Title
Langmuir Waves and Electron Acceleration at Heliospheric Shocks

Author
Pulupa, Marc Peter

Publication Date
2010

Peer reviewed|Thesis/dissertation

Langmuir Waves and Electron Acceleration at Heliospheric Shocks

by

Marc Peter Pulupa

A dissertation submitted in partial satisfaction of the

requirements for the degree of

Doctor of Philosophy

in

Physics

in the

Graduate Division

of the

University of California, Berkeley

Committee in charge:

Professor Stuart Bale, Chair

Professor Robert Lin

Professor Geoff Bower

Spring 2010

Langmuir Waves and Electron Acceleration at Heliospheric Shocks

Abstract

Langmuir Waves and Electron Acceleration at Heliospheric Shocks

by

Marc Peter Pulupa

Doctor of Philosophy in Physics

University of California, Berkeley

Professor Stuart Bale, Chair

Radio waves at the local plasma frequency and its harmonic are generated upstream of collisionless shocks in foreshock regions which are magnetically connected to the shock. The radio waves are created in a multi-step process which involves the acceleration of electrons at the shock front, growth of electrostatic Langmuir waves driven by the accelerated electron beam, and conversion of the Langmuir waves into radio waves.

These radio waves can be used to remotely determine properties of the shock. For example, Type II solar radio burst observations yield information about the radial speed and angular extent of the coronal mass ejection-driven shock associated with the burst. However, in order to completely understand the generation of the radio waves and interpret the remote observations, *in situ* spacecraft measurements of the shock-accelerated electrons and Langmuir waves are necessary.

In this thesis, a brief introduction to the heliospheric environment is followed by a survey of the basic principles of collisionless shocks, a detailed discussion of the process of generating shock-accelerated electrons and the resulting plasma waves, and a description of the relevant instrumentation on board the *Wind* and STEREO spacecraft. Following this review material, several results based on *in situ* observations are presented:

(1) High cadence electron measurements made by *Wind* in the foreshock region of several IP shocks allow for a determination of the spatial scales of the source regions of Type II radio bursts. The sizes of the observed foreshock source regions are comparable to the size of the terrestrial bow shock.

(2) Langmuir waves upstream of IP shocks can be used as a diagnostic signature of foreshock electrons. Using a large database of shocks observed by *Wind*, different shock parameters are statistically tested for their effectiveness at accelerating electrons.

(3) Using a new type of electron detector on STEREO, the limits of the Fast Fermi theory for electron acceleration at suprathermal energies are examined. Preliminary results suggest that the mechanism may hold beyond the regime where the Larmor radius of electrons is much smaller than the scale sizes of the shock.

The prospects for future work in this area are discussed in the conclusion, and a description of an experimental antenna calibration procedure known as rheometry is included as an appendix.

for Vincente and Feliciana Pulupa

Contents

List of Figures

List of Tables

Acknowledgments

I have been extremely fortunate throughout my life to have encountered many individuals who have fostered my interests in science. I owe great thanks to the many excellent teachers who challenged my abilities and sparked my imagination in my early school days. Of these instructors, I particularly would like to thank Robert Donaldson, my first physics teacher, for introducing me to the power, beauty, and limitations of understanding the world through careful scientific reasoning.

As an undergraduate, I worked with Dr. John T. Armstrong at NIST, and in the Space Physics Group at UMCP with Professor Douglas C. Hamilton. Both advisors were generous with their time and eager to give me hands-on experience with interesting problems. My friend and roommate, Kyle Retterer, joined Professor Hamilton's group and suggested I do the same when I was looking for a research position, thereby providing my start in space physics.

In the fall of 2002, I visited Berkeley for the first time thanks to the Berkeley Edge Conference. The experience quickly convinced me that this was the right place for me. I am grateful to the organizers and conference volunteers, especially Dr. Colette Patt, for providing a perfect introduction and invitation to Berkeley.

For graduate students, the most familiar faces in the Physics Department are Anne Takizawa and Donna Sakima, who manage all sorts of graduate student concerns with boundless goodwill and aplomb. Many thanks are due to them for their efforts.

I would like to thank my fellow graduate students, with whom I studied, taught, and played basketball during my time in Berkeley. I should particularly mention Brian Metzger, the founder and leader of our 'Net Force' basketball team, and Mark Bandstra, who has always been a good friend, classmate, and colleague.

I have had a great experience at the Space Sciences Laboratory. The excitement with which I view the prospect of continuing to work at SSL as a postdoc is testament to the collegial and warm environment that is found here. I would especially like to thank all of my companions in Room 260 through the years for their friendship and support.

I would like to express deep thanks to my advisor, Professor Stuart Bale, for consistent encouragement and guidance throughout my graduate career. He has consistently treated me as a valued colleague and has always been willing to listen to my ideas and to explain both simple and difficult concepts.

I would also like to thank Professor Bob Lin, who has always taken an interest in my research and offered helpful advice, and the other members of my thesis and qual committees, Professors Geoff Bower and Jon Arons, for their patience and useful comments.

Any successes I have had are ultimately built on the strong foundation provided by my family. My grandparents, parents, and siblings have always been present for me with love and good cheer. My brother Patrick and I started school in California at the same time, and having him nearby made the big move from the East Coast much easier.

Finally, I would like to thank my wonderful wife Robin for sharing and enriching my life during the past five years, and our son Orson for inspiring me, bringing great joy into our lives, and (sort of) learning to sleep through the night.

Chapter 1

Introduction

1.1 The Sun

The Sun is the central body in the solar system, and has held a central place in the imagination of humanity for millenia, first as an object of worship and later as an object of scientific study. Many of the greatest scientific advances in human history either explain a crucial aspect of the sun's behavior or exploit the sun's mass to test the theories.

Heliocentric cosmology and Newton's theory of gravitation explained the motion of bodies in the solar system, which is gravitationally dominated by the sun. Einstein's theory of general relativity predicted the deflection of light by massive objects, and this theory was tested experimentally using observations of deflection of starlight by solar eclipses.

The development of quantum physics in the early part of the last century provided explanations for both the general shape of the Sun's 5800 K blackbody spectrum and the numerous absorption and emission spectral lines present in sunlight. Discoveries in nuclear physics yielded an understanding of the fusion reaction which provides the sun's energy. More recently, experimental measurements of solar neutrinos provided evidence leading to a modification of the Standard Model of particle physics.

Some of the theories mentioned above, such as classical Newtonian mechanics, represent solved problems in physics. Others, such as general relativity, remain rich fields of research but have moved beyond the solar system to study other regimes, either in the laboratory or on astronomical scales. The present-day field of heliophysics is largely concerned with the study of the plasma in the solar interior, in the solar atmosphere, and in interplanetary space.

1.2 The Heliosphere and the Solar Wind

The region of space where the behavior and nature of the plasma environment is dominated by the sun is known as the heliosphere. The major quiet time plasma influence of the sun in the heliosphere is the continuous outflow of solar plasma and entrained magnetic field known as the solar wind. The prediction and measurement of the solar wind was one of the first and most important successes of heliophysics. The concept of a steady-state outflow of both ions and electrons from the sun, as opposed to transient emissions such as electron beams, was proposed by Kristian Birkeland around the turn of the century (Egeland & Burke 2005). However, Birkeland's solar theories were largely based on laboratory experiments using model magnetic spheres, and most solar physicists remained unconvinced.

The first direct observations of the effect of steady solar wind flow were made in the study of comet tails. It was known that comets could possess multiple tails, one trailing behind the comet in a path predicted by its kinematic motion, and another tail in the radial direction outward from the sun. Biermann (1957) interpreted the second tail as plasma originating from the vaporization of the comet, which was picked up by the flow of the 'solar corpuscular radiation,' and which produced light in a process similar to the mechanism that illuminates the terrestrial aurora. Biermann estimated the speed of the solar outflow, calculating a value of several hundreds of kilometers per second.

In the intermediate years between Birkeland's and Biermann's predictions of outflow from the sun, a crucial piece of evidence had been added by the development of solar spectroscopy. In particular, the identification of lines in the solar spectrum had revealed the surprising fact that the atmosphere of the sun, known as the corona, was much hotter than the photospheric and chromospheric layers of the sun (Edlén 1945). This high coronal temperature made the idea of particles escaping from the sun's massive gravitational potential more plausible than it would be if the coronal temperature was close to the surface temperature. Static calculations of the extent of the solar corona suggested that a million-degree coronal temperature close to the sun would result in a hot interplanetary gas which filled the solar system (Chapman & Zirin 1957). So in the late 1950s, the idea of steady outward flow from the sun and the idea that particles originating from the sun filled interplanetary space were both present in the scientific literature. However, a complete theory and experimental confirmation was required before the concept of the solar wind was generally accepted.

The theory came first, courtesy of Eugene Parker. In a series of landmark papers (Parker 1958a,b, 1965), Parker provided a solution for a the gas dynamic problem of a spherically symmetric solar wind, finding a solution in which the solar wind expands through a critical point and eventually reaches a state of supersonic expansion. Confirmation of the existence of the solar wind consistent with Parker's prediction was made by direct solar wind velocity measurements from Mariner 2 (Neugebauer & Snyder 1962, 1966), which was the first NASA spacecraft to travel beyond the Earth's bow shock and

into interplanetary space. The Mariner 2 measurements also demonstrated that the solar wind velocity and density fluctuated over a large range, suggesting a dynamic and complex origin.

In the half century since the discovery of the solar wind, many spacecraft have made heliospheric observations and contributed to a greatly increased store of knowledge. In terms of basic properties of the solar wind, perhaps the most notable discovery is that the solar wind speed distribution is bimodal, and the fast and slow solar winds come from distinct regions on the sun, with the fast wind coming from open field lines near the poles (known as coronal holes) and the slow wind coming from closed field regions near the equator (the streamer belt) (Hansteen 2009). The approximately 11-year periodic variation of solar magnetic activity known as the solar cycle has considerable impact on the properties of the solar wind plasma, since the separation between coronal holes and streamer belt is relatively simple near the minimum of solar activity, and very complex during active times (McComas et al. 2003).

Fundamental problems relating to the origin and acceleration of the solar wind remain unsolved. In particular, it is still unknown what heats the corona and what processes accelerate the solar wind. These problems are intimately related, and explanations including heating of the corona and solar wind by Alfvén waves (De Pontieu et al. 2007; Chandran & Hollweg 2009) and models which include magnetic reconnection (Edmondson et al. 2009) as an important factor are current areas of active research. Resolution of these problems is likely to come only with improved measurements (Klimchuk 2006).

1.3 The Solar Wind as a Plasma Physics Laboratory

The solar system provides an accessible natural environment for the study of plasma physics. Measurements made in space complement laboratory measurements, providing access to time and length scales and regions of parameter space unavailable in a laboratory. Within the solar wind, many examples of plasma processes which are thought to be universal can be found and studied in an *in situ* environment. In addition to collisionless shocks, which will be discussed in the next chapter, examples include magnetic reconnection, turbulence, and plasma instabilities.

Recently, multispacecraft measurements in the solar wind have shown that magnetic reconnection has been discovered to exist on large time and spatial scales in a quasi steady state (Phan et al. 2006, 2009).

The phenomenon of turbulence, which occurs universally in fluid media, can be studied in the solar wind using field and plasma data. Recent work using wavelet methods (Bale et al. 2005; Podesta 2009; Salem et al. 2009) has been used to compare data with models such as the Alfvénic turbulence model of Goldreich & Sridhar (1995) and shed light on phenomena such as turbulent dissipation.

The large data sets that have been accumulated in the solar wind by missions such

as *Wind* allow for the statistical analysis of solar wind parameter space, showing that the anisotropy in the solar wind is constrained by plasma instabilities. Mirror mode and firehose instabilities seem to bound the distribution of solar wind proton anisotropies (Liu et al. 2006; Hellinger et al. 2006; Kasper et al. 2010), with enhanced wave power present near the boundaries as a signature of the instabilities (Bale et al. 2010).

1.4 Solar Impacts on the Earth and Humanity

The geomagnetic impact of solar activity on the Earth was discovered in the mid-nineteenth century, when Sabine and Wolf independently noted that variation in terrestrial magnetic activity was correlated with the recently discovered solar cycle (Hufbauer 1991). The fact that large solar flare events were often followed by large geomagnetic storms and auroral events (Carrington 1859) indicated solar activity as the ultimate source of terrestrial effects. However, the exact mechanism remained under debate. The discovery of coronal mass ejections (CMEs) (Gosling et al. 1974; MacQueen et al. 1974) and observations of interplanetary shocks associated with CMEs (Cane et al. 1987) offered a consistent mechanism describing the solar origin and transport of energy which drives geomagnetic activity. The role of CMEs has been recognized as predominant[1] (Gosling 1993; Reames 1999) in the appearance of geomagnetic activity. The majority of large geomagnetic storms are driven by CMEs and CME-driven shocks, with a small minority is driven by corotating interaction regions (Zhang et al. 2007). Frontside 'halo' CMEs, which are CMEs that travel in the direction of Earth and whose expansion is therefore seen as a halo in a coronagraph image, are the most geoeffective subset of CMEs (Gopalswamy et al. 2007). CMEs and CME-driven shocks will be discussed further in the following chapter.

The mechanisms by which CME energy is introduced into the magnetosphere and by which the energy generates magnetic fluctuations, injection of particles into the Van Allen radiation belts, and auroral displays (Gonzalez et al. 1994; Pulkkinen 2007) are beyond the scope of this thesis. We will simply mention a few of the potential societal impacts of the interaction of strong CME fields with the magnetosphere, in order to demonstrate the importance of understanding the sun-Earth relationship as completely as is possible.

A National Academy of Sciences report (Committee On The Societal and Economic Impacts Of Severe Space Weather Events 2008) identified four examples of societal impact of solar disturbances, which are listed below. The first two impacts have potential societal costs of billions of dollars, while the second have smaller potential costs on the order of millions of dollars, but represent growing sectors of the economy.

[1]It may be noted that the relationship between flares and CMEs is complex and remains incompletely understood (Hudson et al. 1995), and that there are sometimes important direct geoeffective ionospheric effects from very large flares (Dmitriev & Yeh 2008).

- Damage to satellite systems. Spacecraft in the regions affected most by solar activity experience an increased rate of anomalies due to spacecraft charging and penetration of energetic ions and electrons into sensitive areas in the spacecraft instruments or electronics (Baker 2005; Barth 2005).

- Interruption of electric power and other systems. These events are a result of induced electric fields in the conducting earth, which lead to changes in ground potential at different locations and can drive currents in large networks of conductors such as power systems. The most commonly cited effect of geomagnetic activity on society at large is the Hydro-Québec power system failure in March 1989. Accurate information about possible disturbances is valuable due to the very high cost of system failures and the considerable cost of false alarms (Pirjola et al. 2000; Kappenman et al. 2000)

- Degradation of GPS signal. The availability of non-degraded GPS signals, once the exclusive province of military users, has promoted rapid growth in industries which make use of the accurate time and location signals provided by the satellites. Ionospheric effects due to severe space weather (Kintner & Ledvina 2005) and radio bursts (Cerruti et al. 2008) can degrade the performance of GPS systems.

- Disruption of flight activity in the polar regions. In addition to GPS-related effects, commercial flights over the polar regions, which have increased in recent years, are susceptible to radiation hazards and communications problems during periods of high activity.

The Carrington event remains the strongest magnetic storm in history as measured by ground-based magnetometers (Tsurutani et al. 2003). Although the event is clearly extreme when ranked against other strong events using a variety of parameters (Cliver & Svalgaard 2004), other events have possessed some properties which surpass the Carrington event, so it is unclear exactly why the event had such a large impact on the Earth. The impact of a similar event in today's technologically-dependent society is uncertain.

1.5 Goals of this Thesis

This chapter has given an extremely brief and broad introduction to the heliosphere, and mentioned a few reasons why study of this environment is interesting and useful. The particular area of this large field with which this thesis is concerned is electron acceleration and associated wave activity generated by shocks in the heliosphere. The following two chapters (2-3) introduce the basic physical concepts describing these phenomena, and Chapter 4 describes the spacecraft instrumentation used to study them. Chapters 5-7 describe several new results on this topic, and Chapter 8 summarizes and places these results in the broader context presented in this introductory chapter.

Chapter 2

Collisionless Shocks

The common thread running through the results presented in this thesis is the acceleration of electrons at collisionless shocks in the heliosphere. This chapter presents an overview of collisionless shocks, emphasizing the basic physical processes which lead to the generation of shocks and briefly reviewing the observational and theoretical development of the subject.

2.1 General Properties of Shocks

Before starting the discussion of collisionless shocks, it is useful to briefly mention some properties of ordinary collisional hydrodynamic shocks, in order to illustrate the similarities and differences between the two.

We consider a physical object traveling through a hydrodynamic medium, and creating a disturbance in that medium. The case of flow around a stationary object is equivalent, since the two cases differ simply by a Galilean frame shift, for the nonrelativistic shocks we consider in this thesis. The region of the medium which has not yet been disturbed is known as the upstream region, while the region which has encountered the disturbance is known as the downstream region. In ordinary hydrodynamics, information about a disturbance traveling through a medium can be carried upstream of the disturbance into the undisturbed medium via acoustic pressure waves. These waves, traveling at the sound speed of the medium, can gradually mediate the density, energy, and other properties of the upstream flow and allow for a smooth, laminar transition from the upstream to the downstream region. If the disturbance is traveling with a speed greater than the sound speed of the medium, then there is no way for information about the approaching disturbance to be transmitted upstream, and the transition from upstream to downstream is sharp and discontinuous. The difference between these two scenarios is parametrized using the Mach number M, which is defined as the ratio of the

disturbance velocity (relative to the rest frame of the medium) to the sound speed in the medium. A Mach number less than 1 indicates subsonic flow, while a Mach number greater than 1 indicates supersonic flow.

The transition between the upstream and downstream region for a supersonic disturbance is known as a shock. In dynamical terms, the role of a shock is to slow the upstream material to below the downstream sound speed, by transforming the ram energy of the upstream flow into thermal energy in the downstream flow. The shock is created by nonlinear waves generated by the disturbance. An initial sinusoidal waveform will deform due to nonlinearities in the wave dispersion relation, which cause the peaks of the sound wave to move faster than the troughs and catch up with them. This nonlinear deformation results in a steepening of the wave profile and, eventually, a sharp discontinuity (Shu 1992).

At a hydrodynamic shock, the collisional mechanism which heats and energizes the plasma is the viscosity $\nu \approx \lambda v_{\rm th}$, where λ is the mean free path and $v_{\rm th}$ is the thermal speed of particles in the gas. It can be shown (Shu 1992) that in a viscous shock the length scale of the transition from upstream to downstream is on the order of the particle mean free path. Over this length scale, the shock is decelerated from above the sound speed to below it, the density rises proportionally to the decrease in velocity, and the temperature rises due to the effects of the viscous heating. This heating process involves an irreversible increase in the entropy of the gas from the upstream to the downstream region (Whitham 1974).

Regardless of the mechanism of energy dissipation within the shock layer, every shock must obey conservation of mass, momentum, and energy. The equations describing the conservation of these quantities over the shock transition layer are known as the Rankine-Hugoniot (RH) relations. The RH relations can be generalized to include electromagnetic effects, as will be shown later in this chapter.

2.2 Collisionless Shocks

The concept of collisionless shocks in interplanetary space, like that of the solar wind, was proposed several years before direct *in situ* plasma measurements were available. The first indication that shocklike processes were involved in the heliosphere came from terrestrial observations of geomagnetic storms associated with solar flares. The time between the flare and the storm is typically on the order of one or two days, however, the onset of the magnetic storm takes place over a time period of minutes. Under the assumption that the storm is driven by injection of plasma particles from the solar flare site, the sudden rise time implies an highly monoenergetic beam with an unrealistically narrow spread in velocity. The propagation of a shock wave was proposed as a natural solution to the problem of maintaining a sharply defined disturbance over the distance of 1 AU (Gold, 1955, as cited in Sagdeev 1979). Parker's prediction of the solar wind also

implied that the interaction between the Earth's magnetosphere and the interplanetary plasma involved supersonic flow past a magnetic obstacle, implying the existence of a shocklike structure analogous to shocks observed in collisional gases (Kellogg 1962).

Early spacecraft measurements confirmed the presence of what became known as the terrestrial bow shock upstream of the Earth (Ness et al. 1964), and also of traveling interplanetary shocks driven by solar events (Burlaga 1971), which are the drivers of the sudden storm commencement events described by Gold (Chao & Lepping 1974; Wang et al. 2006).

The development of collisionless shock theory progressed alongside the experimental results. The initial efforts focused on describing the mechanism by which a collisionless shock can exist in the first place. In contrast to the fairly simple microscopic mechanics of binary particle collisions which drives shock formation and heating in a collisional medium, collisionless shocks are created by the collective motion and self-generated fields of the plasma. The task of slowing and heating the upstream material is accomplished by plasma processes such as turbulence and instabilities. The complex nature of plasma turbulence and the large number of different types of instabilities, (e.g. the ion acoustic, lower hybrid, and two stream instabilities) which are possible in a space plasma implies that the problem of shock heating is quite complex (Wu 1982; Papadopoulos 1985).

Many of the properties of hydrodynamic collisional shocks are also applicable at collisionless shocks. In particular, the RH relations, modified to account for the electromagnetic contribution to momentum and energy, also hold for collisionless shocks. However, the addition of magnetic field and the multi-species nature of the particles which make up a plasma give rise to a wide set of phenomena which are not present at conventional shocks. We will discuss in this chapter several of the most important phenomena which are unique to collisionless shocks: the complicated and multi-component structure of the shock, the many qualitatively different categories of collisionless shocks, and the ability of collisionless shocks to accelerate particles to high energies.

2.3 Collisionless Shocks in the Heliosphere

In the interplanetary medium, the Coulomb collisional mean free path for both protons and electrons is on the order of a fraction of 1 AU (1.5×10^8 km) (Livi et al. 1986; Salem et al. 2003), while the ion gyroradius, a typical observed shock scale length, is on the order of tens of kilometers. Therefore, Coulomb collisions at shocks occurring in the medium may be ignored when considering the shock dynamics.

Figure 2.1 is a cartoon illustrating the locations of various types of collisionless shocks in the heliosphere. The locations of shock fronts are shown as red lines, while the arrows represent the plasma flow speed, with the shocks developing at locations where the differential flow speed is large. The shocks represented in the cartoon are:

- **Stream Interaction Region (SIR) IP shocks.** These shocks are driven by

streams of solar wind plasma with different radial speeds. The histogram of observed speeds in the solar wind has a bimodal distribution, with the "fast wind" originating from open field line regions known as coronal holes, while the "slow wind" is generated in closed field regions known as streamer belts (Hansteen 2009). If a slow wind source region lies ahead (i.e., closer to the western limb) of a fast region at the same latitude, then the Parker spiral outflow from the fast region will catch up to the flow from the slow region, driving a compressional buildup of solar wind plasma at the interaction region between the two streams (Smith & Wolfe 1976; Pizzo 1978; Gosling & Pizzo 1999). SIRs which persist long enough to be seen more than once in separate solar rotations are known as Corotating Interaction Regions (CIRs). Depending on the properties of the compression region, shocks may develop at both the forward (anti-sunward) and reverse (sunward) boundary of the interaction region. Roughly one quarter of SIRs exhibit a forward or reverse shock, with forward shocks being more common. The persistent CIR subset of SIRs tend to be faster and larger, and the occurrence of shocks is higher at CIRs than at all SIRs (Jian et al. 2006).

- **Coronal Mass Ejection (CME) associated IP shocks.** Coronal mass ejections are immense and spectacular solar events involving the expulsion of massive quantities of plasma from the solar corona. CMEs are generated by the release of magnetic energy close to the surface of the sun, and propagate outwards through the heliosphere. The rate and average speed of CMEs varies with the solar cycle, ranging from about several per month with an average speed of 300km/s at solar minimum to several per day with an average speed of around 500km/s near solar maximum. The fastest CMEs reach speeds well over 1000km/s (Yashiro et al. 2004). If a CME has sufficient speed relative to the solar wind, it will drive an IP shock ahead of the ejected material (Schwenn 1983; Sheeley et al. 1985). The occurrence rate of CME-generated interplanetary shocks, like the occurrence rate of CMEs, is well correlated to the solar cycle. The Alfvénic Mach number for IP shocks ranges from 1 to 8, and the fast mode Mach number ranges from 1 to 6 (Gopalswamy et al. 2010, see also Chapter 6). (These Mach numbers will be defined and discussed later in this chapter.) Type II radio bursts, which are discussed further in Chapter 3, are a primary signature of a CME-driven IP shock. CMEs which drive shocks and type II bursts tend to be both faster and wider than the entire population of CMEs. (Cane et al. 1987; Gopalswamy et al. 2005, 2008).

- **Bow shocks associated with magnetized bodies.** Planetary bodies which contain an internal dynamo[1] generate a magnetospheric field, which in the absence

[1] In the solar system, the planets Mercury, Earth, Jupiter, Saturn, Uranus, and Neptune have internal dynamos, while Venus, Mars, and most moons do not. Jupiter's moon Ganymede also has an internal dynamo, but it is within Jupiter's magnetosphere and the plasma which it encounters is subsonic (Bagenal 2009).

of perturbation may be approximated by a dipole. The magnetosphere presents an obstacle to the solar wind flow, generating a bow shock similar in nature to the detached hydrodynamic shock that occurs in front of a blunt object passing through a medium at supersonic speed (Spreiter et al. 1966). The magnetosphere is compressed below the nose of the bow shock and elongated behind the planet into a tail. The outer limit of the magnetosphere is known as the magnetopause, and is defined as the boundary between field lines which originate within the Earth and those that originate in the solar wind. In between the magnetopause and the bow shock lies the magnetosheath, a turbulent region of plasma (Vasyliunas 2009). The magnetospheres of the magnetized planets all share these general features, but differ greatly in size due to the radial dependence of the solar wind flux and variation in the properties of the planetary dipoles (Slavin & Holzer 1981; Bagenal 2009).

- **Bow shocks associated with unmagnetized bodies.** The interaction of the solar wind with unmagnetized bodies depends on whether the body has an atmosphere. Planets like Mars and Venus have no internal dynamo and therefore no magnetosphere, but they do have gravitationally bound atmospheres. The upper regions of these atmospheres are ionized by solar ultraviolet radiation, creating a conducting ionosphere which allows currents to flow and create an electromagnetic obstacle for the solar wind and a corresponding bow shock (Luhmann 1986; Mazelle et al. 2004). Comets are also surrounded by ionized plasma due to the melting of cometary material by solar radiation, and can develop bow shocks (Cravens & Gombosi 2004). Bodies with no atmosphere, such as the Moon, do not create upstream shocks, as there is no upstream obstacle presented to the solar wind. Instead, the solar wind is absorbed by the lunar surface, creating a plasma wake behind the Moon (Schubert & Lichtenstein 1974). The solar wind plasma subsequently refills the wake, in the process generating waves and turbulence (Kellogg et al. 1996; Bale 1997).

- **Shocks in the outer heliosphere.** Just as the flow of the solar wind past a magnetized body creates the magnetosphere, the supersonic flow of the warm and partially ionized local interstellar medium (LISM) past the solar system creates the heliosphere. The heliopause, in a role analogous to the magnetopause of a magnetospheric system, is the boundary between the solar system plasma and the LISM. Upstream of the heliopause, a heliospheric bow shock forms where the LISM flow is incident to the heliosphere (Zank 1999). The presence inside the heliosphere of the radially expanding and decelerating solar wind adds an additional shock to the outer heliosphere interaction, where the solar wind slows below the magnetosonic speed before it encounters the heliopause (Richardson & Stone 2009). Both Voyager spacecraft have recently encountered this shock, which is known as the termination shock (Burlaga et al. 2005; Decker et al. 2005; Burlaga et al. 2008).

2.4 MHD Wave Modes

Many of the basic features of collisionless shocks can be described approximately using the magnetohydrodynamic (MHD) approximation, which treats the plasma as a fluid and deals only with the bulk properties (density ρ, bulk velocity $\mathbf{u}$, magnetic field $\mathbf{B}$, and plasma pressure p, where $p = n_{\rm p}kT_{\rm p} + n_{\rm e}kT_{\rm e}$). Ideal MHD makes the further approximation of ignoring resistive and viscous effects.

The MHD equations are valid in the low frequency, large scale regime of the plasma. The ideal MHD equations are (Kantrowitz & Petschek 1966):

$$\text{Continuity:} \quad \frac{\partial p}{\partial t} + \nabla \cdot \rho\mathbf{u} = 0 \tag{2.1}$$

$$\text{Momentum:} \quad \rho\frac{\partial \mathbf{u}}{\partial t} + \rho\mathbf{u}\cdot\nabla\mathbf{u} + \nabla p - \frac{(\nabla\times\mathbf{B})\times\mathbf{B}}{\mu_0} = 0 \tag{2.2}$$

$$\text{Induction:} \quad \frac{\partial \mathbf{B}}{\partial t} - \nabla\times(\mathbf{u}\times\mathbf{B}) = 0 \tag{2.3}$$

$$\text{Entropy:} \quad \frac{\partial(p/\rho^\gamma)}{\partial t} + \mathbf{u}\cdot\nabla\frac{p}{\rho^\gamma} = 0 \quad (p/\rho^\gamma = \text{ constant}) \tag{2.4}$$

where we have used the ideal MHD approximation $\mathbf{E} = -\mathbf{u}\times\mathbf{B}$ to eliminate $\mathbf{E}$, and where γ is the standard hydrodynamic adiabatic index, equivalent to the ratio of specific heats $C_{\rm p}/C_{\rm v}$.

The two characteristic speeds of an MHD plasma are the hydrodynamic sound speed $c_{\rm s}$ and the Alfvén speed $v_{\rm A}$. The sound speed is the ordinary speed of sound waves in the plasma, while the Alfvén speed can be compared to a standing wave on a tightened string, with the mass density of the plasma analogous to the linear density of the string and the magnetic field analogous to the string tension. The sound speed and Alfvén velocity are given by:

$$c_{\rm s} = \sqrt{\gamma p/\rho} \tag{2.5}$$

$$v_{\rm A} = \frac{B}{\sqrt{\mu_0\rho}} \tag{2.6}$$

If the ideal MHD equations are subjected to a small perturbation, and only the first order terms in the perturbed quantities are kept, then there are three non-trivial propagating MHD wave solutions (Kantrowitz & Petschek 1966). The exact speed of the solutions depends on the angle θ between the wave propagation vector $\mathbf{k}$ and the magnetic field $\mathbf{B}$. The three wave solutions are known as the fast wave, the intermediate

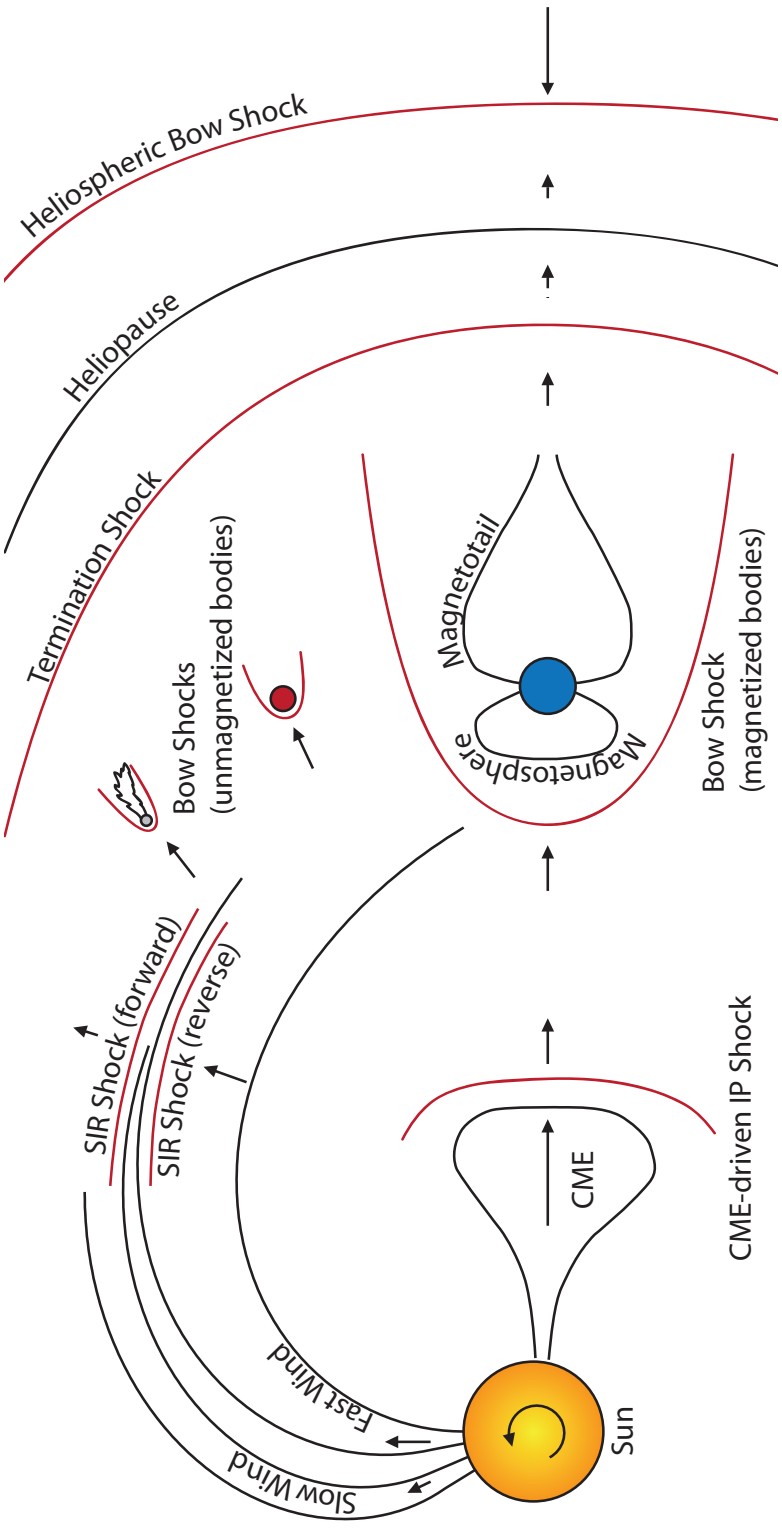

Figure 2.1: Cartoon showing examples of shocks in the heliosphere. Magnetic field lines are black, while the locations of shock fronts are labeled in red. The viewer is looking down on the ecliptic plane from above, except for the case of the bow shock interaction with the magnetized body, in which case the viewer is in the ecliptic plane. Arrows represent the flow speed of the solar wind, the CME, the interplanetary medium, or the LISM.

wave, and the slow wave, and their respective speeds are given by:

$$\text{Fast:} \quad v_\mathrm{f} = \frac{1}{2}\left(c_\mathrm{s}^2 + v_\mathrm{A}^2 + \left(\left(c_\mathrm{s}^2 + v_\mathrm{A}^2\right)^2 - 4c_\mathrm{s}^2 v_\mathrm{A}^2 \cos^2\theta\right)^{1/2}\right) \tag{2.7}$$

$$\text{Intermediate:} \quad v_\mathrm{i} = v_\mathrm{A}\cos^2\theta \tag{2.8}$$

$$\text{Slow:} \quad v_\mathrm{s} = \frac{1}{2}\left(c_\mathrm{s}^2 + v_\mathrm{A}^2 - \left(\left(c_\mathrm{s}^2 + v_\mathrm{A}^2\right)^2 - 4c_\mathrm{s}^2 v_\mathrm{A}^2 \cos^2\theta\right)^{1/2}\right) \tag{2.9}$$

The phase speed of the intermediate wave always lies between that of the fast wave and the slow wave. Figure 2.2 shows the relation between the phase speeds of the MHD wave modes on a polar plot, illustrating the nature of the wave modes for the case where the Alfvén speed is greater than the sound speed, which is typical of the solar wind at 1 AU.

Shocks in MHD plasmas correspond to a steepened version of one of these three wave modes. The numbers $1, 2, 3, 4$ in Figure 2.2 denote different regimes of $\omega/\mathbf{k}$-space, and the boundaries of each region correspond to the speeds of the MHD waves. Shocks involve transitions from one regime to another: a fast shock involves the transition from regime 1 to regime 2 ($1 \rightarrow 2$), while a slow shock corresponds to $3 \rightarrow 4$ and an intermediate shock corresponds to all other available transitions ($1 \rightarrow 3$, $1 \rightarrow 4$, $2 \rightarrow 3$ and $2 \rightarrow 4$) (Draine & McKee 1993).

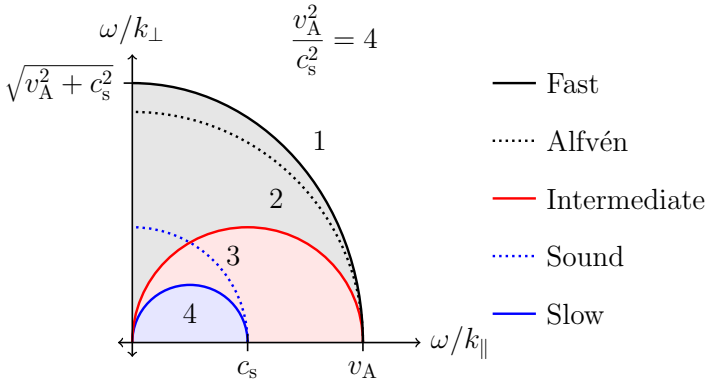

Figure 2.2: Friedrichs diagram showing a polar plot of phase speed for the different MHD wave modes, for a plasma where $v_\mathrm{A} > c_\mathrm{s}$. The three MHD wave modes are plotted with solid lines, while the characteristic speeds in the plasma are plotted with dashed lines. The numbers mark the different regions in velocity space, with transitions between different regions corresponding to different types of shocks.

The intermediate wave mode is transverse (i.e., the oscillatory quantities of the wave are the components of $\delta\mathbf{v}$ and $\delta\mathbf{B}$ which are out of the plane defined by the propagation

vector $\mathbf{k}$ and the upstream magnetic field $\mathbf{B_1}$), while the fast and slow waves are a mixture of transverse and compressional (Kantrowitz & Petschek 1966). A useful heuristic to differentiate the fast and slow waves is to consider the fast wave as the mode where an Alfvén wave and an acoustic wave act in concert and create a wave faster than either the Alfvén wave or the sound wave alone, while in the slow wave the two counteract each other and create a wave slower than either wave alone.

2.5 Shock Parameters and the Rankine-Hugoniot Relations

In the MHD limit, treating the plasma as a single fluid and ignoring the substructure of the shock to treat it as a infinitesimal discontinuity, the parameters which define the upstream/downstream plasma and the shock determine completely the state of the downstream/upstream plasma. Similarly, measurements of the plasma parameters can be used to derive the shock parameters.

The parameters which characterize the upstream plasma are the density ρ_1, the pressure p_1, the upstream velocity in the shock frame $\mathbf{u}_1$, and the upstream magnetic field $\mathbf{B}_1$. In addition to the upstream plasma parameters, the shock interaction is also determined by the shock parameter $\hat{\mathbf{n}}$, defined as the unit vector normal to the surface of the shock. In particular, the angle θ_{Bn} between the shock normal and the upstream magnetic field plays a large role in controlling the properties of the shock. See Figure 2.3 for an illustration of the upstream and downstream shock parameters.

Shocks with $\theta_{\mathrm{Bn}} \approx 0^\circ$ are known as parallel shocks, and shocks with $\theta_{\mathrm{Bn}} \approx 90^\circ$ are known as perpendicular shocks. Shocks with other values of θ_{Bn} are known as oblique shocks, and are divided into quasi-parallel and quasi-perpendicular, with the division point usually taken as $\theta_{\mathrm{Bn}} = 45^\circ$. Observationally, the difference between quasi-parallel and quasi-perpendicular shocks is driven by the fact that particles and certain waves (such as whistler waves) tend to travel along magnetic field lines. As a quasi-parallel shock, these effects can therefore propagate a long distance away from the shock, while at a quasi-perpendicular shock they are confined to a smaller scale.

The MHD model is a considerable simplification, even in a collisional plasma, where the ideal MHD equations will not accurately describe currents and small scale structures in the plasma. In a collisionless plasma, the MHD approximation is even less applicable, since collisionless plasmas often exhibit severe deviations from thermal equilibrium. However, the simplification offered by the MHD approximation can offer insight, and for many space plasmas the approximation works quite well. In particular, while the MHD conditions should not be expected to obtain within the shock layer itself, the Rankine-Hugoniot (RH) conservation relations derived from the MHD approximation can be used quite effectively to derive shock parameters (Szabo 1994).

The MHD RH conservation relations, or RH jump conditions, describe plasma quantities that are conserved in the transition from upstream to downstream regardless of

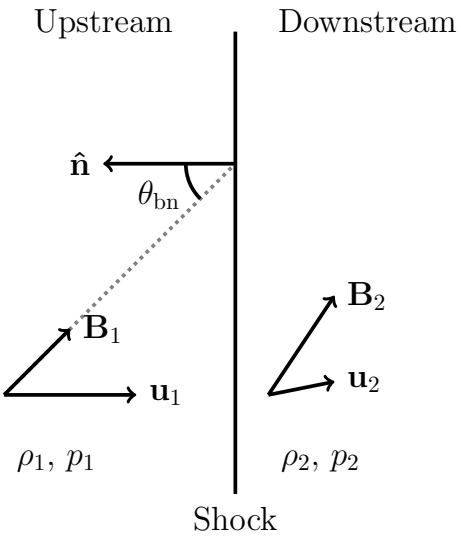

Figure 2.3: Cartoon illustrating shock parameters in the upstream and downstream regions of a shock.

the dynamics of the shock itself. They are usually presented using the convention that a quantity enclosed within brackets ([ ]) represents a difference between the upstream value and the downstream value. The formulation of the RH equations presented here is that presented by Burgess (1995). The first plasma RH condition, which represents conservation of number density across the shock front, is written as:

$$[\rho u_{\mathrm{n}}] = 0 \tag{2.10}$$

where $[\rho u_{\mathrm{n}}] = \rho_{\mathrm{u}} u_{\mathrm{nu}} - \rho_{\mathrm{d}} u_{\mathrm{nd}}$ and the subscripts u and d signify the upstream and downstream states. The subscript n identifies the component of velocity normal to the shock front. The second and third RH conditions result from the conservation of momentum in the shock in the normal direction across the shock front and in the plane transverse to the shock, with transverse components identified by the subscript t.

$$\left[\rho u_{\mathrm{n}}^2 + p + \frac{B^2}{2\mu_0}\right] = 0 \tag{2.11}$$

$$\left[\rho u_{\mathrm{n}} \mathbf{u}_{\mathrm{t}} - \frac{B_{\mathrm{n}}}{\mu_0}\mathbf{B}_{\mathrm{t}}\right] = 0 \tag{2.12}$$

Conservation of energy (combined kinetic energy from the bulk flow and internal energy from plasma pressure and electromagnetic energy) yields the fourth RH equation:

$$\left[\rho u_{\mathrm{n}} \left(\frac{1}{2}u^2 + \frac{\gamma}{\gamma - 1}\frac{p}{\rho}\right) + u_{\mathrm{n}}\frac{B^2}{\mu_0} - \mathbf{u}\cdot\mathbf{B}\frac{B_{\mathrm{n}}}{\mu_0}\right] = 0 \tag{2.13}$$

Finally, Maxwell's equations require that the normal component of the magnetic field remain constant across the shock, and that the tangential component of the $(-\mathbf{u} \times \mathbf{B})$ electric field remain constant (since $\nabla \times \mathbf{E} = \partial \mathbf{B}/\partial t$ and we assume that the shock is time independent).

$$[B_{\rm n}] = 0 \tag{2.14}$$

$$[u_{\rm n}\mathbf{B}_{\rm t} - B_{\rm n}\mathbf{u}_{\rm t}] = 0 \tag{2.15}$$

Several important properties of fast and slow mode shocks follow directly from the RH conditions. The coplanarity theorem, which shows that the upstream and downstream velocity, upstream and downstream magnetic field, and shock normal all lie in the same plane, is a simple and extremely useful result. It is proven (see, e.g., Burgess 1995) by noting first that Equations 2.12 and 2.15 require both $[u_{\rm n}\mathbf{B}_{\rm t}]$ and $[\mathbf{B}_{\rm t}]$ to be parallel to $[\mathbf{u}_{\rm t}]$, provided that we exclude the singular case of the intermediate shock with $u_{\rm n} = v_{\rm i}$. Taking the cross product, we have

$$[\mathbf{B}_{\rm t}] \times [u_{\rm n}\mathbf{B}_{\rm t}] = 0 \tag{2.16}$$

which, when expanded, is equivalent to

$$[u_{\rm n}](\mathbf{B}_{\rm tu} \times \mathbf{B}_{\rm td}) = 0 \tag{2.17}$$

which implies that the $\mathbf{B}_{\rm tu}$ and $\mathbf{B}_{\rm td}$ vectors are parallel, and therefore that the $\mathbf{B}_{\rm u}$, $\mathbf{B}_{\rm d}$, $\hat{\mathbf{n}}$, and $[\mathbf{u}]$ vectors all lie in the same plane, known as the coplanarity plane.

In addition to simplifying the task of drawing diagrams representing shocks, the coplanarity theorem is a useful tool to calculate the shock normal, which usually cannot be measured directly and must be calculated from the asymptotic parameters. Any two vectors in the coplanarity plane can be crossed to yield a vector perpendicular to $\hat{\mathbf{n}}$, and since any two such perpendicular vectors uniquely determine $\hat{\mathbf{n}}$, the multiple vectors in the coplanarity plane can be used to generate several measurements of the shock normal. (Abraham-Shrauner 1972; Paschmann & Schwartz 2000).

Another simple manipulation of the RH equations involves a major difference between fast and slow mode shocks. Using the coplanarity theorem and the definition of $v_{\rm i}$ from Equation 2.9, we can rewrite Equation 2.12 as

$$\left[\left(\frac{u_{\rm n}^2}{u_{\rm i}^2}\frac{u_{\rm t}}{u_{\rm n}}\frac{\cos\theta_{\rm bn}}{\sin\theta_{\rm bn}} - 1\right)\mathbf{B}_{\rm t}\right] = 0 \tag{2.18}$$

If the shock is in a specific frame[2] where the velocity and magnetic field are parallel, then this equation may be reduced further, to (Friedrichs & Kranzer 1958; Draine & McKee

[2]This frame is known as the de Hoffmann-Teller frame and will be described more fully in the following chapter.

1993)

$$\left[\left(\frac{u_{\rm n}^2}{u_{\rm i}^2} - 1\right)\mathbf{B}_{\rm t}\right] = 0 \tag{2.19}$$

Equation 2.19 has important consequences for the behavior of the magnetic field at intermediate waves, and fast and slow shocks. For intermediate waves with $u_{\rm n} = u_{\rm i}$, the quantity in parentheses in 2.19 is zero and rotation of the magnetic field out of the plane defined by $\hat{\mathbf{n}}$ and $\mathbf{B}_{\rm u}$ is possible, but not for any other type of disturbance. For the fast mode shock, the quantity in parentheses in Equation 2.19 is positive in sign on both sides of the shock and decreases in magnitude across the shock, showing that the fast mode increases $\mathbf{B}_{\rm t}$ (and, therefore, B) across the shock. For the slow mode shock, the quantity in parentheses is negative in sign and increases in magnitude, so $\mathbf{B}_{\rm t}$ and B decrease across the shock front (see Figure 2.4.) Finally, we note that although we have proved this result in the de Hoffmann-Teller frame, none of the quantities in 2.19 is changed by a transformation to any other frame in which the shock is stationary, provided that the transformation is nonrelativistic so that we can ignore factors of u^2/c^2. Therefore, these results are not in general frame-dependent.

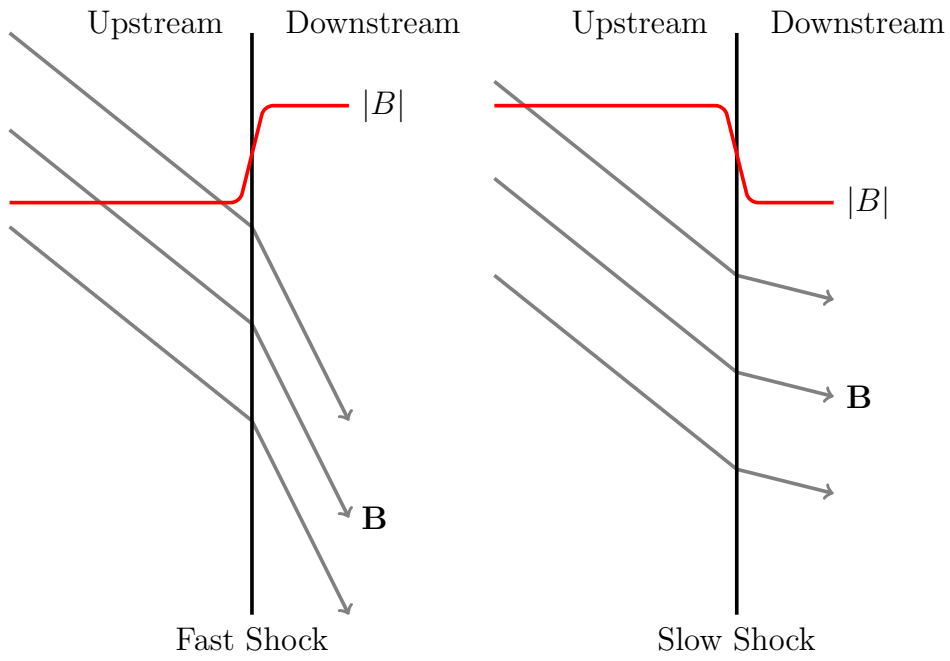

Figure 2.4: Cartoon illustrating the difference between fast and slow mode shocks. The magnitude of B increases from upstream to downstream for a fast mode shock, while it decreases for a slow mode shock.

2.6 Observations

The most well-studied shock in the heliosphere is the terrestrial bow shock, due to its proximity to the earth. The first unambiguous crossing of the bow shock was the made by Mariner 2, which was the first spacecraft to make measurements of the the solar wind direction and velocity (Neugebauer & Snyder 1962). Since then, many spacecraft have made bow shock measurements. Most features found at heliospheric shocks were first observed and described at the terrestrial bow shock. Since the flow speed of the solar wind is nearly always greater than 250 km/s (Gosling et al. 1971), the Alfvén speed is rarely greater than 100 km/s, and the sound speed is usually less than the Alfvén speed (Mullan & Smith 2006), the terrestrial bow shock is essentially always a fast mode shock. The dynamics of the shock are therefore controlled by the fast mode Mach number $M_{\rm f} = u_{\rm sw}/v_{\rm f}$ and the angle between the magnetic field and the (local) shock normal $\theta_{\rm bn}$.

Figure 2.5 shows several examples of terrestrial bow shock crossings observed by the *Wind* spacecraft, giving a hint of the variation of bow shock appearance. Each panel shows a time series of magnetic field magnitude during the shock crossing. The top panel shows a laminar shock, with relatively steady upstream and downstream fields. This type of shock is found at quasiperpendicular, low β and low Mach number crossings (Greenstadt 1985). The middle panel shows a quasiparallel crossing with large amounts of upstream and downstream turbulence. Finally, the bottom panel shows a high Mach number quasiperpendicular shock, and illustrates the structure often seen in these types of shock (Burgess 1995). The upstream magnetic field is constant until time 0225, then from roughly 0225 to 0226 it rises slowly, creating what is known as the foot region of the shock. The length of the foot region is usually on the order of the ion gyroradius, a signature of its origin in ions reflected from the front of the shock. Following the foot region, the magnetic field increases sharply at around time 0226, in what is known as the ramp region. The magnetic field just past the ramp is higher than the eventual downstream value of the magnetic field, a phenomenon known as overshoot. Further examples of different types of collisionless shocks may be found in Greenstadt (1985) and Russell (1985).

The majority of traveling interplanetary shocks within 1 AU are also fast mode shocks, with propagation velocities in the solar wind frame of 50 to 400 km/s (Volkmer & Neubauer 1985). However, slow interplanetary shocks have been observed and make up a small minority of observed interplanetary shocks (Chao & Olbert 1970; Whang et al. 1998). Intermediate shocks are rarer still but have been observed in the outer heliosphere (Chao et al. 1993; Feng & Wang 2008).

Figure 2.6 shows an example of a typical quasiperpendicular interplanetary fast mode shock observed by the *Wind* spacecraft, showing the variation of several different plasma parameters across the shock front. The data, measured by the MAG and 3DP instruments on board *Wind*, are shown in black, while the red lines show a RH solution to the shock. The downstream RH values of the plasma parameters are the solution to the RH equations

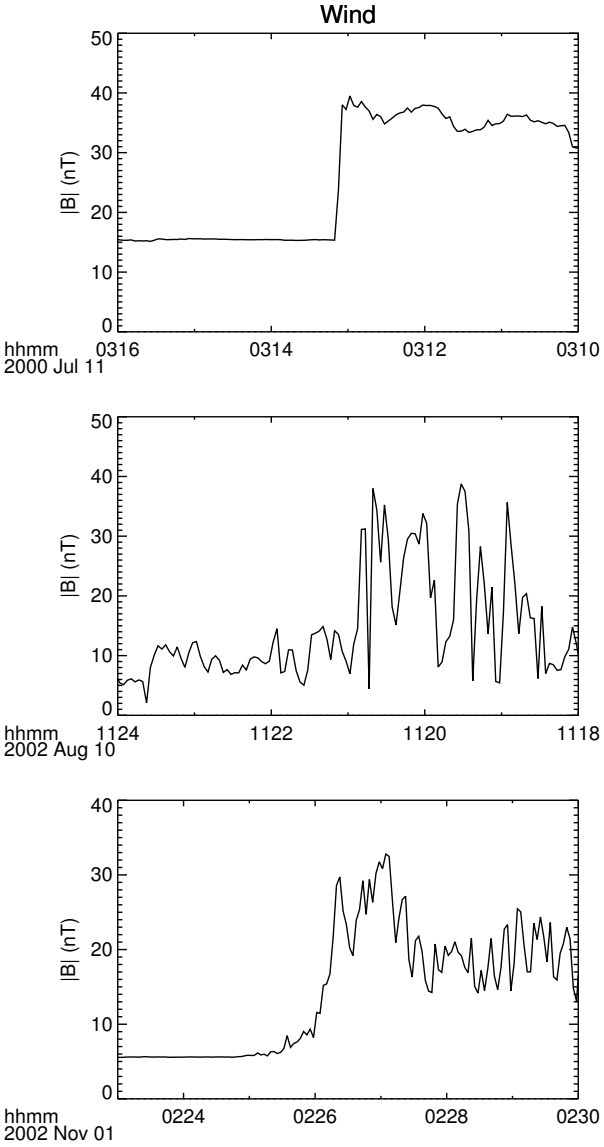

Figure 2.5: Several examples of bow shock crossings observed by the *Wind* spacecraft. The upstream magnetic field is shown in the left of the plot, and the downstream field is shown to the right after the shock jump. The top panel displays a laminar shock crossing with relatively steady upstream and downstream fields. The middle panel displays a highly turbulent quasiparallel shock crossing, with turbulent upstream and downstream fields. The bottom panel displays a structured quasiperpendicular shock, with visible foot, ramp, and overshoot regions. The top and middle panels display an outbound shock crossing, and therefore the time scale for these panels is reversed.

given the measured upstream parameters, and shock parameters ($M_{\rm f}$, $\theta_{\rm bn}$, and γ) which were varied until the solution provided a reasonable fit. In preparing this simple example, it was assumed that the shock front was propagating radially from the Sun, i.e. the shock normal pointed in the $\hat{\mathbf{x}}$ direction.

There are notable deviations between the RH solution and the temperature data. The single fluid MHD model does not allow for differential heating between ions and electrons, a feature commonly seen at shocks (Goodrich & Scudder 1984). We will discuss some limitations of the MHD model, and their importance to the physics of collisionless shocks, in the next section.

2.7 Length Scales in Collisionless Plasmas

While ideal MHD is a useful conceptual tool and often yields reasonable results for the asymptotic plasma parameters upstream and downstream of a shock, it is not applicable for investigation of the internal dynamics of the shock. A review of the limitations of MHD theory for space plasmas may be found in Parks (2004). An area of particular relevance for this thesis is electron scale physics within the shock structure, which is not well approximated by ideal MHD.

Comparing the formulation of Ohm's Law in ideal MHD and in a generalized form which includes the terms ignored in ideal MHD is a useful way to illustrate the types of phenomena which are not described well by the ideal MHD approximation. The single-fluid nature of the ideal MHD approximation yields a simple version of Ohm's Law in the plasma:

$$\mathbf{E} = -\mathbf{v} \times \mathbf{B} \tag{2.20}$$

This simple relation can be qualitatively understood by assuming that there is zero electric field parallel to the direction of the magnetic field, that there is zero electric field if the plasma is at rest, and that if the plasma is moving, and the induced electric field is the one that is generated by the appropriate Lorentz transformation from the plasma rest frame in the low-velocity limit. This form of Ohm's law may be used, along with Maxwell's equations, to derive the "frozen-in" condition which states that the bulk plasma motion is bound to the motion of the magnetic field lines if the ideal MHD conditions are met.

The generalized form of Ohm's law includes resistive, viscous, and inertial effects ignored in the ideal MHD equation. It is given by Vasyliunas (1975) as:

$$\mathbf{E} + \mathbf{v} \times \mathbf{B} = \eta \mathbf{j} + \frac{m_e}{ne^2}\left[\frac{\partial \mathbf{j}}{\partial t} + \nabla \cdot (\mathbf{v}\mathbf{j} + \mathbf{j}\mathbf{v})\right] - \frac{\mathbf{j} \times \mathbf{B}}{ne} - \frac{\nabla \cdot \overleftrightarrow{\mathbf{p}_e}}{ne} \tag{2.21}$$

The left hand side is the Ohm's law from ideal MHD. The terms on the right hand side represent, in order, resistive dissipation, the effect of nonzero electron inertia, the Hall effect, and ambipolar effects from anisotropic electron pressure.

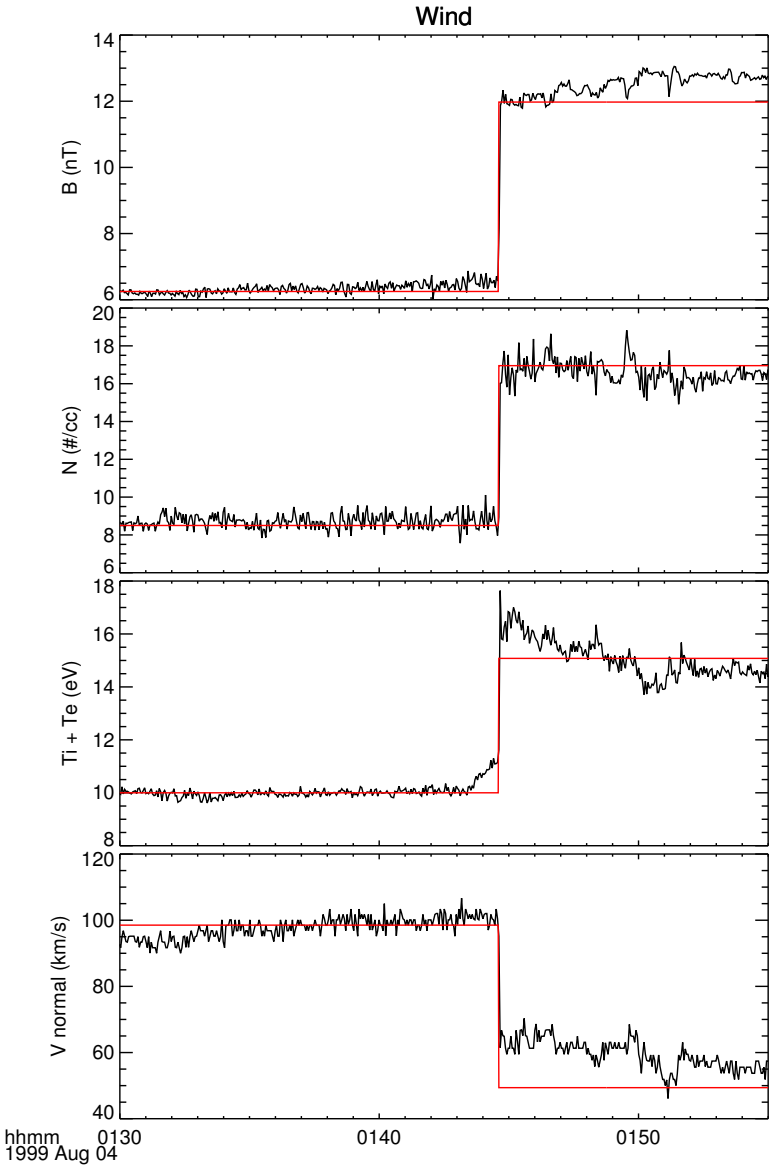

Figure 2.6: Rankine-Hugoniot relations at a typical interplanetary shock observed by the *Wind* spacecraft. The black lines show measurements of various plasma parameters by the MAG and 3DP instruments on *Wind*. The temperature plotted is a combination of the ion and electron temperatures, as per the usual single fluid MHD equation. The plotted velocity is the component normal to the shock front. The red lines show the predicted downstream value of the plotted parameter based on the upstream values and shock parameters $(M_{\mathrm{f}}, \theta_{bn}, \gamma) = (1.65, 62.0°, 1.4)$.

It is convenient to parametrize the nonideal terms in the generalized Ohm's law in terms of scale lengths at which the nonideal terms on the RHS become comparable to the terms on the LHS. For problems with typical scale sizes significantly above the scale length for a given term, the term may be ignored.

The scale lengths are obtained from dimensional analysis, where we define a typical length L_0, typical magnetic field B_0, and typical velocity equal to the Alfvén velocity V_A. Then $\nabla \sim 1/L_0$, $\mathbf{j} \approx B_0/(\mu L_0)$, $\partial/\partial t \approx V_\mathrm{A}/L_0$, and the convective electric field is of order $V_\mathrm{A} B_0$.

The scale length L_η for the first term is then equal to $\eta/(\mu_0 V_\mathrm{A})$. The classical value of plasma resistivity due to Coulomb collisions (Spitzer 1962) is given as[3]

$$\eta \approx \frac{\pi e^2 m^{1/2}}{(4\pi\varepsilon_0)^2 (K T_\mathrm{e})^{3/2}} \ln \Lambda \tag{2.22}$$

which for typical solar wind parameters ($V_\mathrm{A} \approx 60$ km/s, $T_\mathrm{e} \approx 7$ eV) implies that η is approximately 10^{-4} Ω·m and the scale length L_η is on the order of a millimeter (Vasyliunas 1975). This argument is simply another way of proving the claim made earlier in the chapter that collisional terms may be entirely ignored in heliospheric shocks. However, plasma wave turbulence generated by a the current generated at a shock can cause particles to scatter, and this scattering can be modeled by using a value for η much larger than the classical value. This effect, known as "anomalous" resistivity, has been calculated for observed levels of shock-associated waves and yields scale lengths which are closer to that of heliospheric shocks (Watt et al. 2002; Büchner & Elkina 2005; Wilson et al. 2007).

Ignoring the partial time derivative and setting the electron inertial term equivalent to the convective term yields

$$V_\mathrm{A} B_0 \approx \frac{m_\mathrm{e}}{n e^2} \frac{V_\mathrm{A} B_0}{\mu L_0^2} \tag{2.23}$$

Therefore, the length on which the electron inertial term plays a large role (in practical terms, this means when a region of current is this size or smaller) is

$$L_0 \approx c \left(\frac{m_\mathrm{e} \epsilon_0}{n e^2} \right)^{1/2} = \frac{c}{\omega_\mathrm{pe}} = \lambda_\mathrm{e} \tag{2.24}$$

which defines the electron inertial length λ_e, also known as the electron skin depth. The electron inertial length is on the order of a kilometer to a few kilometers in the solar wind at 1 AU, which is substantially smaller than the overall scale size of the shock. However, Bale & Mozer (2007) have recently observed that large electric fields exist both

[3] $\ln \Lambda$ here represents the Coulomb logarithm, which represents a cutoff in the maximum distance over which two particles experience Coulomb collisions, and is taken here as approximately equal to 25. More detailed calculations of both η (Spitzer 1962) and $\ln \Lambda$ (Cranmer et al. 2009) are available, but are not necessary to show that classical resistivity plays no role in an interplanetary shock.

perpendicular to and parallel to the magnetic field in the terrestrial bow shock on scale sizes similar to the electron inertial length.

The same dimensional analysis performed on the Hall term yields

$$V_{\mathrm{A}} B_0 \approx \frac{B_0^2}{ne\mu L_0} \tag{2.25}$$

so the important length scale is

$$L_0 \approx c\left(\frac{m_{\mathrm{p}}\epsilon_0}{ne^2}\right)^{1/2} = \frac{c}{\omega_{\mathrm{pi}}} = \frac{V_{\mathrm{A}}}{\Omega_{\mathrm{i}}} = \lambda_{\mathrm{i}} \tag{2.26}$$

where λ_{i} is known as the ion inertial length, in analogy to the electron inertial length.

Finally, the same dimensional analysis performed on the ambipolar term yields

$$V_{\mathrm{A}} B_0 \approx \frac{1}{L_0}\frac{kT}{e} \tag{2.27}$$

and a length scale of

$$L_0 = \beta_e \frac{V_{\mathrm{A}}}{\Omega_i} = \beta_e \lambda_i \tag{2.28}$$

A more detailed calculation (Zakharov & Rogers 1992) shows that L_0 actually scales with $\beta_e^{1/2}$ and not β_e. Observations of reconnection in the magnetopause support the $\beta_e^{1/2}$ scaling (Scudder et al. 2002). Regardless of whether one uses $\beta_e\lambda_i$ or $\beta_e^{1/2}\lambda_i$ as the scaling relation, the fact that $\beta_e \sim 1$ in the solar wind at 1 AU implies that the ambipolar term can easily be on the order of the ion inertial length.[4]

In the solar wind at 1 AU, λ_{i} is typically several tens of kilometers, which is close to the observed scale length of shocks. However, recent measurements (Bale et al. 2003) have found that density transition scale lengths at quasi-perpendicular shocks more closely correspond not to λ_{i} but to the convected ion gyroradius, which is given by the ratio of the shock speed to the downstream cyclotron frequency $v_{\mathrm{sh}}/\Omega_{\mathrm{ci},2}$.

It is clear from these order of magnitude estimates that we must consider nonideal effects when dealing with shock microstructure. In particular, the environment governing the behavior of electrons in shock fronts is generated by the ion scale terms in the generalized Ohm's law.

2.8 Particle Acceleration

Interest in the physics of collisionless shocks in space plasmas is largely driven by the role that shocks play in particle acceleration. Most of the energetic particle populations

[4]There is a corresponding term in the generalized Ohm's law which represents the ion pressure, but it is a factor of M/m smaller than the electron term and can be ignored.

both in the heliosphere and in astrophysical plasmas are thought to be accelerated by shocks (Jones & Ellison 1991).

The general astrophysical problem of particle acceleration was prompted by early observation of the spectrum of high energy cosmic rays, which varies as a power law over many orders of magnitude in both flux and energy (Amsler, C., *et al.* 2008). It was shown by Fermi that particles undergoing repeated interactions with the galactic magnetic field would lead to a power law distribution (Fermi 1949, 1954), and later Parker studied the mechanism of MHD waves to explain the nature of the interaction between the field and the cosmic ray particles (Parker 1958c).

In the heliosphere, the time and distance scales for interactions of particles with magnetic disturbances are far shorter than those in the galaxy. Nevertheless, energetic particles were detected upstream of the terrestrial bow shock by the first generation of spacecraft capable of making such measurements in the solar wind environment (Asbridge et al. 1968; Anderson 1968). These measurements spurred theoretical research into mechanisms by which a particle can gain energy by interacting with a single shock on a relatively short time scale.

The two mechanisms of shock acceleration which have been most studied in the heliosphere are shock drift acceleration and diffusive shock acceleration (Lee & Fisk 1982; Jones & Ellison 1991; Lee 2000). Shock drift acceleration is more important at quasiperpendicular shocks and tends to produce spiky upstream particle events, while diffusive shock acceleration is more important at quasiparallel shocks and tends to produce relatively smooth increases in energetic particles up to the shock encounter (van Nes et al. 1984; Tsurutani & Lin 1985).

The key insight which led to the first descriptions of diffusive shock acceleration was that turbulence in the upstream and downstream regions of parallel shocks could scatter particles back and forth across the shock. Due to the converging nature of the flow at the shock front the particle would, on average, gain momentum proportional to $u_{\mathrm{nu}} - u_{\mathrm{nd}}$, the difference in plasma flow velocity normal to the shock between the upstream and downstream regions (Fisk 1971; Axford et al. 1977; Bell 1978; Blandford & Ostriker 1978). Taking into account the multi-encounter energy gains as well as the scattering of particles away from the vicinity of the shock leads to power law energy spectra.

The model of diffusive shock acceleration has been observed to be broadly consistent with observed energy spectra of upstream of the quasiparallel terrestrial bow shock (Ellison 1985) and quasiparallel interplanetary shocks (Gosling et al. 1981).

At quasiperpendicular shocks, the mechanism of shock drift acceleration is important in the energization of particles (Armstrong et al. 1985; Decker 1992). Shock drift acceleration relies on the presence of an induced $(-\mathbf{u} \times \mathbf{B})$ electric field in the plasma in the upstream and downstream regions. If the gyroradius of a particle is large enough, its orbit may cross a shock several times. The gradient of the magnetic field across the shock discontinuity changes the gyroradius of the particle, and this change may cause the particle to drift along the front of the shock. Depending on whether the magnetic

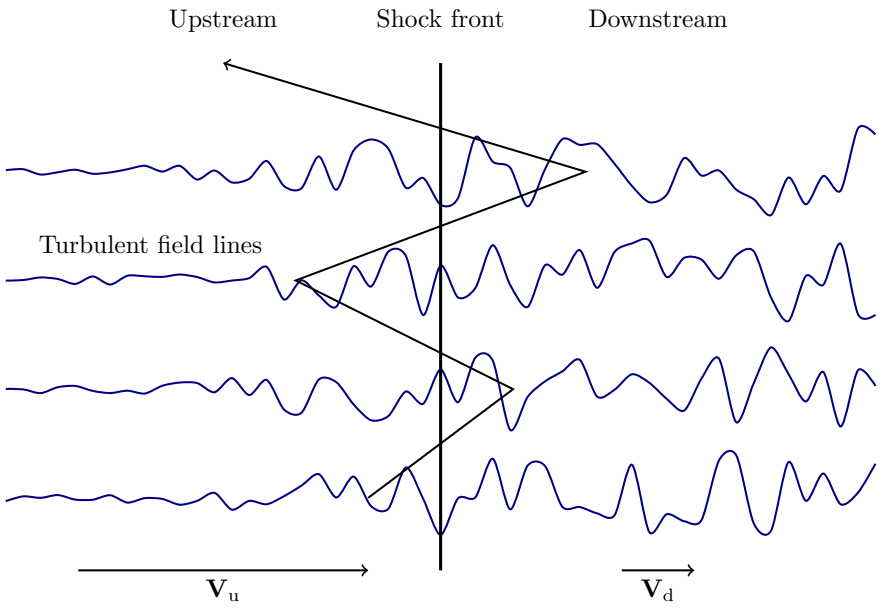

Figure 2.7: Cartoon illustrating diffusive shock acceleration at a parallel shock. A schematic typical path of a shock-accelerated particle is shown. Each encounter with the shock yields an average gain of energy, due to the converging flow velocities at the shock front. (Figure after Lee (2000).)

field increases or decreases across the shock, the particle will drift along the shock front in a direction parallel or antiparallel to the induced electric field of the plasma flow, and will therefore gain or lose energy depending on the sign of the particle charge. Fast mode shocks, which result in increased magnetic field magnitude, lead to energy gains.

Shock drift acceleration has for the past several decades been invoked to explain the spiky and highly time dependent events observed at shocks in the heliosphere (see, *e.g.* Sarris et al. 1976; van Nes et al. 1984; Tsurutani & Lin 1985; Meziane et al. 2002).

More recently, the importance of factors such as shock curvature to the process of shock drift acceleration have been appreciated. Decker (1990) and Giacalone (1992) studied the effects of surface ripples on a shock front, while Erdos & Balogh (1994) studied the effects of curved field lines which intersect the shock at multiple points. From the standpoint of the particle orbit, these effects have a similar result, namely that the particle can be trapped between connection points on the shock surface and accelerated to higher energies than particles which undergo a single drift acceleration process.

Although diffusive shock acceleration and shock drift acceleration are often considered as distinct mechanisms, both are the result of the same basic physical force (the Lorentz

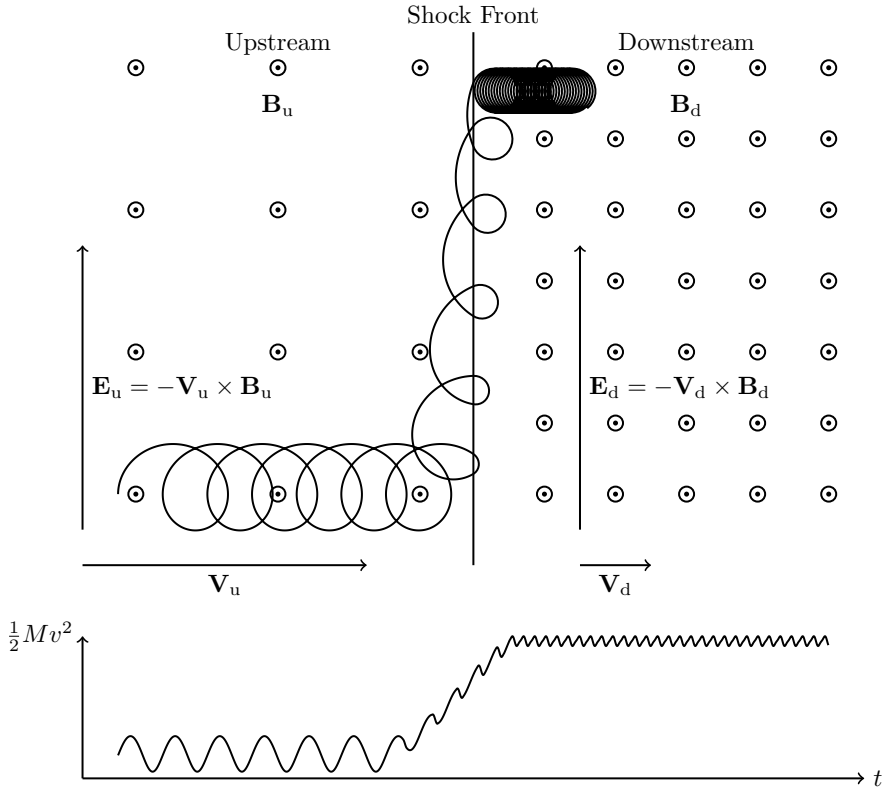

Figure 2.8: Cartoon illustrating shock drift acceleration across a perpendicular fast mode shock. The magnetic field, coming out of the page, increases from upstream to downstream and decreases the gyroradius of the incident particle. The particle continues to drift downstream during its repeated encounters with the shock front, until the particle eventually escapes downstream (it is also possible for the particle to escape in the upstream direction). The bottom panel of the figure shows the kinetic energy of the particle plotted as a function of time, showing how the energy gain occurs in several steps coinciding with the shock encounters. (Figure after Armstrong et al. (1985) and Ball & Melrose (2001).)

force) and the mechanisms often act together to energize particles, a fact emphasized by Decker (1988). Together, these mechanisms have proven greatly successful for the explanation of high energy ion spectra in astrophysical and heliospheric plasmas. However, electron acceleration requires modifications to the basic picture presented in this section. Most importantly, both mechanisms rely on the fact that Larmor radii of accelerated particles are large enough that the shock front seems like a infinitesimal discontinuity, while in fact the width of the shock front is usually on the order of the proton Larmor radius. Therefore, these processes require a 'seed' population of particles which are already relatively highly energized in order for the acceleration mechanisms to be effective. This is a particular problem for electrons, whose Larmor radii are a factor of $\sqrt{M/m}$ smaller than protons at similar energies. For low energy electrons accelerated at shocks, a modified shock drift process known as 'fast Fermi' is the main mechanism believed to energize the particles. This theory will be more fully discussed in the following chapter.

Chapter 3

Electron Acceleration, Plasma Waves, and Radio Emission

The material in this thesis investigates the acceleration of electrons at heliospheric shocks, and the radio waves that are generated by those accelerated electrons. In this chapter, the physical mechanisms behind these phenomena are introduced.

3.1 Radio Observations

The first observations of solar radio emission were made via ground-based radio spectrometers, which measured radio waves in the metric ($\sim$1-20 m) wavelengths. The solar radio output in these wavelengths was observed to be dominated by bursty emissions, where the time scale for the bursts varied from seconds to minutes, sometimes occurring in storms which lasted up to several days. Further observations revealed a spectrum which included harmonic structure, which was correctly interpreted as $f_{\rm p}$ and $2f_{\rm p}$ radio waves generated by longitudinal electron plasma waves (Wild et al. 1954; Wild 1985).

Space-based instrumentation extended the range of frequencies available for radio observations below the ionospheric plasma frequency, which is on the order of 10 MHz. Since radio bursts are generated at the local plasma frequency, the extension to lower frequencies corresponds to an extension to lower plasma densities and greater distances from the sun in the radially expanding solar wind. Radio bursts observed at these interplanetary distances are known as decametric/hectometric or kilometric bursts, depending on the observed frequency, as opposed to the metric bursts from coronal altitudes.

Although many different types of solar radio bursts exist (see Dulk (1985) for a summary of types and mechanisms of solar radio emission), the primary types of interest for space-based plasma wave instrumentation are the radio bursts known as Type IIs and Type IIIs, since these types often extend to interplanetary frequencies that cannot

be observed from terrestrial stations. The Type II radio burst is associated with shocks generated by CMEs, while the Type III burst is associated with electron beams generated by solar flares.

In addition to the solar radio measurements, space-based instrumentation also offered the first *in situ* measurements of shock-accelerated electrons and the locally generated plasma waves. The curved topology of the terrestrial bow shock and the nature of its interaction with the solar wind magnetic field implies that there is almost always some location on the shock that is favorable for electron acceleration and subsequent radio emission. The theory and observations behind this phenomenon are discussed further later in this chapter.

Several distinct steps are required for a disturbance to generate radio emission. The steps in this "signal chain" are illustrated in Figure 3.1. First, a supersonic moving disturbance is generated in a plasma, either by an explosive event or by the steady flow of plasma around an object. In Figure 3.1, the examples of a CME and of the interaction of the solar wind with a magnetized body are symbolically shown. The disturbance generates waves which steepen into collisionless shocks. The shocks then reflect and accelerate electrons in a process known as Fast Fermi acceleration, and the accelerated electron beam is sent back upstream of the shock into the solar wind. The reflected electron beam is unstable to the Landau resonance, and generates electrostatic plasma oscillations known as Langmuir waves. The Langmuir waves in turn generate electromagnetic radio waves via a mode conversion process.

This chapter is primarily concerned with reviewing the several processes involved in the signal chain represented in Figure 3.1. This discussion is preceded by a section which contains some background on the solar wind electrons, which are the seed population for the acceleration, and it is followed by a discussion of the use of quasi-thermal antenna noise as a diagnostic of the solar wind plasma.

3.2 Solar Wind Electrons

We begin by considering the properties of the source population of solar wind electrons. The distribution function of solar wind electrons deviates from a Maxwellian distribution, since the collisional mean free path in the solar wind is long. The solar wind electron distribution function can be quantitatively described by a multi-component model. The densest and coldest component of the solar wind is known as the core. The core electrons make up more than 90% of the number density of solar wind electrons, with a typical density of roughly 7.1 cm^{-3} and temperature of 1.3×10^5 K for the slow solar wind, and a density of roughly 2.8 cm^{-3} and temperature of 1×10^5 K in the fast solar wind (see Table 3.1). The core can be reasonably well approximated by a bi-Maxwellian distribution, which is a Maxwellian distribution with separate temperatures $(T_\parallel, T_\perp)$ in the directions parallel and perpendicular to the magnetic field.

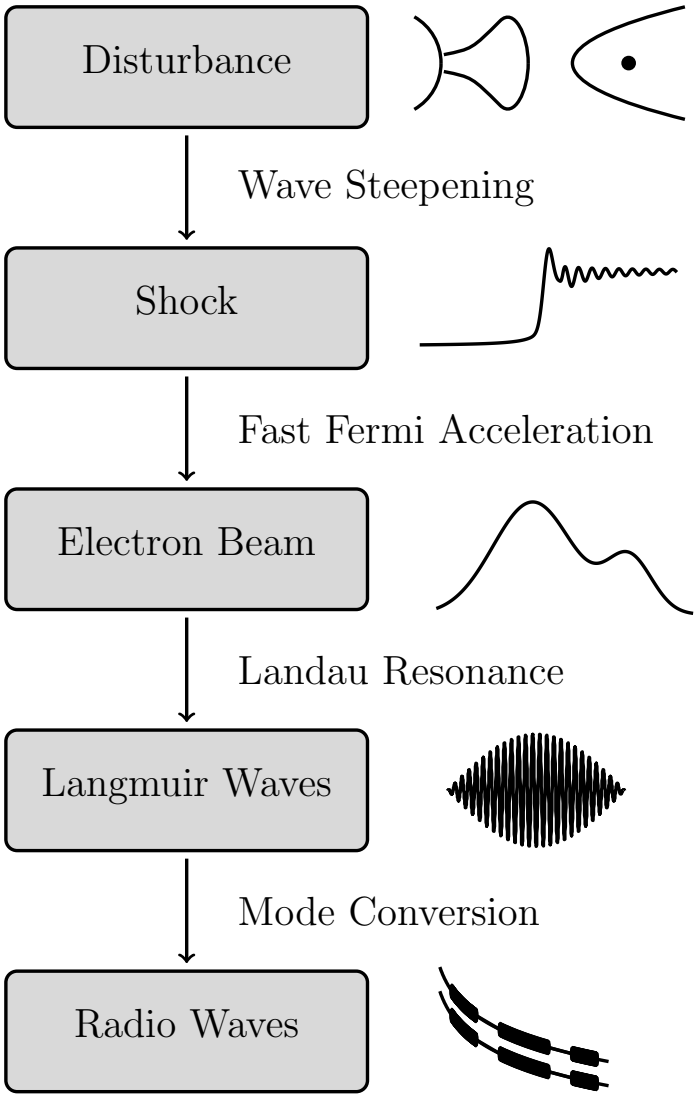

Figure 3.1: Signal chain for generation of radio emission at the plasma frequency by shock accelerated electrons. Each block represents an phenomenon observable either remotely or *in situ*, and each arrow represents the process by which a link in the signal chain is generated by the link above. The small icons to the right of the boxes show schematic representations of (from top): a CME or magnetosphere/solar wind interaction region, the magnetic field jump across a shock crossing, a parallel cut through the distribution function of shock-accelerated electrons, the electric field observed in a Langmuir wave, and the drifting radio signal of a Type II radio burst.

The non-Maxwellian, or nonthermal, components of the solar wind include the halo and the strahl. The halo can also be approximated by a bi-Maxwellian distribution with a typical number density of about 5% of the core number density and a typical temperature of about 8 times the core temperature. The bulk velocity calculated from the bi-Maxwellian distribution for the halo is often offset from the core bulk velocity by several hundred kilometers per second (Feldman et al. 1975; Pilipp et al. 1987). Although the bi-Maxwellian distribution fits the halo well at low frequencies, the fit becomes worse at high energies, where a high energy power law tail exists. Maksimovic et al. (2005) found that a bi-kappa distribution function provided a superior fit for the high energy tail of the halo electrons.

The kappa distribution, first introduced by Vasyliunas (1968) as an empirical description of the distribution function of magnetospheric electrons, is a modification of the Maxwellian distribution function which resembles a Maxwellian at low energies but at high energies becomes a power law with an index κ. The κ parameter generally ranges from 4 to 5 at 1 AU for the nonthermal components of the solar wind electron distribution (Štverák et al. 2009).[1]

The bi-kappa distribution is, like the bi-Maxwellian distribution, an extension of the isotropic distribution to include the effects of separate parallel and perpendicular temperatures. Expressions for the core bi-Maxwellian and halo bi-kappa distribution from Štverák et al. (2009) are:

$$f_{\mathrm{c}}(v) = n_{\mathrm{c}} \left(\frac{m}{2\pi k}\right)^{3/2} \frac{1}{T_{\mathrm{c}\perp}\sqrt{T_{\mathrm{c}\parallel}}} \exp\left[-\frac{m}{2k}\left(\frac{v_\perp^2}{T_{\mathrm{c}\perp}} + \frac{v_\parallel^2 - \Delta_{\mathrm{c}}}{T_{\mathrm{c}\parallel}}\right)\right] \tag{3.1}$$

$$f_\kappa(v) = n_{\mathrm{h}} \left(\frac{m}{\pi k(2\kappa-3)}\right)^{3/2} \frac{1}{T_{\mathrm{h}\perp}\sqrt{T_{\mathrm{h}\parallel}}} \frac{\Gamma(\kappa+1)}{\Gamma(\kappa-1/2)} \times \left(1 + \frac{m}{k(2\kappa-3)}\left(\frac{v_\perp^2}{T_{\mathrm{h}\perp}} + \frac{v_\parallel^2}{T_{\mathrm{h}\parallel}}\right)\right)^{(-\kappa-1)} \tag{3.2}$$

The core and halo components of the solar wind also display anisotropy, which is generated by adiabatic focusing and mediated by collisions. Salem et al. (2003) calculated the collisional age A_{e} of solar wind electrons, where A_{e} represents the average number of Coulomb collisions that a solar wind electron will make during the transport of the solar wind from the low corona to the observation point (1 AU for the *Wind* data studied in Salem et al. (2003)). The collisional age ranges from 2 to several hundred, and is inversely correlated with the anisotropy $T_\parallel/T_\perp$ of the solar wind electrons.

[1]It should be noted that there exist two slightly different definitions for the kappa distribution, one with an exponent of $-\kappa$ and one with an exponent $-\kappa-1$, as discussed by Livadiotis & McComas (2009). In this thesis the second and most commonly encountered definition is used.

Property	Value
n [cm^{-3}]	7.1 (slow wind), 2.8 (fast wind)
T [10^5 K]	1.3 (slow wind), 1.0 (fast wind)
v [km/s]	400 (slow wind), 750 (fast wind)
$n_\mathrm{h}/n_\mathrm{c}$	0.04
$T_\mathrm{h}/T_\mathrm{c}$	7.2
$\Delta v_{\mathrm{c-h}}$	1215

Table 3.1: Typical parameters for the core and halo populations of solar wind electrons at 1 AU. Data from Feldman et al. (1975), Hundhausen (1995), and Issautier et al. (2003).

The strahl component (Montgomery et al. 1968; Rosenbauer et al. 1977; Pilipp et al. 1987) of the solar wind electrons, unlike the core and halo, is sufficiently anisotropic that it cannot be modeled with a bi-Maxwellian or bi-kappa distribution. The strahl is a beam-like feature, with the beam moving away from the sun and focused around the magnetic field. The densities of the halo and strahl suprathermal populations display complementary radial variation, with the density of the strahl decreasing while the density of the halo increases. The sum of the two suprathermal populations remains nearly constant, suggesting that the strahl evolves into the halo, possibly via a collisional or wave-particle scattering mechanism (Maksimovic et al. 2005; Štverák et al. 2009). The core, halo, and strahl populations are illustrated in Figure 3.2, which shows parallel and perpendicular cuts through a solar wind electron distribution function.

In addition to the core, halo, and strahl electron populations, there exists a fourth quiet time component known as the superhalo, with a hard spectrum from ~ 2 keV to ~ 100 keV. The superhalo is nearly isotropic with a slight anisotropy in the sunward-flowing direction, suggesting the possibility of a source beyond 1 AU rather than a solar origin. However, these observations are marginal, and the origin of the superhalo remains an open question (Lin et al. 1996; Lin 1998).

3.3 Electron Acceleration: The Fast Fermi Model

It is more difficult for a collisionless shock to accelerate an electron to higher energies than it is to energize an ion, a fact that is due to the relative size of the electron and ion Larmor radii. At a sharp discontinuity such as a shock wave, ions in the plasma will become unmagnetized, that is, their paths will no longer follow the guiding center of the magnetic field. This demagnetization frees the ion to scatter back and forth across the

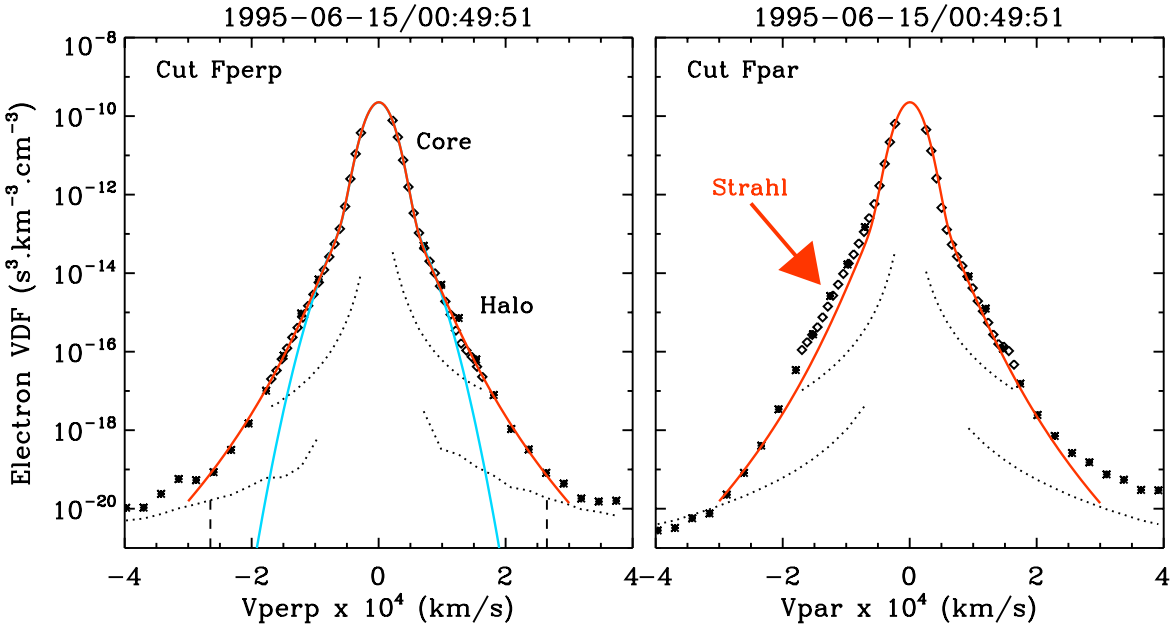

Figure 3.2: Parallel and perpendicular cuts through a solar wind electron distribution function observed by *Wind*/3DP. The cyan line on the left panel shows the bi-Maxwellian core and halo fit, and the red line shows a kappa distribution fit for the halo electrons, which fits much better at higher energies. The superhalo is visible beyond the halo energies at the highest velocities. The right panel shows the parallel-aligned electron strahl. The dotted lines indicate the one count levels for EESA-L at low energies, and EESA-H at high energies. *Figure courtesy of Chadi Salem.*

shock, and this scattering is the basis of the stochastic acceleration processes outlined in the previous chapter. Similarly, in the shock drift process, ions gain energy as their large Larmor radius brings them into contact with the shock front multiple times.

However, the Larmor radius $r_{\rm L}$ of an electron is a factor $\sqrt{M/m} = 42.8$ times smaller than that of a proton with the same kinetic energy, and therefore remains smaller than the scale sizes of the shock crossing. Since the electron Larmor radius remains small, the magnetic moment μ of the electron remains well defined as $\mu = IA$, where I is the current generated by the Larmor motion of the electron ($I = e\omega_{\rm c}/2\pi$) and A is the area of the circle with radius equal to the Larmor radius ($A = \pi v_\perp^2/\omega_{\rm c}^2$.) It can be shown (see, e.g., Bellan 2006) that the first adiabatic invariant $\mu = mv_\perp^2/2B$ is conserved provided the total change in magnetic field during an orbit is much smaller than the average magnetic field over the orbit. Conservation of μ implies that when a particle moves into a region of space where the magnetic field is increasing, its perpendicular velocity must also increase. Energy conservation mandates that this increase must come at the expense of the parallel

velocity. If the increase in magnetic field is sufficiently large, the parallel velocity can decrease to zero, and the particle can reverse direction. This process, known as magnetic mirroring, is illustrated in Figure 3.3. The jump in field at a fast mode shock front can serve as a magnetic mirror for the upstream electrons. Whether an individual electron is reflected by the mirror depends on the pitch angle α ($\cos\alpha = \mathbf{v}\cdot\mathbf{B}/vB$) of the particle and the relative strength of the magnetic field in the upstream region and in the shock front.

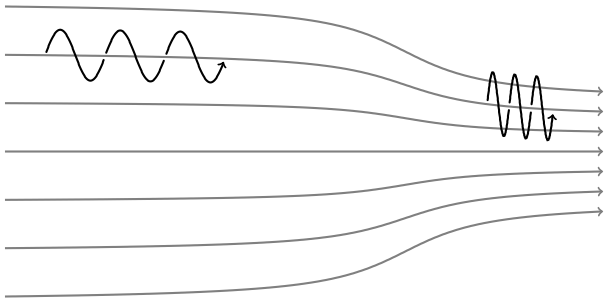

Figure 3.3: Cartoon illustrating the magnetic mirroring of a gyrating particle moving from a region of low magnetic field to a region of higher magnetic field.

Calculation of the mirror process is most easily tractable in a frame where there is no upstream convective electric field, which implies that the velocity and magnetic field vectors are parallel. This frame is known as the de Hoffmann-Teller (HT) frame (de Hoffmann & Teller 1950). The transformation velocity from any frame in which the shock is stationary to the HT frame is:

$$\mathbf{v}_{\rm HT} = \frac{\hat{\mathbf{n}}\times(\mathbf{v}_1\times\mathbf{B}_1)}{\mathbf{B}_1\cdot\hat{\mathbf{n}}} \tag{3.3}$$

where $\mathbf{v}_1$ and $\mathbf{B}_1$ are the observed velocity and magnetic field in a shock-stationary frame. Equation 3.3 shows that $\mathbf{v}_{\rm HT}$ is perpendicular to $\hat{\mathbf{n}}$; that is, the transformation lies in the plane of the shock, so the shock is still stationary in the HT frame.

The advantage of moving to the HT frame is that the electron reflection process for an electron with a given parallel and perpendicular velocity is greatly simplified, and depends only on the upstream magnetic field, the maximum magnetic field encountered in the shock front, and the electrostatic potential across the shock which arises from the differential motion of ions and electrons through the shock.[2] This process is known as 'Fast Fermi' acceleration (Leroy & Mangeney 1984; Wu 1984), and is reviewed in

[2]Of course, the actual physical process does not depend on which frame we choose for analysis, and it has been shown that the HT analysis is equivalent to a shock drift acceleration process with a single shock encounter (Krauss-Varban & Wu 1989).

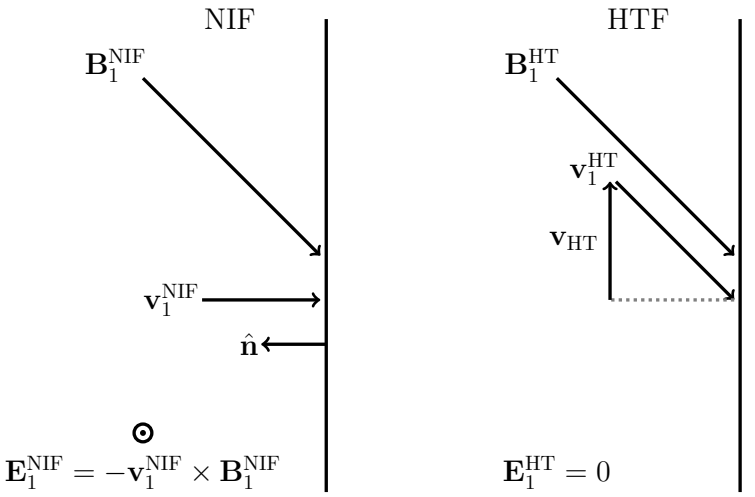

Figure 3.4: Diagram illustrating geometry of the normal incidence frame and the de Hoffman-Teller frame. Only the upstream $\mathbf{B}$ and $\mathbf{v}$ vectors are shown. From Equation 3.3, it is clear that the $\mathbf{v}_{\mathrm{HT}}$ is perpendicular to the shock normal and lies in the same plane as $\mathbf{v}_1$ and $\mathbf{B}_1$. The $-\mathbf{v} \times \mathbf{B}$ electric field is zero in the HT frame, where $\mathbf{v}_1$ and $\mathbf{B}_1$ are parallel.

more detail in Chapter 6. Fast Fermi theory, applied to a bi-Maxwellian (core and halo) population of solar wind electrons, predicts the following results (Krauss-Varban et al. 1989) for the average energy of a reflected electron and the number of reflected electrons relative to the halo population (most of the core is typically not reflected due to the effect of the cross shock potential):

$$\langle E_{\mathrm{r}\parallel} \rangle \sim \frac{4}{\cos^2 \theta_{\mathrm{bn}}} \frac{1}{2} m_{\mathrm{e}} v_1^2 \tag{3.4}$$

$$\begin{aligned} \frac{n_{\mathrm{r}}}{n_{\mathrm{h}}} = \frac{1}{2} \left(\frac{\Delta B}{B_{\mathrm{max}}} \right)^{1/2} & \left[1 + \mathrm{erf} \left(\frac{v_1'}{v_{\mathrm{h}}} \left(\frac{\Delta B}{B_{\mathrm{max}}} \right)^{1/2} \right) \right] \\ & \times \exp \left(- \frac{B_1}{B_{\mathrm{max}}} \left(\frac{v_1'}{v_{\mathrm{h}}} \right)^2 - \frac{2e\Phi'}{m_{\mathrm{e}} v_{\mathrm{h}}^2} \frac{B_1}{\Delta_B} \right) \end{aligned} \tag{3.5}$$

The first two panels of Figure 3.5 shows plots of Equations 3.4 and 3.5, illustrating one of the main predictions of Fast Fermi theory: that the energy of reflected electrons is greatest when the shock is very close to perpendicular, but the number of reflected electrons drops. The third panel plots the product of the first two panels, and is a rough

estimate of the energy in the beam of reflected electrons. The energy in this beam is the source of the free energy that will drive the growth of the Langmuir waves that will be discussed in the following section. The beam energy peaks at a value of $\theta_{\rm Bn}$ which is almost perpendicular.

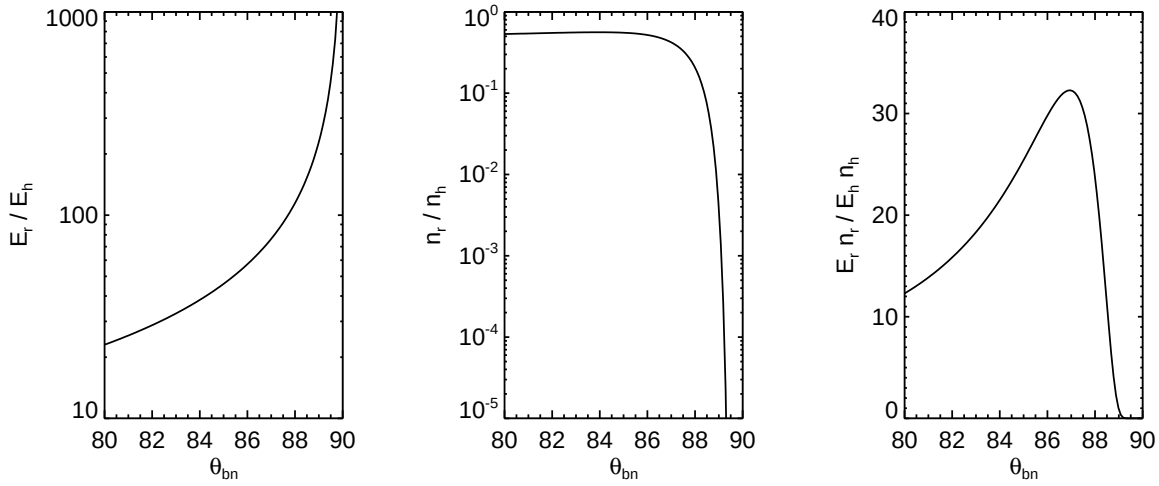

Figure 3.5: Plots illustrating Fast Fermi electron acceleration at nearly perpendicular shocks. The panels show, as a function of $\theta_{\rm Bn}$, the average energy of a reflected electron compared to the average energy of a halo electron, the number of electrons reflected normalized to the number of halo electrons, and the product of the normalized energy and normalized number, which is a rough measurement of the energy of the beam. The first and second panels are similar to Figures 4 and 5 of Krauss-Varban et al. (1989).

3.4 Electron Beams and Landau Resonance

Langmuir waves, also known as electron plasma waves, correspond to a fundamental electrostatic oscillation mode in a plasma. These waves were among the first plasma phenomena to be discovered and investigated (Tonks & Langmuir 1929; Bohm & Gross 1949). Langmuir waves can be qualitatively described by considering a neutral plasma in a fixed volume, and examining the response if all of the electrons are shifted a small distance from their original position. A restoring force arises in the form of the electric field generated by the charge separation, and the resulting oscillation has the characteristic frequency $f_{\rm p} \approx 9000\sqrt{n}$ Hz.

In the heliosphere, Langmuir waves are generated and damped from a collisionless exchange of energy between particles and waves. The relevant equations are the Vlasov

equation, which relates the distribution function of the plasma to the electromagnetic forces acting on the plasma, and the Poisson equation, since the Langmuir waves are driven by electrostatic forces resulting from inhomogeneities in charge density.

Because Langmuir waves are electrostatic, the Lorentz force in the Vlasov equation includes only the electric field term. We also ignore any collisional terms. With these assumptions, the Vlasov and Poisson equations are given by:

$$\frac{\partial f}{\partial t} + \mathbf{v} \cdot \nabla f + \frac{e}{m}\mathbf{E}_1 \cdot \frac{\partial f}{\partial \mathbf{v}} = 0 \tag{3.6}$$

$$\epsilon_0 \nabla \cdot \mathbf{E}_1 = -e n_1 \tag{3.7}$$

where f refers to the electron distribution function (the high frequency of Langmuir waves means that we can treat the massive ions as a motionless background charge density which causes the average net charge to vanish) and $\mathbf{E}_1$, and n_1 refer to the perturbation electric field and density.

When these equations are linearized using the standard Fourier method of assuming a plane wave in the x direction with perturbed quantities $\propto e^{i(kx-\omega t)}$, the resulting equation is (see, e.g., Chen 2006, Chap. 7)

$$1 = -\frac{e}{km\epsilon_0} \int\int\int \frac{\partial f_0/\partial v_x}{\omega - k v_x} d^3v \tag{3.8}$$

The v_y and v_z integrals can be performed assuming a Maxwellian distribution function, which makes the problem one-dimensional so the x subscript may be dropped.

$$1 = \frac{\omega_p^2}{k^2} \int_{-\infty}^{\infty} \frac{\partial \hat{f}_0/\partial v}{v - \omega/k} dv \tag{3.9}$$

It was pointed out by Landau (1946) that the evaluation of 3.9 is not well defined, due to the singularity present at $v = \omega/k$. Landau solved the equation using a Laplace transform and a contour integral, and found that the solution agreed with the Fourier treatment for the real part of ω, but that the presence of a pole in the complex plane corresponding to the singularity resulted in an imaginary component in ω. This implied that, even in a collisionless plasma, wave energy could be lost to (damping) or gained from (resonance) the particle distribution function.

Evaluation of the dispersion function is in general quite complicated, but a simpler result (which agrees reasonably well with observations) can be derived if the assumptions of small ω_i and $\omega \gg kv$ are made (Bellan 2006). In this case, ω_r is be well approximated by the principal value of the integral, which can be integrated by parts with the

denominator Taylor expanded for small kv:

$$1 = -\frac{\omega_{\rm p}^2}{k^2} \int \frac{\tilde{f}_0}{(v-\omega/k)^2} dv \tag{3.10}$$

$$1 = -\frac{\omega_{\rm p}^2}{k^2} \int \frac{\tilde{f}_0}{\omega^2/k^2} \left(1 + \frac{2vk}{\omega} + \frac{3v^2k^2}{\omega^2} + \ldots\right) dv \tag{3.11}$$

This yields a dispersion relation for $\omega_{\rm r}$ which is the same as the dispersion relation obtained from analysis of the fluid equations.

$$\omega_{\rm r}^2 = \omega_{\rm p}^2 + 3k^2 v_{\rm th}^2 \tag{3.12}$$

Using the same assumptions as above, ω_i is calculated from the residue of the Landau integration contour.

$$\omega_{\rm i} = i\omega_{\rm p} \frac{\pi}{2} \frac{\omega_{\rm p}^2}{k^2} \left[\frac{\partial f}{\partial v}\right]_{v=v_\phi} \tag{3.13}$$

It can be seen from Equation 3.13 that the sign of $\omega_{\rm i}$ depends on the derivative $\partial f/\partial v$ of the distribution function. For a Maxwellian distribution, f always decreases with increasing v, and so electrostatic waves are damped. However, if the value of $\partial f/\partial v$ is positive, the sign of $\omega_{\rm i}$ is reversed and Langmuir waves will grow. A physically intuitive (although simplified) picture of Landau damping imagines individual electrons traveling along with the wave and interacting with the wave field depending on the relative velocity of the electron and the wave. In this picture, electrons moving slightly slower than the wave will gain energy from the wave, and contribute to wave damping, while electrons moving slightly faster will give energy to the wave and contribute to wave growth. Thus the resonance occurs at locations where there are a greater number of electrons moving slightly faster than there are electrons moving slightly slower than the wave.

The top two plots in Figure 3.6 show an undisturbed Maxwellian distribution and a distribution with an added electron beam which is unstable to growth of Langmuir waves. The shaded sections illustrate (top plot) a location where $\partial f/\partial v < 0$ and waves are damped, and (middle plot) a location where $\partial f/\partial v > 0$ and waves will grow.

Landau's prediction of collisionless damping was experimentally verified (Malmberg & Wharton 1964) fifteen years after the first publication of the idea. In space physics, the Landau resonance describes the mechanism responsible for generation of electrostatic Langmuir waves from the electron beams accelerated by shocks (in the electron foreshock, or upstream of IP shocks in the case of Type II radio bursts) or solar flares (as in the case of Type III radio bursts).

The shock-accelerated electron beams, either created by the Fast Fermi mechanism or accelerated by a solar flare (Lin 2005), evolve via a time of flight mechanism. In

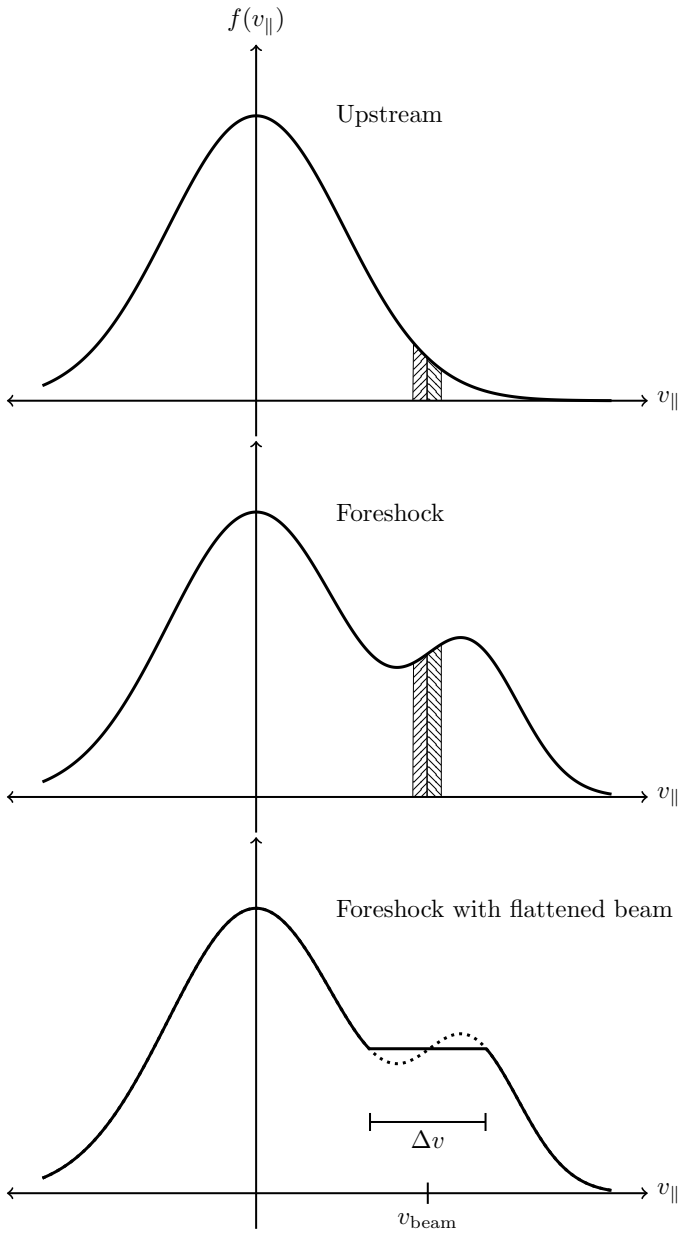

Figure 3.6: Examples of reduced distribution functions: undisturbed, with an electron beam, and with a relaxed beam. The top panel shows a distribution upstream of a shock. The middle panel shows the bump on tail region caused by the accelerated electron beam. The shaded panels show a region unstable to Landau resonance, since the slope of $\partial f/\partial v$ is greater than 0. The final panel shows the reduced distribution after the process of quasilinear damping (see text), illustrating the beam parameters $v_{\rm beam}$ and Δv.

the case of flare-accelerated electrons, the mechanism is temporal velocity dispersion, as the faster electrons outrun the slower electrons as they propagate along a magnetic field line away from the sun (Lin et al. 1981, 1986; Ergun et al. 1998). For electrons at the bow shock, the mechanism is spatial dispersion, in a mechanism described by Filbert & Kellogg (1979). The velocity dispersion in the Filbert and Kellogg mechanism describes the electron beam moving along a field line which is connected to the quasiperpendicular bow shock. As the electrons travel along the field line, the solar wind motional electric field causes the electrons to drift in the antisunward direction, with the slow moving electrons deviating farther from the original field line than the fast electrons. Therefore, at locations very close to the connected field line, only the fast electrons will be present. In both cases, the time of flight mechanism allows the satisfy the condition $\partial f/\partial v > 0$.

A reduced distribution function with a section for which $\partial f/\partial v > 0$ is known as a bump on tail distribution. This bump provides the free energy which leads to the growth of the Langmuir waves as described by Landau. The actual modification of the electron distribution function can be described as a quasilinear relaxation, which flattens the bump on tail into a quasi-stable plateau (Grognard 1975; Melrose 1986; Robinson 1996; Foroutan et al. 2008). An illustration of a quasi-linearly damped distribution function is shown in the bottom plot of Figure 3.6. The velocity of the beam v_{beam} and its width Δv can be estimated from the width of the observed plateau.

The growth rate of the waves can be evaluated, and for typical values in the solar wind at 1 AU the growth rate is a significant fraction of the plasma frequency, meaning that the waves will quickly (on the order of milliseconds) act to smooth out the bump on tail. This fact has important observational implications. Given that the time resolution of plasma instruments is usually on the order of seconds, it should be difficult to resolve bump on tail structures in observed distribution functions. Bump-on-tail distributions have been reported in the electron foreshock with beam velocities about 5 times the electron thermal velocity (Fitzenreiter et al. 1984, 1996), although it is likely that the beams which generate foreshock Langmuir waves have higher relative speeds (Bale et al. 2000).

The rapid growth rate also presented a theoretical problem for Type III radio bursts known as "Sturrock's paradox", which argued that without a mechanism to limit the rate of growth, the waves would quickly exhaust the available free energy in the electron beam (Kellogg 2003). However, observations of radio bursts show that emission often occurs out to 1 AU and beyond. Stochastic growth theory (SGT) (Robinson 1992; Robinson & Cairns 1993; Cairns et al. 2000) describes the wave generation as a random walk process, where the particle distribution fluctuates around a marginally stable state, frequently encountering both regions of wave growth and decay, depending on local solar wind conditions encountered by the electron beam. The quasi-stable distribution can therefore persist for long distances. SGT quantitatively predicts probability distributions for the observed electric fields of the Langmuir waves, and observed distributions for Type III radio bursts (Robinson et al. 1993) and in the terrestrial foreshock (Cairns & Robinson

1999) agree well with the theory.

3.5 Langmuir Wave Structure and Mode Conversion

In space plasmas, Langmuir waves exist in spatially limited regions which are localized and which typically measure 40–100 km transverse to the magnetic field and longer than 150 km in the direction of the magnetic field (Soucek et al. 2009). The electric field of observed Langmuir wave events ranges from tens of mV/m to less than 1 mV/m. The waveforms of the several kHz Langmuir waves are bounded by envelopes with time scales of several to tens of milliseconds. The larger events tend to have relatively smooth envelopes while the smaller events are more patchy (Bale et al. 2000). Two example Langmuir waveforms from the TDS instrument on STEREO/Behind are shown in Figure 3.7.

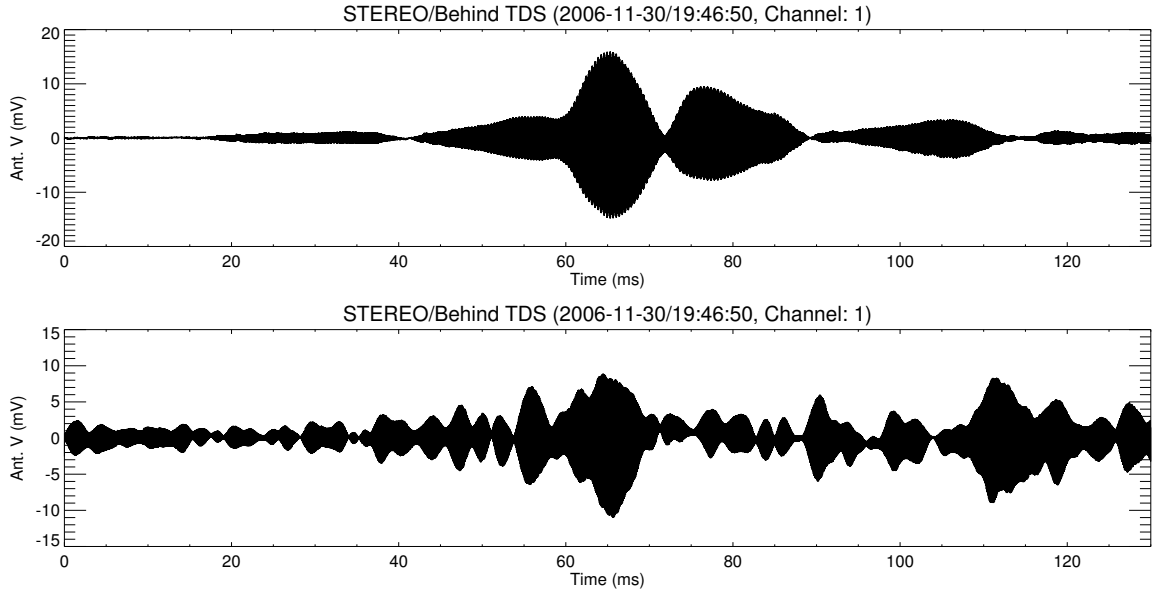

Figure 3.7: Two foreshock Langmuir wave events observed by the TDS instrument on STEREO/Behind.

A number of explanations explaining the nature of Langmuir wave envelopes and the reasons for wave localization have been proposed. (Kellogg et al. 1999b) proposed that since the frequency of Langmuir waves in the solar wind is very close to the local plasma frequency, the waves are sensitive to small fluctuations in the local density and become trapped in regions of low density due to reflection off of density gradients. The observed envelopes of Langmuir wave fluctuations are also consistent with trapped eigenmodes in

regions of lowered density in the solar wind (Ergun et al. 2008). Collapse of Langmuir waves due to ponderomotive force has been essentially ruled out as an important factor in the fate of Langmuir waves, since observations of Langmuir waves do not show any events which are clearly above the threshold of electric field necessary to precipitate collapse (Cairns et al. 1998; Kellogg et al. 1999a).

Observations of solar wind TDS events show more complicated behavior than the purely longitudinal fluctuations associated with electrostatic Langmuir waves, including phase shifts consistent with an interpretation of the waves as transverse z-mode waves (Bale et al. 1998). (In space physics, the z-mode is the name given to the slow branch of the extraordinary wave dispersion function (Benson et al. 2006)). Malaspina & Ergun (2008) found evidence of two- and three-dimensional structure and interpreted it as a consequence of eigenmode structure.

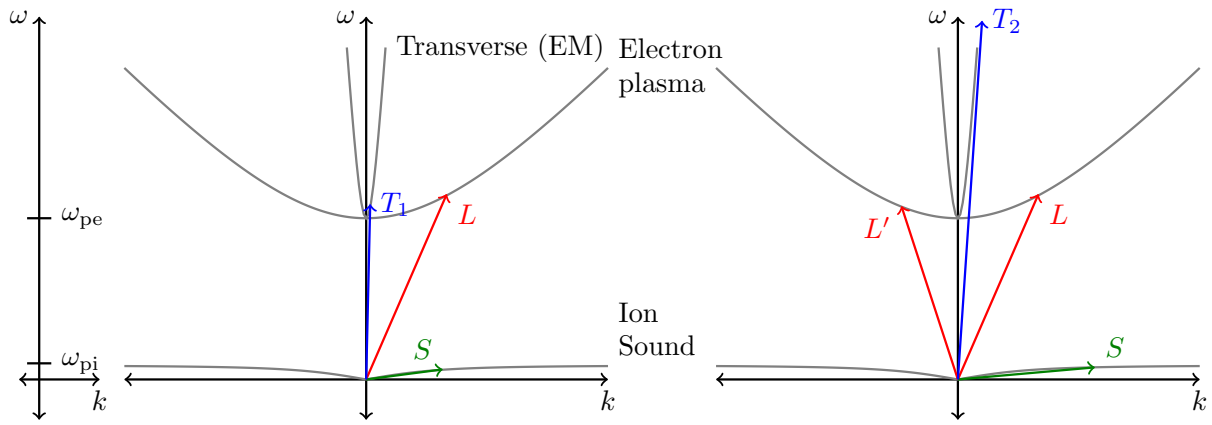

Figure 3.8: Cartoon illustrating the three-wave concept of mode conversion. The dispersion relations for the electron plasma (Langmuir) waves, ion acoustic waves, and transverse electromagnetic waves are shown. The left plot shows the process of generation of fundamental emission, and the right plot shows the generation of harmonic emission.

The Langmuir waves observed in the solar wind do not propagate far from their source regions, and the energy in the waves must be mode converted to electromagnetic radio emission in order to be observed nonlocally. Proposed mechanisms include nonlinear wave-wave interactions and linear mode conversion of z-mode waves. In nonlinear wave-wave mode conversion (Ginzburg & Zhelezniakov 1959; Robinson et al. 1994; Melrose 1986; Robinson & Cairns 1998), radio emission is generated by combinations of waves generated by the beam-driven Langmuir wave L. The dispersion relations for each of the three types of waves involved in the process are shown in Figure 3.8.

The emission of a transverse wave T_1 at the plasma frequency f_p is generated by the reaction $L \rightarrow T_1 + S$ (where S is an ion acoustic wave), shown in the left plot in Figure 3.8. Emission at the harmonic $2f_p$ is produced in a multi-step process. First, a Langmuir

wave L decays into a different 'daughter' Langmuir wave L' and an ion acoustic wave S, $L \rightarrow L' + S$. The harmonic transverse wave T_2 is then produced by $L + L' \rightarrow T_2$, as shown in the right plot in Figure 3.8. Each of the processes described can take place when $\omega_1 \approx \omega_2 + \omega_3$ and $\mathbf{k}_1 \approx \mathbf{k}_2 + \mathbf{k}_3$, where the subscript 1 denotes the wave on the side of the equation with one term and 2 and 3 denote the waves on the other side.

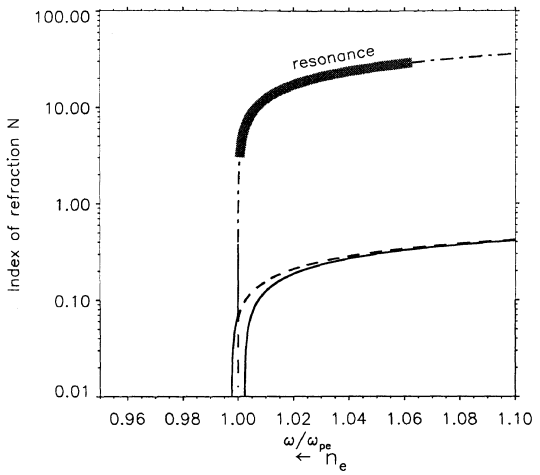

Figure 11. The dispersion relation of electron plasma waves, as index of refraction ($N = kc/\omega$) against ω/ω_{pe}. The dot-dash line is the warm plasma, magnetized Langmuir mode, which meets the electromagnetic z-mode at small N. Waves with beam speeds discussed in this paper have a resonant refractive index marked by the heavy bar. As they propagate into density enhancements, they must move leftward on the curve, and hence down to very small wavenumber.

Figure 3.9: Illustration of the concept of linear mode conversion. Figure from Bale et al. (2000).

The theory of linear mode conversion (Hinkel-Lipsker et al. 1992; Yin et al. 1998; Willes & Cairns 2001; Kim et al. 2008) involves a warm plasma Langmuir wave which is incident on a region of space with a density gradient. The density gradient drives the wavenumber of the magnetized Langmuir wave down until it meets the electromagnetic z-mode branch of the dispersion function. The z-mode wave can then tunnel through to the ordinary electromagnetic branch and propagate freely. Observations of transverse components of Langmuir waves in the foreshock suggest the presence of z-mode waves and the possibility of linear mode conversion as the source of the foreshock radio emission (Bale et al. 1998, 2000).

Recently, Malaspina et al. (2010) have described a new mechanism based on treating Langmuir waves trapped as eigenmodes in density cavities as radiating antennas. Using measured distributions of electric field strength and of the spatial scale of Langmuir

waves, Malaspina et al. (2010) suggest that most of the observed emission in the terrestrial foreshock may come from a small minority of emitting regions.

3.6 Radio Bursts, CMEs, and Shock Tracking

The final result of the signal chain introduced at the beginning of this chapter is the emission of transverse waves in planetary foreshocks or solar radio bursts. One of the primary drivers of interest in heliospheric radiofrequency measurements is the fact that the properties of the emission yield remote observations of phenomena which cannot be studied by other means.

By measuring the drift rate of radio bursts, and assuming a radial density relation in the solar wind, the propagation of an electron beam (for a Type III burst) or of a CME-driven shock (for a Type II) can be measured. In addition, the technique of direction finding (Lecacheux 1978; Ladreiter et al. 1994; Reiner et al. 1998a; Cecconi et al. 2008) can be used to determine the source location directly from the observed radiation. However, these techniques, as well as any other study of radio emission, must take into account the local processes which generate the radio waves. Applications of these techniques to the problem of radiation from shocks upstream of CMEs (Type IIs) is discussed further in Chapter 6, along with radio spectrograms for several Type II events.

The *in situ* study of the shocks, electron beams, and Langmuir waves that are responsible for remotely observed events is useful because it can explain exactly where and how the radiation is produced. Chapters 5 and 6 present results at interplanetary shocks which characterize the properties of Type II source regions, and Chapter 7 uses observations of electrons in the foreshock to evaluate the standard explanation of Fast Fermi electron acceleration.

3.7 Thermal Noise

The thermal motion of an individual electron in the plasma near a spacecraft antenna generates an electric field signal on the antenna. The combination of signals from all of the electrons in the local electron distribution function results in a spectrum known as the quasi-thermal noise (QTN) spectrum, where the 'quasi' emphasizes the fact that the electron distribution functions are generally non-Maxwellian. Unlike measurements of phenomena like Langmuir waves and radio emission, which exist in the plasma regardless of whether a spacecraft is present to measure them, the QTN spectrum is inherently dependent upon the properties of the measuring antenna itself.

The development of QTN spectroscopy in a form applicable to spacecraft antenna has a long history (Fejer & Kan 1969; Meyer-Vernet 1979; Couturier et al. 1981); the background and major results are presented in the review paper by Meyer-Vernet & Perche (1989). The usefulness of QTN spectroscopy derives from the fact that electron plasma

properties (in particular, the density and temperature) can be effectively measured by analyzing the shape of the QTN spectrum. QTN results agree well with the results obtained by conventional plasma detectors and exhibit less susceptibility to the spacecraft potential and photoelectron effects (Maksimovic et al. 1995; Issautier et al. 1999, 2005), making QTN measurements an effective complement to standard plasma measurements.

The measured QTN spectrum for a long, thin wire antenna such as the *Wind*/WAVES spin plane antennas shows three separate regimes: a flat spectrum below the plasma frequency $f_{\rm p}$, a prominent peak at around $f_{\rm p}$, and a power law tail above $f_{\rm p}$ (See Figure 3.11).

The difference between the high and low frequency regimes can be explained simply by considering the typical impact parameter p beyond which an electron will not generate a voltage signal on the antenna (Meyer-Vernet & Perche 1989). At low frequencies $f \ll f_{\rm p}$, p is given by the Debye length $p = \Lambda_{\rm D} = \sqrt{T/m}/\omega_{\rm p}$. At high frequencies $f \gg f_{\rm p}$, the typical impact parameter can be approximated using the dispersion relation for electron plasma waves, $\omega^2 = \omega_{\rm p}^2 + 3k^2T/m$ (see, e.g., Bellan 2006, Chap. 5), which for large ω results in a typical impact parameter p of $1/k \approx \sqrt{3T/m}/\omega$ (see Figure 3.10).

Each electron encounter can then be represented as a short voltage pulse of height $V_{\rm e} \sim e/4\pi\varepsilon_0 p$ and duration $\Delta t \sim p/v_{\rm t}$, where $v_{\rm t}$ is the electron thermal velocity:

$$V_{\rm e}(t) \approx \frac{e}{4\pi\varepsilon_0 p} \exp\left[-\frac{tv_{\rm t}}{p}\right] \tag{3.14}$$

The signal of an individual time domain pulse in the power spectral domain is therefore

$$\tilde{V_{\rm e}^2}(\omega) \approx \left(\frac{e}{4\pi\varepsilon_0 p}\right)^2 \frac{p}{2v_{\rm t}} \exp\left[-\frac{1}{2}\left(\frac{\omega p}{v_{\rm t}}\right)^2\right] \tag{3.15}$$

The overall observed power spectrum $\tilde{V}^2(\omega)$ is the sum of all of the electrons within a distance p, $n_{\rm e}p^3$. By our definitions of p, it is clear that the exponential term in Equation 3.15 is $O(1)$ (i.e., the majority of the spectral power comes from electrons whose impact parameter is close to the antenna). With these simplifications, it is possible to show that the spectral power is proportional to $n_{\rm e}p^2/v_{\rm t}$.

$$\tilde{V}^2(\omega) \sim \begin{cases} n_{\rm e}v_{\rm t} & \omega < \omega_{\rm p} \\ n_{\rm e}v_{\rm t}\left(\dfrac{\omega_{\rm p}}{\omega}\right)^2 & \omega > \omega_{\rm p} \end{cases} \tag{3.16}$$

This brief discussion is only intended to show that the spectral behavior is quite different above and below the plasma frequency. To calculate the spectrum correctly, especially in the vicinity of $f_{\rm p}$, it is necessary to explicitly calculate the response of the antenna to the electron fluctuation spectrum, taking into account the multi-component

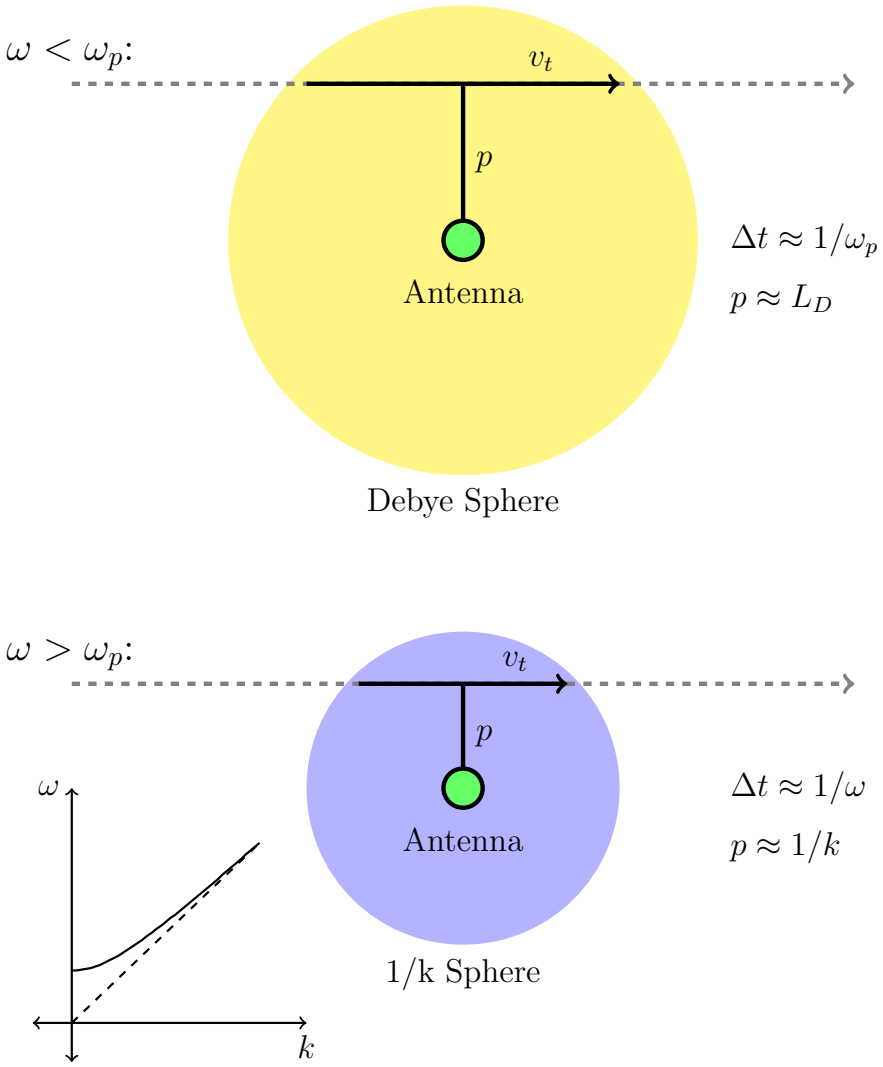

Figure 3.10: Two regimes of electron antenna noise.

nature of the distribution function and the antenna mechanical and electrical properties (Meyer-Vernet & Perche 1989). This calculation yields a prominent peak which lies between the flat low frequency spectrum and the power law tail. The full calculation also takes into account the length of the antenna, in the case of a long thin wire antenna like the *Wind*/WAVES antennas. The signal received on the antenna is attenuated when the antenna is longer than v_t/ω, which leads to a $1/\omega^3$ power law at high frequencies. A schematic thermal noise spectrum is shown in Figure 3.11. The formulae for the high and low frequency regimes, and for the height of the plasma peak, are from Table 1 of Meyer-Vernet & Perche (1989).

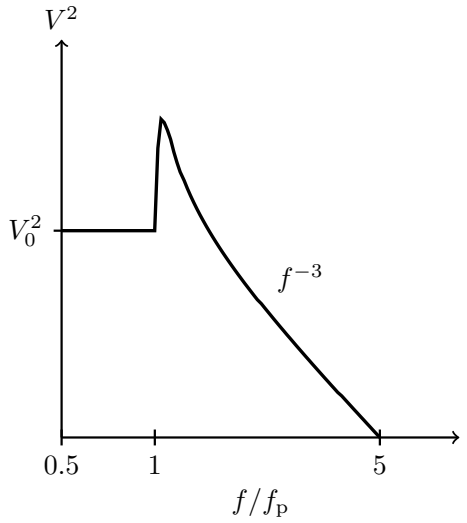

Figure 3.11: Schematic thermal noise spectrum, showing the flat response below the plasma frequency, the plasma peak, and the power law behavior above the plasma frequency. (See Meyer-Vernet & Perche (1989), Figure 2.)

Figure 3.12 shows actual spectra measured by the *Wind*/WAVES antenna. In addition to the electron thermal noise, the measured spectra include Doppler-shifted ion noise and shot noise from electrons colliding with the antenna (Issautier et al. 1999). (In the case of three-axis stabilized spacecraft such as STEREO, the antennas are shorter and wider than the wire booms on *Wind*, and the shot noise signal can dominate the noise spectrum (Zouganelis et al. 2010).)

The left panel of Figure 3.12 shows a typical thermal noise spectrum in the absence of Langmuir waves or radio emission. From the location of the peak, the plasma frequency and density can be determined easily, although to achieve the highest accuracy the full spectrum should be fitted (Maksimovic et al. 1995; Issautier et al. 1999). The plasma peak at around 2.0×10^4 Hz implies a plasma density of around 4.9 cm^{-3}. The right

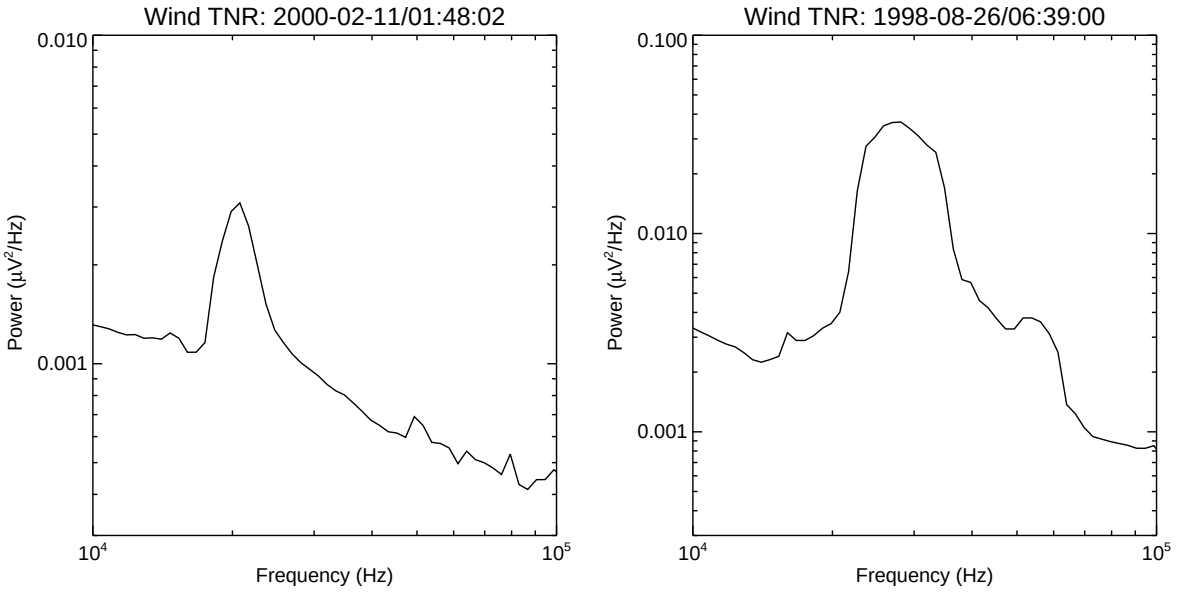

Figure 3.12: Left: A typical thermal noise spectrum measured in the solar wind by the *Wind*/WAVES instrument. Right: A spectrum from the same instrument during a period of strong Langmuir wave activity. Note the vertical scale implying a much greater electric field amplitude, and the presence of the second harmonic at approximately twice the peak frequency.

panel shows a spectrum when intense Langmuir waves are present. The Langmuir wave includes an intense peak at $f_{\rm p} \approx 2.5 \times 10^4$ Hz and a harmonic peak at $2f_{\rm p} \approx 5 \times 10^4$ Hz, implying a plasma density of around 7.7 cm^{-3}. Examples of spectrograms containing foreshock Langmuir waves are shown in Chapters 5, 6 and 7.

Chapter 4

Instrumentation

The results presented in this thesis are based on data from the thermal and suprathermal plasma, magnetic field, and plasma wave detectors on board the *Wind* and STEREO spacecraft. This chapter consists of brief descriptions of the two spacecraft and the relevant instruments. The scientific payload for STEREO shares considerable heritage with the earlier *Wind* payload, and therefore the description of the instrumentation will be joint, except where noted.

4.1 Wind and STEREO

The *Wind* spacecraft was launched on November 1, 1994, as part of the International Solar Terrestrial Physics (ISTP) program. The goal of the ISTP program was to send probes to various regions of the near Earth heliospheric environment and monitor the transport of energy and momentum from the Sun to the Earth. Global Geospace Science (GGS) was a NASA-provided component of ISTP which focused on the study of the interaction of the solar wind with the local geospace environments including the terrestrial bow shock, the magnetosphere, and the magnetotail (Acuña et al. 1995). In addition to *Wind*, which was launched to study the plasma environment upstream of the bow shock, the GGS program included the POLAR mission, which measured the energy input to the auroral regions near the Earth's poles via imaging and *in situ* measurements, and supported analysis of the Geotail mission which studied the magnetotail.

Wind was launched into a dual lunar swingby orbit, which used gravitational encounters with the Moon to alter the original post launch petal orbit, gradually pushing the apogee farther from the Earth to eventually achieve its final destination, the L1 Lagrangian point between the Sun and the Earth (Acuña et al. 1995). During this time, the spacecraft made many crossings of the terrestrial bow shock and spent significant time in both the ion and electron foreshock regions upstream of the shock. Over its lifetime

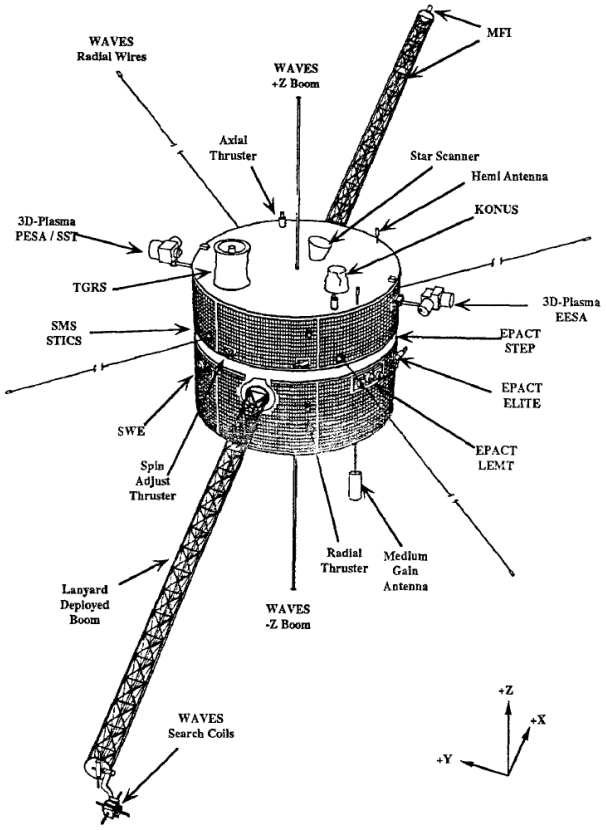

Figure 4.1: *Wind* spacecraft with locations of instruments. Figure from Harten & Clark (1995).

of more than 15 years, *Wind* has returned several times to the near Earth environment, making many additional bow shock crossings and even a deep crossing of the magnetotail. For the past several years, *Wind* has been in a stable 'halo' orbit around L1. Despite its relatively advanced age, the *Wind* spacecraft is in good health and continues to make excellent measurements.

The twin STEREO (Solar TErrestrial RElations Observatory) spacecraft were launched on October 25th, 2006, as the second mission in the NASA Solar Terrestrial Probes (STP) Program. The STP program has a focus that is similar to that of the ISTP program, in that it seeks to understand the fundamental physics underlying energy and momentum transfer in the Sun-Earth system. The STP program seeks to fill in the gaps left in our understanding of this system by sending probes to relatively unexplored areas and using coordinated measurements to explore previously unavailable physical scales.

The goal of the STEREO mission is to understand CME generation, evolution, and interaction with the Earth. The unique STEREO contribution to this goal is based on

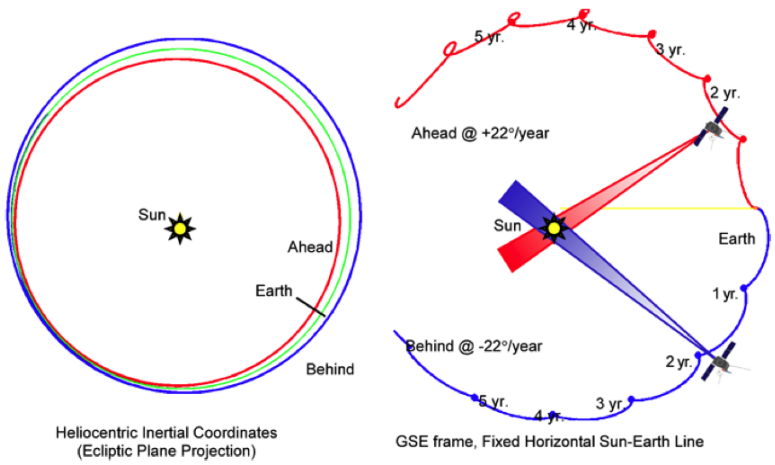

Figure 4.2: STEREO orbit. Figure is from Driesman et al. (2008).

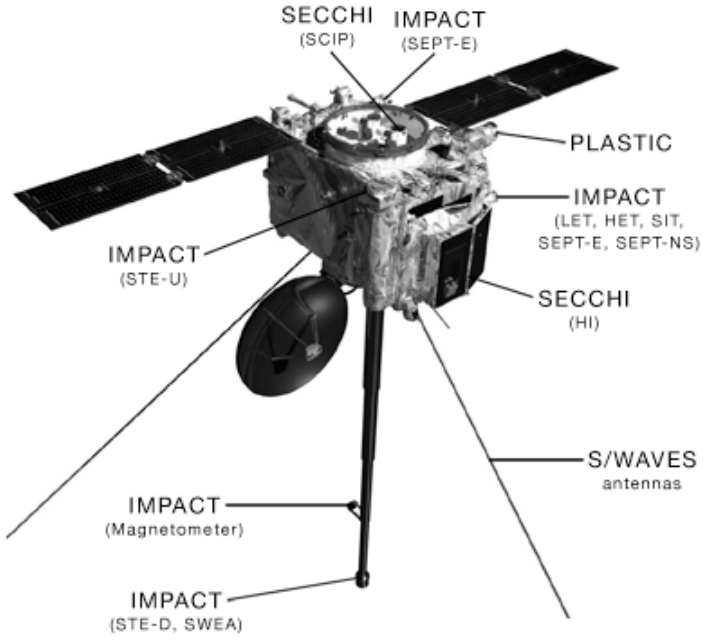

Figure 4.3: STEREO Behind spacecraft with locations of instruments shown. The STEREO-A spacecraft is nearly identical. Image source: STEREO website (http://stereo.gsfc.nasa.gov/)

the orbit of the two STEREO spacecraft. The two spacecraft were launched together, and entered a petal orbit. After this early stage, which included several bow shock encounters and significant time spent in the terrestrial foreshock, the spacecraft used lunar encounters to separate and enter two heliocentric orbits. The Ahead, or STEREO/A, spacecraft orbits at slightly less than 1 AU and therefore moves slightly faster than the Earth. The reverse is true for the Behind, or STEREO/B, spacecraft. The spacecraft drift ahead and behind the earth in its orbit at a rate of approximately 22.5 degrees per year (see Figure 4.2). The stereoscopic view available from these positions enables true three dimensional tracking of CMEs from their surface origins past 1 AU.

The STEREO spacecraft includes a suite of solar and heliospheric telescopes (Howard et al. 2008) designed to observe CMEs using fields of view from the chromosphere out to beyond the radius of the Earth. The attitude requirements for the telescopes require that STEREO be a three-axis stabilized spacecraft, unlike the spin-stabilized *Wind* spacecraft. This has ramifications for the design and performance of the field and particle instruments, as described in the following sections.

Although STEREO was launched in the longest and deepest solar minimum of the space age, limiting the number of large CMEs available for study, significant results have come from the STEREO mission, including the first optical observations of CIRs (Rouillard et al. 2008) and quadrature observations of waves in the low corona (Patsourakos & Vourlidas 2009). The spacecraft are in excellent position and health for observation of the rise phase of the next solar cycle.

4.2 Electric Field/Plasma Waves

The *Wind* and STEREO spacecraft both carry electric field instrumentation to measure remote radio wave emission and *in situ* electric fields. The primary difference between the two instruments derives from the fact that *Wind* is a spinning spacecraft, while STEREO is three-axis stabilized.

The *Wind*/WAVES sensors consist of two orthogonal wire dipoles in the spin plane of the spacecraft, and one rigid boom along the spin axis. The longer of the two spin plane dipoles is 100 m from tip to tip, and the shorter is 15 m from tip to tip. The spinning motion of the spacecraft enables it to hold the wire sensors in a stable position via centrifugal force. The rigid boom extends 12 m from tip to tip (Bougeret et al. 1995).

Because STEREO is three-axis stabilized, it is impossible to hold long wire antennas in place through the spacecraft motion, and hence the sensors must be rigid booms. The three STEREO/WAVES antennas are 6 m long monopoles mounted in an orthogonal configuration on the rear (anti-sunward) side of the STEREO spacecraft (see Figure 4.3). The length of the STEREO/WAVES sensors is comparable to the Debye length of the solar wind at 1 AU ($\lambda_D \sim 10$ m). Each STEREO/WAVES sensor consists of a 6 m (when deployed) beryllium-copper tubular spring known as a stacer (Bougeret et al.

2008; Bale et al. 2008).

The electronics for both WAVES experiments are very similar. In the spectral domain, several instruments are used to cover the bandwidth between several kHz and 16 MHz. A preamplifier for each antenna is located close to the antenna base.

The low frequency spectral instruments (on *Wind*, the Thermal Noise Receiver (TNR) covers a range of 4–256 kHz; on STEREO, the Low Frequency Receiver (LFR) covers a range of 2.5–160 kHz) employ a wavelet-like transform of sampled data and an Automatic Gain Control (AGC) circuit to adjust the receiver gain and thereby increase the dynamic range. TNR and LFR measure physical phenomena such as *in situ* ion acoustic and Langmuir waves, electron quasi-thermal noise, and the low frequency component of interplanetary radio bursts.

The high frequency spectral instruments (on *Wind*, the radio receivers RAD1 and RAD2 combine to cover the range 20 kHz–13.825 MHz; on STEREO, the High Frequency Receiver (HFR) covers the range 125 kHz–16.025 MHz) use a super-heterodyne receiver system, producing an intermediate frequency by mixing the measured signal and a programmable synthesized frequency. The range of the high frequency receivers covers Type II and III radio bursts from the from several radii above the surface of the Sun to 1 AU.

Both high and low frequency instruments are capable of making multichannel measurements from selected antennas, and can therefore calculate both auto correlations and cross correlations between antennas. These measurements are critical for direction finding of radio sources, especially for the 3-axis stabilized STEREO antennas (Cecconi & Zarka 2005).

In the time domain, *Wind*/WAVES and STEREO/WAVES both contain a Time Domain Sampler (TDS) instrument, which makes a time series measurement of antenna voltage at a cadence of over one hundred thousand samples per second. These instruments can measure waveforms of events such as Langmuir waves and ion acoustic waves.

Spacecraft/Instrument	*Wind*/WAVES	STEREO/WAVES
Configuration	50 m wire booms (×2)	6 m stacers (×3)
	7.5 m wire booms (×2)	
	12 m rigid boom	
LF spectral range	4–256 kHz (TNR)	2.5–160 kHz (LFR)
HF spectral range	20 kHz–13.825 MHz (RAD1/2)	125 kHz–16.025 MHz (HFR)
TDS max sample rate	120k samples/second	250k samples/second

Table 4.1: Properties of the *Wind* and STEREO electric field instruments.

4.3 Magnetic Field

The magnetic field measurements presented in this thesis come from triaxial fluxgate magnetometers mounted on booms on the *Wind* and STEREO spacecraft. A fluxgate magnetometer consists of a core of magnetic material around which two coils, the drive coil and the sensing coil, are wrapped. An alternating current in the first coil is used to continuously drive the magnetic core through its hysteresis loop, which induces a voltage in the sensing loop. The presence of external magnetic fields can make it easier or more difficult to drive the core to saturation in a given direction, depending on the strength and sign of the component of the external field aligned with the magnetic core. This effect is measured by observing the time varying voltage in the sensing coil. A thorough review of space-based magnetometers, including fluxgate magnetometers, can be found in Acuña (2002).

The *Wind* spacecraft deploys a dual magnetometer system mounted on a 12 m boom, with one magnetometer located near the end of the boom and the other approximately 2/3 of the distance along the boom. The dual magnetometer configuration allows allows a calibration which separates the magnetic field in the plasma from the magnetic field generated by the spacecraft (Lepping et al. 1995).

The STEREO spacecraft has a single magnetometer, carried on the IMPACT (In-situ Measurements of Particles and CME Transients) boom (Ullrich et al. 2008) approximately 3 m from the spacecraft. In order for the instrument to carry out uncontaminated measurements without the use of two magnetometers, a stringent magnetic cleanliness program was implemented during the design of the STEREO spacecraft (Acuña et al. 2008).

Spacecraft/Instrument	*Wind*/MFI	STEREO/MAG
Cadence	11 Hz	8 Hz
Range	±64 nT	±512 nT
Accuracy	±0.016 nT	±0.015 nT

Table 4.2: Properties of the *Wind* and STEREO fluxgate magnetometers. Parameters listed are for typical operating mode in the solar wind. Both magnetometers have operating modes which allow for measurement in high field environments such as the magnetosphere (Lepping et al. 1995; Acuña et al. 2008).

4.4 Electrostatic Detectors

The electrostatic electron detectors for both *Wind* and STEREO operate using similar principles. However, as in the case of the plasma wave instruments, the three axis stabilized STEREO spacecraft must accommodate the instrument differently. The Three-Dimensional Plasma (3DP) suite (Lin et al. 1995) on the *Wind* spacecraft contains two electron electrostatic analyzers, EESA-L and EESA-H, which measure electron energies from 3 eV to 30 keV. The STEREO/IMPACT suite includes the Solar Wind Electron Analyzer (SWEA) (Sauvaud et al. 2008), which has an energy range from 1 eV to 3 keV.

In both instruments, electrons enter the instrument via an aperture. Electrons of a specific energy range are then electrostatically deflected in a curved path between two hemispherical plates. Once the electrons have passed through the deflector plates, they are accelerated by a potential of several hundred volts before hitting a chevron multi channel plate (MCP) detector, which generates a signal which is measurable by the instrument electronics.

The EESA-L field of view is a narrow fan oriented radially to the spacecraft, which measures 180°×14°. The field of view rotates with the spacecraft, so EESA-L can measure a full 4π steradian electron distribution function with every spacecraft rotation. The SWEA instrument is located in a fixed position at the end of the IMPACT boom (see Figure 4.3). SWEA therefore implements an additional electrostatic deflection of the field of view (±60°) prior to the electrons entering the curved plate system. This results in a total SWEA field of view of 360°×120°, with unviewable regions parallel and antiparallel to the IMPACT boom direction. The field of view of each instrument is made up of many separate sectors to provide angular resolution of for 5.6–22.5° for EESA-L and 22.5° for SWEA.

Spacecraft/Instrument	*Wind*/EESA-L	STEREO/SWEA
Cadence	3 s burst, 45 s survey	2 s burst, 45 s survey
Energy Range	3 eV to 30 keV	1 eV to 3 keV
Field of View	180°×14°	360°×120°
Geometrical Factor	1.3×10^{-2} (cm^2 sr eV)/eV	8.4×10^{-3} (cm^2 sr eV)/eV

Table 4.3: Properties of the *Wind* and STEREO electrostatic electron detectors. Field of view does not take rotation into account.

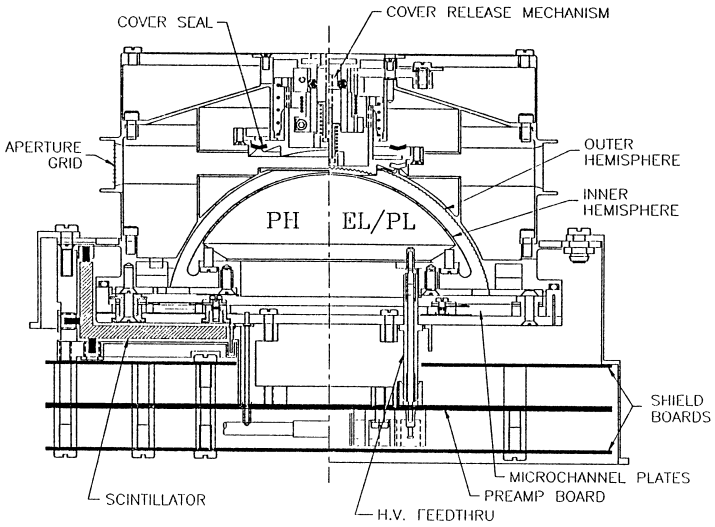

Fig. 4. Cross section of an electrostatic analyzer representative of PESA-H (*left side*), and PESA-L and EESA-L (*right side*).

Figure 4.4: Diagram illustrating design of the *Wind*/3DP electrostatic detectors, including EESA-L (on the right side). Figure from Lin et al. (1995).

4.5 Suprathermal Electrons

In addition to the electrostatic detectors, the STEREO/IMPACT suite includes a Supra-Thermal Electron (STE) solid state electron instrument which measures electrons in the range 2–100 keV. On each STEREO spacecraft, the STE instrument includes two detectors, one upstream sunward detector, STE-U, with a field of view along the nominal Parker spiral and one antisunward detector, STE-D, with a field of view in the opposite direction. Each detector in turn consists of four pixels, each of which is a silicon semiconductor detector (SSD). The four pixels are arranged in a strip, and the field of view for each pixel is defined by a single rectangular aperture mounted above the strip of pixels. Each STE detector therefore has four fixed look directions, centered on the Parker spiral angle in the upstream and downstream direction (see Figure 4.6). The STE energy range, 2–100 keV is partially covered on *Wind* by the electrostatic EESA-H detector, which has an energy range of 100 eV–30 keV. Compared to EESA-H, STE has a much larger geometric factor, and a much larger duty cycle for any given energy channel due to the fact that the electrostatic analyzer must measure one energy at a time (Lin et al. 2008). The upstream STE detectors are saturated by multiple scattering of sunlight off the spacecraft and instrument into the sensors.

While the STE detector is more sensitive by orders of magnitude to suprathermal electrons, it is also sensitive to ions and neutral particles, since STE has no charged

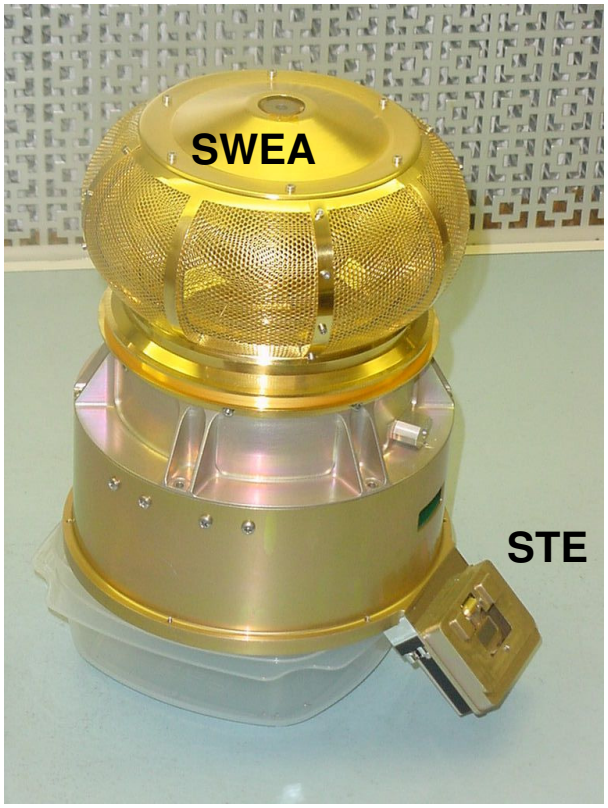

Figure 4.5: The STEREO SWEA and STE-D detectors. The combined SWEA/STE package caps the STEREO/IMPACT boom. Image source: STEREO/IMPACT website (http://sprg.ssl.berkeley.edu/impact/).

deflection plates, as does an electrostatic detector, and X-rays, since STE has no foil or other barrier to the SSDs. Therefore, it may be difficult to determine which type of incident particle or photon has triggered a STE event. For example, the annual modulation of STE-D quiet time spectra has been interpreted as energetic neutral atoms (ENAs) from the heliosheath (Wang et al. 2008) and as X-rays from the strong X-ray source Sco X-1 (Hsieh et al. 2009). However, these events occur on a much longer time scale than the bursty foreshock beams which are analyzed in Chapter 7.

STE often observes ion and electron beams in the terrestrial foreshock, and the detectors do not discriminate between particle types. Several additional indicators can distinguish the two types of beam: a) the electron beams are often seen in both STE and SWEA, b) the electron beams are sometimes accompanied by Langmuir wave emission, and c) the beams often present energy distributions which would be highly unstable to Landau resonance, and therefore cannot be electron beams and must be ion beams. Using these criteria, we can reliably distinguish electron beams from ion beams in the

terrestrial foreshock.

Spacecraft/Instrument	STEREO/STE
Energy Range	2–100 keV
Field of view	80°×80°
Geometrical Factor	0.10 cm^2 sr

Table 4.4: Properties of the STEREO STE detector. The field of view is the combined field for all four detectors, and is centered 225° from the Sun.

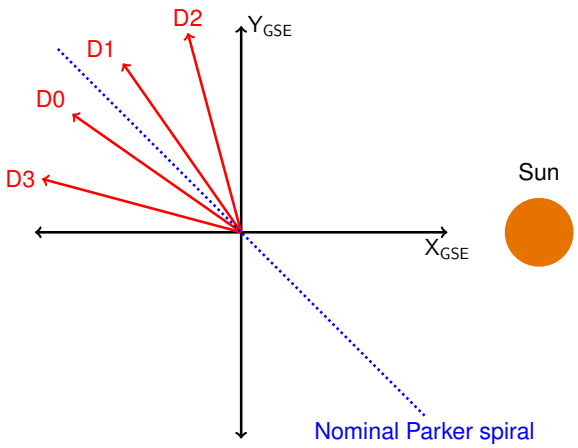

Figure 4.6: STE-D look directions

Chapter 5

Interplanetary Foreshock Regions

Pulupa, M., & Bale, S. D. 2008, ApJ, 676, 1330

We present *in situ* observations of the source regions of interplanetary (IP) type II radio bursts, using data from the Wind spacecraft during the period 1996-2002. We show the results of this survey as well as in-depth analysis of several individual events. Each event analyzed in detail is associated with an interplanetary coronal mass ejection (ICME) and an IP shock driven by the ICME. Immediately prior to the arrival of each shock, electron beams along the interplanetary magnetic field (IMF) and associated Langmuir waves are detected, implying magnetic connection to a quasiperpendicular shock front acceleration site. These observations are analogous to those made in the terrestrial foreshock region, indicating that a similar foreshock region exists on IP shock fronts. The analogy suggests that the electron acceleration process is a fast Fermi process, and this suggestion is borne out by loss cone features in the electron distribution functions. The presence of a foreshock region requires nonplanar structure on the shock front. Using Wind burst mode data, the foreshock electrons are analyzed to estimate the dimensions of the curved region. We present the first measurement of the lateral, shock-parallel scale size of IP foreshock regions. The presence of these regions on IP shock fronts can explain the fine structure often seen in the spectra of type II bursts.

5.1 Introduction

Interplanetary type II radio bursts are generated upstream of IP shocks by solar wind electrons reflecting from the shock front. The reflected electron beams create Langmuir waves which produce type II emission at the local electron plasma frequency f_p, and possibly the second harmonic. The upstream region in which the radio emission is generated is analogous to the electron foreshock region at the Earth's bow shock. The *in*

situ terrestrial foreshock has been extensively studied by many spacecraft. In contrast, only one *in situ* IP foreshock region has been described in the literature (Bale et al. 1999). In this section, we will review the basic characteristics of electron acceleration and Langmuir wave generation at the terrestrial foreshock, and outline our analogous measurements upstream of IP shocks.

Terrestrial foreshock electron beams were first observed in the upstream regions of the Earth's bow shock by the ISEE spacecraft. (Anderson et al. 1979; Fitzenreiter et al. 1984) At the terrestrial foreshock, solar wind electrons and ions are accelerated by a fast Fermi process. The bow shock, moving in the solar wind frame, mirrors the particles and accelerates them tangent to the shock along IMF lines (Wu 1984; Leroy & Mangeney 1984). The backstreaming electrons then cause bump-on-tail velocity distributions and generate upstream Langmuir waves (Filbert & Kellogg 1979). If the acceleration point is magnetically connected to a spacecraft, the spacecraft observes an energetic electron beam aligned with the IMF. The region in which these beams are present is known as the electron foreshock region. The Wind spacecraft has made detailed observations of electron beams, bump-on-tail distributions, and signatures of fast Fermi acceleration in the terrestrial foreshock (Fitzenreiter et al. 1996; Larson et al. 1996).

The efficiency of fast Fermi acceleration at curved shocks peaks when the IMF lines are nearly tangent to the shock (Krauss-Varban et al. 1989; Krauss-Varban & Burgess 1991). This places constraints on the geometry of the shock front, as a straight upstream IMF line has no tangent point to a shock unless curvature is present on the shock front. Therefore, evidence of a foreshock region is also evidence of curved structure. Cairns (1986) proposed a time-of-flight mechanism for Type II emission generated by a curved IP shock analogous to the Filbert & Kellogg (1979) mechanism for emission generated by the curved terrestrial bow shock.

Reiner et al. (1998a) has suggested that the intermittent nature of type II emissions implies multiple, distinct emission regions. It has also been shown with both remote sensing (Reiner et al. 1998b,a) and *in situ* observations (Bale et al. 1999) that the source region of type II emission lies upstream of CME-driven shock fronts. Taken together, these observations suggest that type II emission is generated in multiple foreshock regions upstream of IP shocks. Theoretical models of electron reflection from the surface of interplanetary shocks are consistent with this model, producing electron beams and plasma radiation at f_p and $2f_p$ which agree reasonably well with the observed quantities (Knock et al. 2003, 2001; Cairns et al. 2003).

We will use both 'IP foreshock region' and 'type II source region' interchangeably throughout this paper, our choice of terminology depending on whether the emphasis of the discussion is on the accelerated electrons or the radio emission. Both terms refer to the same physical region.

The event described by Bale et al. (1999) was the first observed *in situ* measurement of a type II radio burst. We have examined the data set of IP shocks observed by the Wind spacecraft, searching for additional events. Section 5.2 describes the results of the

search.

Section 5.3 presents detailed *in situ* observations of three selected IP foreshock regions, showing the correlation between upstream electron beams and the local generation of type II radiation.

Sections 5.4 and 5.5 emphasize the information about shock structure that may be deduced from the velocity-dispersed foreshock electron beams. By analyzing velocity-dispersed electron beams in the foreshock region, we can determine the shock-parallel and perpendicular scale size of the shock front structure. The calculated parameters are illustrated in Figure 5.1. In order to calculate the perpendicular scale height $d_\perp$ of the shock structure, we must determine both the shock speed V_{sh} and the initial acceleration time of the foreshock electrons t_0. To calculate the lateral distance $d_\parallel$ from the spacecraft to the acceleration point, we analyze the velocity dispersion of the foreshock electron beam. Since the spacecraft can be connected to the shock front in both the IMF-parallel and antiparallel direction, we can potentially determine $d_{-\perp}$ and $d_{-\parallel}$ as well. Taken together, these measurements describe the nature of the rippling which occurs along the shock front. We present all distances in units of R_E as well as km, to facilitate comparison with the terrestrial foreshock region. The shock surface shown in Figure 5.1 is approximately to scale with the $d_{\pm\perp}$ and $d_{\pm\parallel}$ parameters determined for the 28 August 1998 shock.

Section 5.6 examines the validity of the assumptions we use in analyzing the IP shocks, and Section 5.7 summarizes our observations and discusses possible origins of the IP foreshock regions.

5.2 Event Selection

We have investigated *in situ* data from the Wind spacecraft for several hundred shocks which occurred during the time period 1996-2002. Our list of shocks was obtained from the MIT database of Wind shock crossings.[1] We used data from the Wind/WAVES plasma wave experiment (Bougeret et al. 1995) to investigate each shock. Of the 377 shock crossings in the database, we found 125 events which upon visual inspection contained possible foreshock Langmuir wave activity (LWA), as evinced by strong plasma frequency radiation immediately prior to shock arrival. We inspected these events closely for signs of *in situ* type II radiation.

We eliminated events with rapid changes in plasma density and magnetic field prior to shock arrival, in order to avoid misidentification of upstream waves as foreshock structures. We also eliminated events with other possible sources of plasma frequency emission, such as Langmuir waves caused by reflection from the terrestrial foreshock, or type III radio bursts arriving at Earth.

[1] http://www.cfa.harvard.edu/shocks/

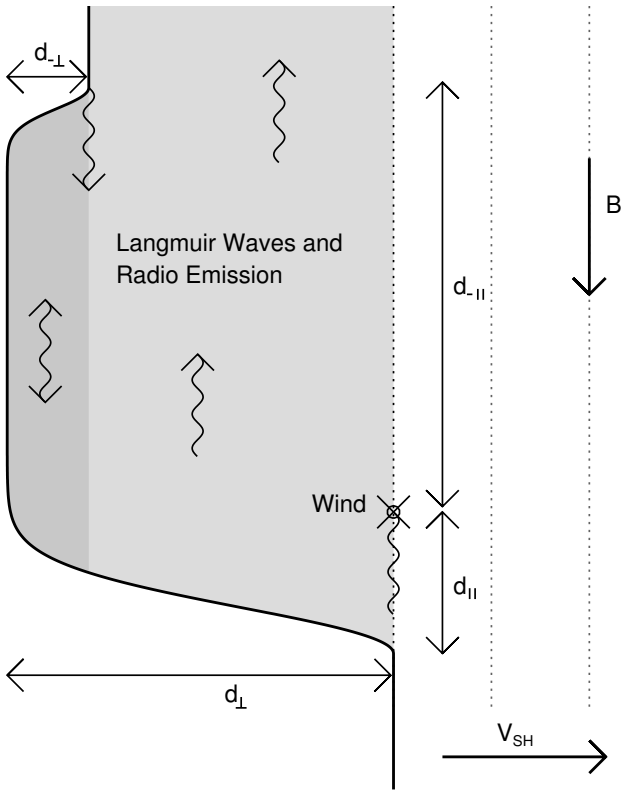

Figure 5.1: A cartoon of shock structure consistent with our observations. Electron flux in the $\mathbf{B}$ and $-\mathbf{B}$ direction increases previous to shock arrival, as Wind is connected along the IMF line to an advanced section of the shock front. Langmuir waves and electron beams are observed in the foreshock region.

Using data from the Three-Dimensional Plasma (3DP) instrument suite on Wind (Lin et al. 1995), we searched for correlations between IMF-parallel electron beams and LWA. The electron beams were measured by the low energy electron electrostatic analyzer (EESA-L), an instrument on the 3DP suite. The EESA-L instrument measures one full 3D electron distribution function per spacecraft spin (3 seconds). However, the cadence of data in the telemetry stream is determined by the telemetry rate of the spacecraft. In normal operation, the spacecraft returns distribution functions at a rate of approximately one per 100 seconds. An instrument 'burst-mode' provides full time resolution (3 second) measurements when a burst-mode trigger criterion is met. The trigger is computed on board from a selectable set of measurements (e.g. ion or electron flux changes). Some programmed burst triggers are optimized to catch shocks, while others might be optimized

to investigate energetic particle events. When an event is detected by the burst mode trigger, the spacecraft stores higher cadence data into a circular buffer, and sends the data when the event ends or when the memory is full.

In many cases, the LWA occurred in short bursts lasting less than 1 minute, and therefore did not appear in the Wind low cadence data. Wind was operating in burst mode for less than half of the shocks with possible Langmuir wave activity. On one occasion, the LWA was sustained for minutes prior to the shock, and could therefore be correlated with the low cadence electron data. The majority of the 125 events with possible *in situ* type II radiation were eliminated from consideration because the lack of burst mode data made the association between the plasma emission and IMF-parallel electron beams impossible to confirm.

In order to determine the source of the IP shocks, we used the lists of CME events and related shocks published in Cane & Richardson (2003) and Manoharan et al. (2004), as well as the type II radio burst list maintained at Goddard Space Flight Center.[2]

We found a total of 8 events (including the event published in Bale et al. (1999)) possessing all of the characteristics described above: upstream LWA, observed IMF-parallel electron beams correlated with the LWA, a relatively stable upstream plasma environment during the periods of LWA, and an identifiable ICME source for the shock. These events are listed in Table 5.1.

Of the 8 events, three contained velocity-dispersed electron beams. As will be shown in the following sections, this feature enables the measurement of the lateral scale size of the shock front structures where type II radiation is generated. The measurement of this lateral scale size is the primary new measurement presented in this paper, therefore we will focus on the three events with velocity-dispersed beams.

5.3 Foreshock Electron Observations

The three *in situ* type II events with observed velocity dispersed electron beams occurred upstream of IP shocks which arrived at the Wind spacecraft on 15 May 1997, 26 August 1998, and 11 February 2000. The 26 August 1998 event has been described in Bale et al. (1999). The shock for that event was driven by an ICME associated with an X1.0 class flare which occurred at 22:09 UT on 24 August 1998.

The 15 May 1997 (11 February 2000) shock was driven by an ICME associated with a C1.3 (C7.3) class flare which occurred at 04:55 UT on 12 May 1997 (02:08 UT on 10 February 2000.)

Figure 5.2 shows dynamic spectra from Wind/WAVES and magnetic field data from the MFI instrument (Lepping et al. 1995) on Wind, along with GOES X-ray data for each of these three events. Upstream and downstream plasma parameters for each shock

[2]http://lep694.gsfc.nasa.gov/waves/waves.html

are listed in Table 5.2. At each event, the Wind spacecraft was in the foreshock region for a timespan of 20 to 40 seconds.

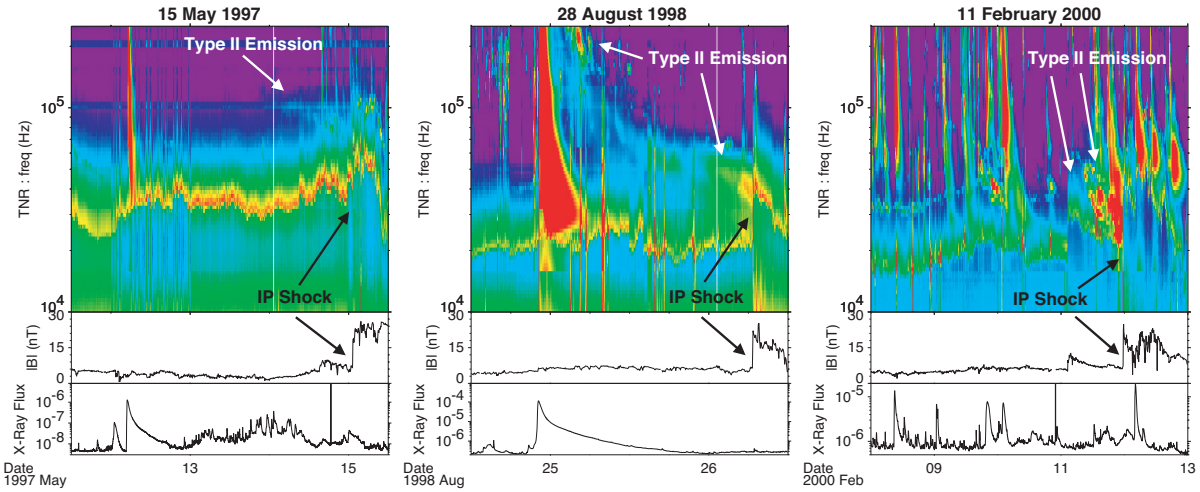

Figure 5.2: Radio wave, magnetic field, and GOES x-ray data for three shock crossings seen by the Wind spacecraft. The top panel is a dynamic spectrum from the WAVES instrument on Wind, the bottom panel is the x-ray flux data in the band $1 - 8$Å from the GOES-8 satellite (for May 1997) and the GOES-10 satellite (for August 1998 and February 2000.) The flare activity is shown by the x-ray peaks and type III radio bursts on 12 May 1997, 24 August 1998, and 9 February 2000. The type II emissions can be seen as slowly drifting features in the spectrum, and the spacecraft shock crossings are indicated by abrupt jumps in the local plasma frequency and the magnetic field.

Figure 5.3 shows two-dimensional electron pitch angle distributions from the EESA-L instrument on Wind/3DP. The distributions are shown for each event in the upstream 'pre-foreshock' region, in the foreshock region, and in the downstream region after the shock has passed. The foreshock region is distinguished by the electron beams in the IMF-parallel direction, which can be seen as the bulges in the parallel and anti-parallel direction on the two-dimensional distributions and in the parallel (solid line) and perpendicular (dashed line) cuts. The observed electron distribution functions are consistent with the predictions of electron beams originating from the shock as predicted by Filbert & Kellogg (1979), and reflected by the Fast Fermi process described by Wu (1984) and Leroy & Mangeney (1984). The distribution functions also show an angular feature corresponding to a loss cone. This loss cone feature is predicted by the Fast Fermi theory and has been observed by Wind/3DP in the terrestrial foreshock (Larson et al. 1996).

The electron beam reflected from the surface of the shock creates a bump on the tail of the electron distribution function. Due to velocity selection effects, this bump is most prominent at the boundary of the foreshock region (Fitzenreiter et al. 1984).

LASCO CME			IP Shock			Burst	Velocity	Type II
Year	Date	Time	Year	Date	Time	Data	Dispersion	Emission*
1997	May 12	0530	1997	May 15	0115	X	X	X
1998	Aug 24	2209	1998	Aug 26	0640	X	X	X
2000	Feb 10	0230	2000	Feb 11	2333	X	X	X
2000	Feb 17	0431	2000	Feb 20	2045	X		X
2000	Oct 02	0350	2000	Oct 05	0240	X		
2000	Oct 09	2350	2000	Oct 12	2145	X		
2001	Mar 19	0526	2001	Mar 22	1355			
2001	Dec 26	0530	2001	Dec 30	2005	X		X

Table 5.1: IP Shocks With Observed *in situ* Type II Source Regions. *Denotes presence in the Wind/WAVES type II database. *In situ* plasma frequency (type II) radiation was observed in the foreshock region of each event.

The Wind Solar Wind Experiment (SWE) (Ogilvie et al. 1995) has observed the positive slope at many encounters with the terrestrial foreshock boundary (Fitzenreiter et al. 1996). However, the Wind/3DP instrument has insufficient energy resolution to resolve the positively sloped region on the tail of the distribution function, and therefore does not observe the bump during the same encounters.

After the arrival of the shock, the distributions display the broadened, flat-topped characteristics common to distributions downstream of strong interplanetary shocks (Fitzenreiter et al. 2003).

The association of the foreshock electrons with the type II emission is established using the Langmuir wave observations from the WAVES instrument. Figure 5.4 shows wave and particle data from Wind at each shock crossing. Panel (a) is a WAVES dynamic spectrum showing intense Langmuir wave activity in each foreshock region. Panels (b) and (c) show magnetic field magnitude from MFI and proton density from 3DP. In both panels, there is a clear discontinuity as each shock crosses the spacecraft. The bottom three panels show electron energy flux for a range of energies measured by the low geometric factor Electron Electrostatic Analyzer (EESA-L) on 3DP. The Wind spacecraft was in burst mode during each shock crossing, measuring full three dimensional electron distributions once every three seconds. Panels (d), (e), and (f) show the IMF-parallel, antiparallel, and perpendicular fluxes, respectively. The Langmuir waves in panel (a) are associated with increases in electron flux in both the parallel and antiparallel directions, except for the 11 February 2000 shock, for which only antiparallel foreshock flux was observed. The black

bars on the plots indicate the locations of elevated flux due to foreshock electrons. The correlation between foreshock electrons and Langmuir wave activity strongly indicates that these regions are sources of type II radio emission. In the following sections, we will use the electron burst data to characterize the shock-perpendicular scale height and shock-parallel scale distance of the foreshock region.

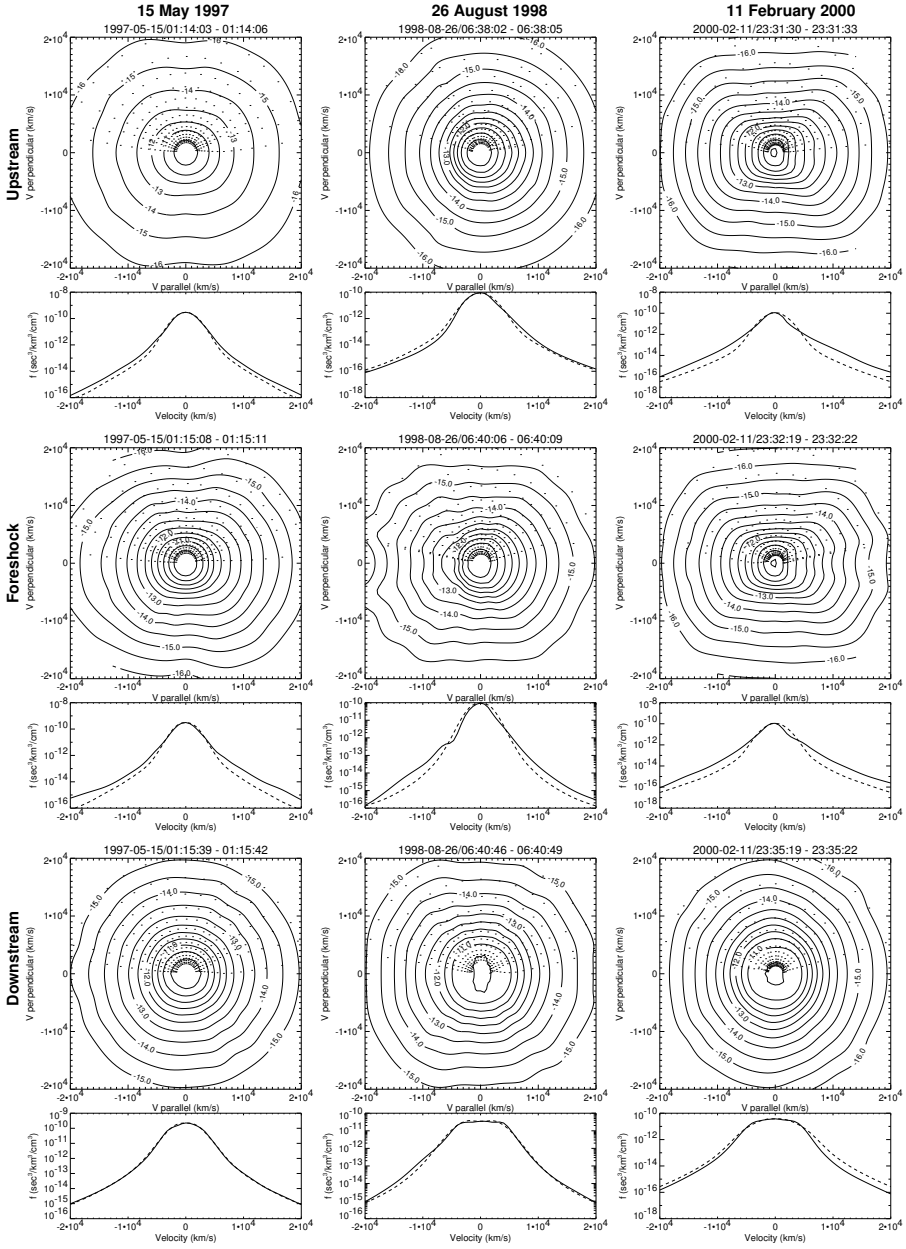

Figure 5.3: Electron velocity distributions measured by the EESA-L instrument on Wind during the upstream pre-foreshock, foreshock, and downstream periods for the three IP shocks. The foreshock region is characterized by bumps on the parallel distribution function and the loss cone evident in the 26 August 1998 and 11 February 2000 foreshock regions. The bottom part of each panel shows a parallel (solid line) and perpendicular (dashed line) cut through each two-dimensional distribution.

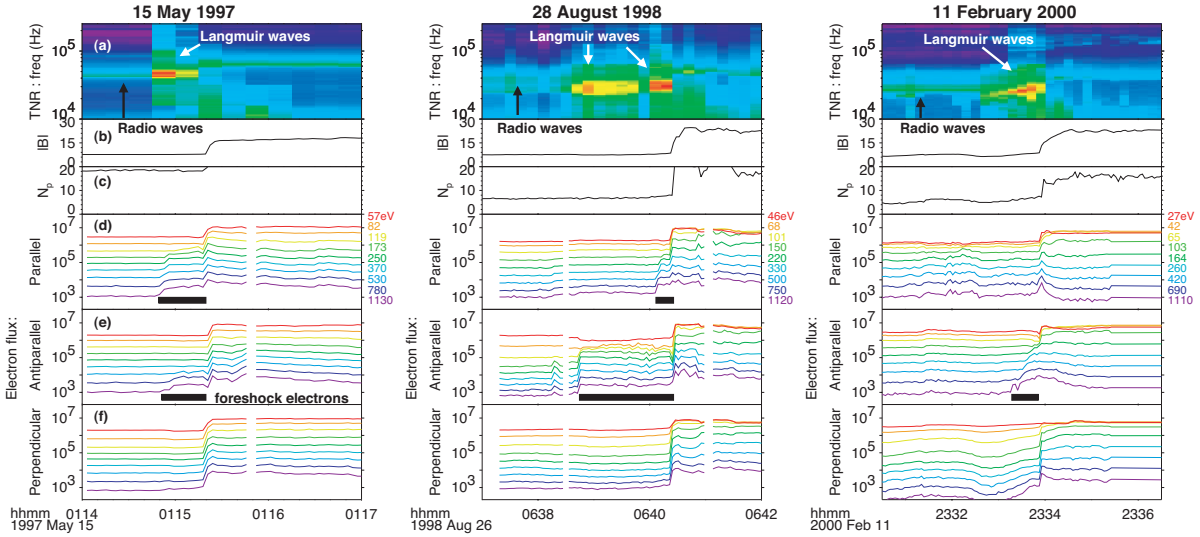

Figure 5.4: *In situ* particle and wave data from the Wind spacecraft for the three shock crossings. Panel (a) is a dynamic spectrum from the WAVES Thermal Noise Receiver, showing Langmuir wave activity in the foreshock region. Panels (b) and (c) are magnetic field and density measurements from MFI and 3DP, both showing a jump at the arrival of the shock. Panels (d), (e), and (f) are electron flux energy distributions from the EESA-L experiment on 3DP, in the parallel, antiparallel, and perpendicular directions. The foreshock electron beams are denoted by black bars in the parallel and antiparallel panels. The units for magnetic field are nT, for density $1/\mathrm{cm}^3$, and electron flux $1/\mathrm{eV}/\mathrm{sec}/\mathrm{cm}^2/\mathrm{ster}$.

5.4 Shock-Perpendicular Scale Height

The scale height $d_\perp$ of the feature on the shock front is determined by the speed of the shock in the spacecraft frame $V_{sh}^{S/C}$ and the amount of time Δt between the start of foreshock electron enhancement and arrival of the shock.

$$d_\perp \approx V_{sh}^{S/C} \cdot \Delta t \tag{5.1}$$

The time interval, indicated by the black bars in Figure 5.4, is easily measured. The shock velocity in the spacecraft frame is determined by mass flux conservation across the shock boundary (Paschmann & Schwartz 2000), and is given by:

$$V_{sh}^{S/C} = \frac{\Delta(\rho \mathbf{V}^{S/C})}{\Delta\rho} \cdot \hat{\mathbf{n}} \tag{5.2}$$

where ρ is the local mass density and $\hat{\mathbf{n}}$ is the unit vector normal to the shock surface. The determination of $\hat{\mathbf{n}}$ is discussed in a later section.

The scale height of the 26 August 1998 shock was calculated in Bale et al. (1999) and found to be $136,000$ km ($21.3\ R_E$) for $d_{-\perp}$, the height of the structure in the antiparallel direction, and $25,000$ km ($3.9\ R_E$) for $d_\perp$, in the parallel direction. Our method yields the significantly smaller values of $69,000$ km ($10.1\ R_E$) for $d_{-\perp}$ and $15,000$ km ($3.9\ R_E$) for $d_\perp$. These results differ because Bale et al. (1999) uses the total time between the start of the flare and arrival of the shock to calculate an average shock speed from the inner heliosphere to 1 AU. Here we use the *in situ* method described above, which yields an instantaneous V_{sh} that more accurately describes the local shock parameters.

The calculated values of $d_\perp$ and $d_{-\perp}$ for each of the three analyzed shocks are listed in Table 5.3.

5.5 Estimating Shock-Parallel Distance

When electrons reflect from the shock surface and stream along IMF lines to the spacecraft, the most energetic accelerated electrons will arrive first, followed by the lower energy electrons. Provided that the distance from the acceleration point is sufficiently large and the energy and time resolution of the detector is sufficiently good, this time of flight dispersion is observable in the foreshock electron beam.

The velocity of the electrons is determined by the (nonrelativistic) formula

$$v_e = \sqrt{2E/m_e} \tag{5.3}$$

where E is the kinetic energy of the electron.

We assume that the electrons were accelerated instantaneously at a time t_0. The transit time for each energy bin is determined by the time interval between t_0 and t_{onset},

Date	Time	B_1/B_0	$V_{sh}^{S/C}$ (km/s)	U_{sw} (km/s)	M_A	β	r_L (km)	θ_{bn}
15 May 1997	0115	2.19	423.	321.	2.62	0.44	392.	89.9
26 August 1998	0640	3.09	659.	493.	2.63	0.66	665.	88.1
11 February 2000	2333	3.24	678.	458.	3.19	0.39	654.	85.7

Table 5.2: Shock and Plasma Parameters for Selected Events.

Date	t_0	t_{shock}	$d_\perp$		$d_\parallel$		$d_{-\perp}$		$d_{-\parallel}$	
15 May 1997	01:14:43	01:15:23	17	(2.6)	136	(21.2)	17	(2.6)	≤ 140	(21.9)
26 August 1998	06:40:04	06:40:27	15	(2.3)	78	(12.2)	69	(10.1)	≤ 26	(4.0)
11 February 2000	23:32:55	23:33:58	...	...	...	...	28	(4.3)	151	(32.6)

Table 5.3: Shock Structure Parameters (d measured in Mm (R_E))

when the first enhancement appeared in that bin. The parallel distance $d_{\parallel}$ and the initial acceleration time t_0 are determined by fitting the measured values of v_e and $t_{\rm onset}$ to the simple functional form

$$d_{\parallel} = v_e(t_{\rm onset} - t_0) = v_e \cdot \Delta t \tag{5.4}$$

The results of this fit are shown in Figure 5.5, which contains *in situ* data from the Wind/3DP in the foreshock region, for each of the three analyzed shocks. For each shock, only one of two possible directions contained sufficient velocity dispersion in the electron beam that the above equation could be fit. For the 15 May 1997 and 28 August 1998 shock, the parallel direction was fit. For the 11 February 2000 shock, the antiparallel direction was fit.

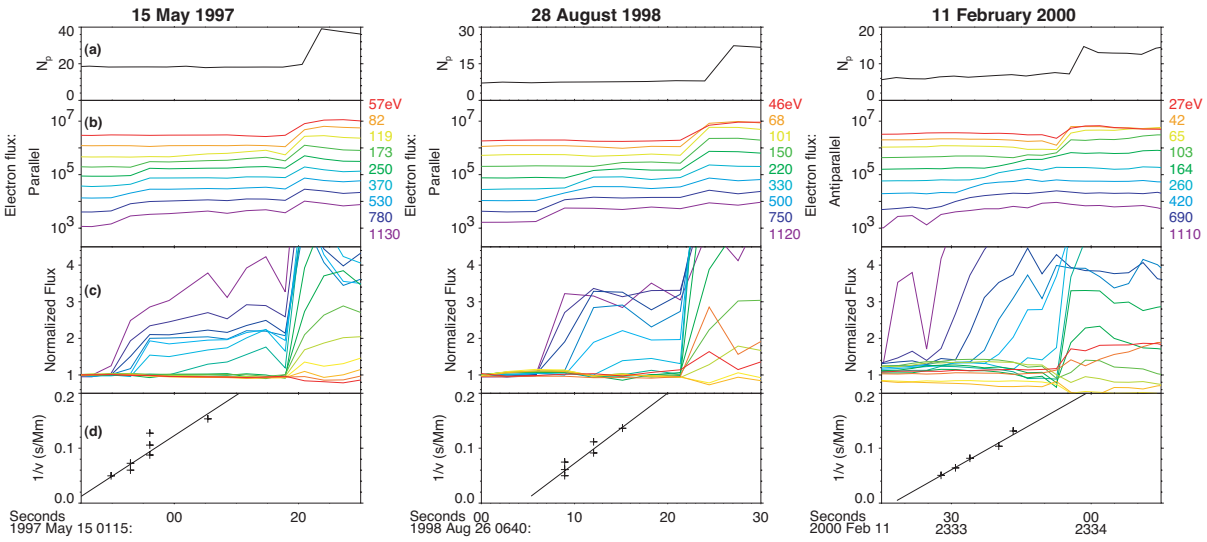

Figure 5.5: *In situ* particle data from the Wind 3DP instrument. Panel (a) is the particle density, showing the shock arrival time. Panel (b) is the parallel (antiparallel for 11 February 2000) electron energy distribution, showing the velocity dispersed electron beam. Panel (c) emphasizes the velocity dispersion by normalizing each energy channel to its pre-foreshock flux. Panel (d) shows a fit of arrival time to inverse electron velocity, as described in Equation 5.4.

The proton density is plotted in panel (a). The jump in density indicates arrival of the shock. Panel (b) shows the flux of electrons parallel (or antiparallel for 11 February 2000) to **B** prior to shock arrival. Note that flux enhancement occurs first in the high energy electron bins. Panel (c) shows the same electron flux, with each energy bin normalized to its preshock level. The onset time for each energy bin is defined as the time when the normalized flux first rises past a threshold value. Panel (d) shows a fit of onset time

against inverse velocity for each energy bin which showed foreshock enhancement. t_{acc} and $d_{\parallel}$ are given by fitting the velocity and time data to Equation 5.4.

It is important to clarify the relationship between Equation 5.4 and the 'foreshock coordinate system' established by Filbert & Kellogg (1979). Filbert & Kellogg (1979) noted that velocity-dispersed electrons will be a steady-state spatial feature of an electron foreshock in the shock frame. A 'cutoff' velocity v_c exists below which the shock-accelerated electrons will not reach the spacecraft; the result is a beam-like feature that is unstable to Langmuir waves. Filbert & Kellogg (1979) showed that $v_c \approx v_{sw} d_{\parallel}/DIFF$, where $DIFF$ is the distance downstream from the first tangent field line to the shock, in the direction of the solar wind flow. In our formulation, $DIFF = v_{sh}\Delta t \approx v_{sw}\Delta t$ so that $d_{\parallel} = v_c \Delta t$, which is equivalent to Equation 5.4. Hence this is just a transformation from the shock frame to the spacecraft frame.

For the 26 August 1998 shock discussed in Bale et al. (1999), the fit value for the shock parallel distance $d_{\parallel}$ is 78,000 km (12.2 R_E). The parallel beam for the 15 May 1997 shock and the antiparallel beam for the 11 February 2000 shock were also fit using this method, yielding $d_{\parallel} = 136,000$ km (21.2 R_E) for the 15 May 1997 shock and $d_{-\parallel} = 151,000$ km (32.6 R_E) for the 11 February 2000 shock.

The antiparallel foreshock beams seen in the 15 May 1997 and 26 August 1998 shocks do not display velocity dispersed onset times, implying that the acceleration site was close to the spacecraft. An upper limit on $d_{-\parallel}$ may be obtained by noting that if the fastest and slowest foreshock electrons arrived at the spacecraft at the same time to within the time resolution of 3DP burst mode, then $d_{-\parallel}$ must satisfy

$$d_{-\parallel}/v_{slow} - d_{-\parallel}/v_{fast} \leq 3 \text{ seconds} \tag{5.5}$$

which yields an upper limit for $d_{-\parallel} \leq 140,000$ km (21.9 R_E) for 15 May 1997 and $d_{-\parallel} \leq 26,000$ km (4.0 R_E) for 28 August 1998.

The calculated values of $d_{\parallel}$ and $d_{-\parallel}$ for all of the analyzed shocks are listed in Table 5.3.

5.6 Upstream IMF and coplanarity of shock front

In our calculation of $d_{\parallel}$ and $d_{\perp}$, we have made two assumptions about the magnetic field: that the IMF line connecting the shock to the spacecraft is straight, and that the shock propagation direction is perpendicular to the IMF lines. In this section, we investigate the validity of these assumptions.

The boundary of the electron foreshock region is determined by the IMF line tangent to the shock surface. Turbulence in the solar wind and electromagnetic radiation generated by shock-accelerated particles can deform the structure of the IMF. Numerical models of magnetic field line transport have been developed to simulate IMF conditions at planetary bow shocks (Zimbardo & Veltri 1996).

For IMF conditions similar to those at 1 AU, the ratio of the spread in the foreshock boundary Δr to the length of the connecting IMF line r is $\Delta r/r \approx 0.1$. If $\Delta r/r > d_\perp/d_\parallel$, then the foreshock measurements could be explained simply as an effect of turbulence in the IMF. However, for each analyzed shock, $d_\perp/d_\parallel$ (and $d_{-\perp}/d_{-\parallel}$) is greater than 0.1, so magnetic turbulence alone cannot account for the apparent structure on the shock front.

If the IMF lines are straight, but the shock front is not coplanar with the IMF lines, then the time of flight dispersion analysis can yield misleading results for the perpendicular distance to the shock. The above analysis assumes a coplanar structure, so we must establish that this is a good approximation.

The orientation of the shock to the IMF can be determined by mixed mode (including both field and particle data) coplanarity analysis. The coplanarity theorem for compressive shocks states that the shock normal ($\hat{\mathbf{n}}$), the upstream and downstream magnetic fields ($\mathbf{B}_u$ and $\mathbf{B}_d$), and the velocity jump across the shock ($\Delta\mathbf{V}$) all lie in the same plane. If $\Delta\mathbf{B} \equiv \mathbf{B}_d - \mathbf{B}_u$ is the change in magnetic field, then the shock normal (Paschmann & Schwartz 2000) is given by:

$$\hat{\mathbf{n}} = \frac{(\Delta\mathbf{B} \times \Delta\mathbf{V}) \times \Delta\mathbf{B}}{|(\Delta\mathbf{B} \times \Delta\mathbf{V}) \times \Delta\mathbf{B}|} \tag{5.6}$$

The perpendicularity of the shock is measured by θ_{bn}, the angle between the upstream magnetic field $\mathbf{B}_u$ and $\hat{\mathbf{n}}$. To check consistency, we also calculate θ_{bn} using $\mathbf{B}_u$ and $\mathbf{B}_d$ in place of $\Delta\mathbf{B}$ in Equation 5.6 (Paschmann & Schwartz 2000). Values for θ_{bn} for each shock are listed in Table 5.2.

For each mixed mode calculation at each shock, $\theta_{bn} > 80°$, so the assumption of a locally perpendicular shock front at Wind is a good one, and the angle between the shock front and magnetic field does not introduce large errors in our calculation of $d_\parallel$ or $d_\perp$.

5.7 Discussion

We have conducted a survey of several hundred IP shocks, and found *in situ* type II radiation, correlated with IMF-parallel electron beams, present at eight IP shocks. Most IP shocks do not show evidence of *in situ* type II radiation, and of those that do, few show evidence of upstream electron beams observable by the Wind spacecraft. However, this does not disprove the IP foreshock mechanism as the generator of type II radiation. The proposed mechanism is a localized phenomenon, while the consequent radiation is visible throughout the heliosphere. It is quite unlikely that any given region of localized emission will be encountered by the Wind spacecraft. The exact probability of such an encounter depends on the size and number of IP foreshock regions, and this paper represents a first attempt at quantifying both. Of the events which do present observed *in situ* type II radiation, the low number of events with correlated waves and electron

beams is primarily due to the infrequent availability of high cadence measurements of the electron distributions.

In addition to the survey of the Wind data set, we present detailed *in situ* observations of the electron foreshock region of three IP shocks. In each of these three events, the presence of velocity dispersion in the foreshock electron measurements allows calculation of the parallel and perpendicular scale size of shock front structure. The 15 May 1997 and 28 August 1998 shocks have evidence for foreshock structure in both the parallel and antiparallel directions, suggesting the presence of a bay in which electron beams can be mirrored and accelerated, generating Langmuir waves and radio emission.

Although foreshock regions upstream of IP shocks imply curved structures, the foreshock regions could theoretically be created by either a curved magnetic field or by a curved shock. Using only measurements made by a single spacecraft, it is impossible to determine which effect predominates. Previous studies focused on ion acceleration have assumed both cases: propagation of a planar shock through a region of curved magnetic fields (Erdos & Balogh 1994), or ion acceleration by repeated encounters with a rippled shock (Decker 1990). It is shown in the previous section that upstream magnetic turbulence alone cannot explain the dimensions of the acceleration regions, and therefore at least a portion of the foreshock region must be created by shock front structure. Regardless of which effect predominates, the methodology used in this paper to estimate the characteristic dimensions of the foreshock regions is valid.

It is unclear at present what causes the observed shock front structure. The curvature may be caused by Alfvén speed inhomogeneities in the solar wind, which can allow different sections of the shock to propagate at different speeds through the heliosphere. Shock reformation, a process in which protons reflected from a shock surface generate upstream instabilities which lead to formation of a new shock front upstream of the original front, may also play a role. One-dimensional hybrid simulations suggest that shock reformation in perpendicular shocks depends on upstream parameters such as Mach number and plasma β (Hellinger et al. 2002). However, more recent two-dimensional studies suggest that perpendicular shock fronts may be dominated by whistler waves, which can inhibit reformation (Hellinger et al. 2007).

Multi-spacecraft missions such as STEREO will be greatly helpful in future investigations of shock structure, and future studies with multi-point measurements should improve current estimates of the frequency and size of IP foreshock regions, which will provide useful input for models of type II generation. If shock front structure is a common feature of IP shocks, then each foreshock region on a shock front would create an independent source of type II radio emission. The spatial variation in upstream plasma density at these multiple source regions could then be responsible for the fine structure observed in many type II bursts.

The authors would like to thank J. C. Kasper for use of the Wind IP shock list. Work at UC Berkeley is sponsored by NASA grants NNG05GH18G and NNX06AF25G. MPP

is supported by the NASA GSRP grant NNG04GN52H. Wind/MFI data is courtesy of the MFI team (PI: R. P. Lepping) at Goddard Space Flight Center. GOES x-ray data is obtained from the National Geophysical Data Center at NOAA.

Chapter 6

Upstream Langmuir Waves

Pulupa, M. P., Bale, S. D., & Kasper, J. C. 2010, J. Geophys. Res., 115, 4106

We have examined 178 interplanetary shocks observed by the *Wind* spacecraft to establish which shock and plasma parameters are favorable for the production of upstream Langmuir waves, and therefore to determine which shocks are likely to generate interplanetary Type II radio bursts. Of the 178 shocks included in this study, 43 produced upstream Langmuir waves, as evinced by enhancements in wave power near the plasma frequency. The large number of observed shocks permits the use of statistical tests to determine which parameters control the upstream activity. The best predictor of activity is the de Hoffmann-Teller speed, a result consistent with the Fast Fermi model of electron acceleration. Several other parameters, including the magnetic field strength and the level of solar activity (but not the Mach number), are also correlated with upstream activity. These additional parameters may be associated with an increased level of shock front curvature or upstream structure, leading to the formation of upstream foreshock regions, or with the generation of an upstream electron population favorable for shock reflection.

6.1 Introduction

Interplanetary (IP) shocks, which are often driven by IP coronal mass ejections (ICMEs), accelerate solar wind electrons into foreshock regions upstream of the shock. These regions are in some respects analogous to the foreshock regions upstream of the bow shocks of magnetized bodies in the solar wind. In both types of foreshock region, the reflected electron beams create unstable bump-on-tail electron distribution functions, which excite a Landau resonance and create electrostatic oscillations known as Langmuir waves. The Langmuir waves undergo a mode conversion process and generate electromagnetic radio

waves at the plasma frequency $f_{\rm p}$ and $2f_{\rm p}$. These radio waves propagate throughout the heliosphere and are used as a remote diagnostic of electron acceleration at shocks. As an IP shock propagates radially outward from the sun, the plasma becomes less dense and the plasma frequency decreases. The radio emission generated upstream of the shock is observed on a radio spectrogram as a slowly drifting, often patchy feature known as an IP Type II radio burst.

IP Type II radio bursts are a primary method used to track the progress of CME-driven shocks through the heliosphere. The decrease in the frequency of Type II emission due to the decrease in local electron density, together with an assumed radial electron density profile, can be used to measure the velocity of the shock (Cane et al. 1982), and this measurement can be used as a tool in space weather forecasting (Cremades et al. 2007). In addition to measurements of radial speed, direction finding techniques can be used to provide information about the three-dimensional structure of the shock (Hoang et al. 1998; Reiner et al. 1998a).

It is still a matter of debate where on the CME-driven shock surface the Type II burst is being generated. It would be very valuable to know if Type II emission is generated where the shock compression is strongest, or where the shock front and upstream magnetic field are favorably aligned, as that would allow us to determine if the emission is always at the nose of the shock, or if it can also occur on the flanks or on the trailing edges. This work is complementary to the direction finding technique of probing Type II burst origins, in that it focuses on direct measurements of the process *in situ* instead of remote reconstruction.

Investigation of IP foreshock regions is guided by previous studies of the terrestrial electron foreshock region. The terrestrial electron foreshock is a commonly observed feature of the quasiperpendicular terrestrial bow shock, and copious *in situ* measurements of electron beams and electrostatic oscillations present in the terrestrial foreshock have been made for several decades. Upstream electrons originating at the bow shock accompanied by plasma frequency noise were observed by the *IMP* and *OGO* spacecraft (Anderson 1968; Scarf et al. 1971). Further upstream observations of electron beams (Anderson et al. 1979; Feldman et al. 1983) and *in situ* measurements of Langmuir waves (Filbert & Kellogg 1979) were made by the *ISEE* and *IMP* spacecraft. These early measurements confirmed that the electron beams appear upstream of the shock when the spacecraft is magnetically connected to the quasiperpendicular bow shock. These observations also established the spatial structure of the electron foreshock, showing that the strongest electron beams and the most intense Langmuir waves occur near the edge of the electron foreshock, where the upstream magnetic field is very nearly perpendicular to the shock normal.

Langmuir waves (Gurnett et al. 1979) and reflected electrons (Potter 1981) were observed upstream of IP shocks, lending the support of *in situ* evidence to the theory of the generation of IP Type II bursts by shock accelerated electrons (Cane et al. 1981, 1987). However, unambiguous *in situ* observation of Type II source regions, including

both wave observations and plasma data which resolve the accelerated electron beams, as first reported by Bale et al. (1999), is rare. This comparative rarity is mainly due to the necessity of high time resolution plasma measurements to resolve the velocity dispersed electron beams which are characteristic of upstream foreshock regions. A previous study (Pulupa & Bale 2008) made use of high cadence 'burst mode' electron measurements to resolve the velocity dispersion of the electron beams and thereby measure the dimensions of the foreshock region. However, burst mode data is unavailable for the majority of shocks observed by the *Wind* spacecraft, and of the shocks with burst mode data, only three presented time-resolved velocity dispersed beams.

Wilson et al. (2007) used the Time Domain Sampler (TDS) instrument from the *Wind* WAVES plasma wave experiment (Bougeret et al. 1995) to study the occurrence of electrostatic waves in the vicinity of interplanetary shocks, showing that the strongest waves occur in the shock ramp itself, and in particular that the shock ramp is dominated by large amplitude ion acoustic waves. TDS selects specific waveform events to send in the telemetry stream, and the selection algorithm preferentially selects large amplitude events. Due to this selection effect, two shocks with similar levels of upstream Langmuir wave activity (LWA) could appear different in the TDS data stream, depending on the level of ion acoustic waves in the ramp or downstream region. Therefore, in order to search for upstream Langmuir waves, we use the low-frequency (4-256 kHz) Thermal Noise Receiver (TNR) from *Wind/WAVES*, which offers continuous coverage in the upstream region and a uniform measurement of upstream activity at each shock. Langmuir waves are apparent in a TNR spectrogram as intense enhancements of wave power at the plasma frequency, and the presence of upstream Langmuir waves is a signature of IP foreshock regions (Bale et al. 1999; Fitzenreiter et al. 2003).

A similar method was employed by Thejappa & MacDowall (2000), who used data from the Ulysses Unified Radio and Plasma experiment to search for Langmuir waves in the vicinity of IP shocks. Thejappa & MacDowall (2000) found that Langmuir waves exist (1) primarily in the upstream region, (2) at both quasiperpendicular and quasiparallel shocks, and (3) primarily at supercritical shocks.

For any given shock crossing by a single spacecraft, the presence or absence of upstream LWA is largely determined by the local shock geometry. Furthermore, the measurements of local shock parameters made at the crossing point will be different from those at the quasiperpendicular acceleration point of the electron beam, introducing uncertainty into the calculation of these parameters and their effect on the acceleration process. Therefore, in order to investigate the effects of different local and global shock parameters, as well as the locally measured solar wind parameters, it is necessary to examine many shocks. *Wind* has been in continuous operation since 1994, and has observed a sufficient number of IP shock crossings to determine statistically which parameters control the production of upstream Langmuir waves.

The structure of the remainder of this paper is as follows: Section 6.2 presents a brief review of the Fast Fermi theory of electron reflection at heliospheric shocks. Section

6.3 discusses the database of *Wind* IP shocks examined in this study, and explains the algorithm used to automatically determine which shocks exhibit Langmuir waves in the upstream region. Section 6.4 describes the shock and plasma parameters computed for each shock, and how the parameters relate to electron acceleration and the generation of foreshock regions. Section 6.5 describes the results, showing which of the calculated parameters control the generation of upstream Langmuir waves, and Section 6.6 briefly discusses the implications of these results for the broader theory of Type II radio bursts.

6.2 Brief Review of Fast Fermi Theory

The Fast Fermi (called 'Fast' because the energization takes place in a single encounter, rather than the multiple encounters of classic Fermi theory) model for the energization of thermal electrons at the terrestrial bow shock was derived independently by Leroy & Mangeney (1984) and Wu (1984). The dynamics of electron acceleration in the Fast Fermi model are most tractable in the de Hoffmann-Teller frame (HTF), in which the upstream plasma bulk velocity and magnetic field are parallel and therefore there is no upstream convective ($\mathbf{V} \times \mathbf{B}$) electric field. The energization of electrons in the upstream solar wind frame is a consequence of the boost to the HTF, the reflection, and the boost associated with the return to the solar wind frame.

The transformation velocity to the HTF from the normal incidence frame (NIF), in which the upstream bulk velocity is antiparallel to the shock normal, is known as the de Hoffmann-Teller velocity, and is given by:

$$\mathbf{V}_{\mathrm{HT}} = \frac{\hat{\mathbf{n}} \times (\mathbf{V}_{\mathrm{u}} \times \mathbf{B}_{\mathrm{u}})}{\mathbf{B}_{\mathrm{u}} \cdot \hat{\mathbf{n}}} \tag{6.1}$$

We denote quantities in the HT frame with a prime, e.g. the parallel $v'_{\parallel}$ and perpendicular $v'_{\perp}$ velocities. $\mathbf{V}_{\mathrm{HT}}$ lies in the shock plane parallel to the projection of the upstream magnetic field into the shock plane. An electron with incoming parallel velocity $v'_{\parallel}$ will be reflected upstream with a parallel velocity $-v'_{\parallel} + 2V_{\mathrm{HT}}$, and with an unchanged perpendicular velocity.

The distribution of the reflected electrons is a loss cone distribution. The opening angle α of the cone is set by the ratio of upstream to downstream magnetic field, according to the relation $\alpha = \sin^{-1}(B_{\mathrm{u}}/B_{\mathrm{d}})$. The loss cone is modified by the presence of a frame-dependent potential across the shock, resulting from the differential motion of protons and electrons through the shock layer. Goodrich & Scudder (1984) showed that electron energy gain is given by Φ', the cross shock potential in the HTF. Φ' affects the reflected distribution by drawing low energy electrons through the shock to the downstream region, broadening the loss cone for low values of $v'_{\parallel}$. This loss cone broadening has been observed in the terrestrial electron foreshock (Larson et al. 1996).

Assuming conservation of μ for the upstream electrons, the criterion for reflection in the HTF is:

$$\frac{1}{2}m\frac{v_\perp'^2}{B_\mathrm{u}} \geq \frac{1}{B_\mathrm{d}-B_\mathrm{u}}\left(e\Phi' + \frac{1}{2}mv_\parallel'^2\right) \tag{6.2}$$

The reflection criterion defines a separatrix in velocity space, which is plotted in Figure 6.1 as a dashed line. Electrons lying above the dashed line will be reflected, while those lying below will pass through the shock to the downstream region.

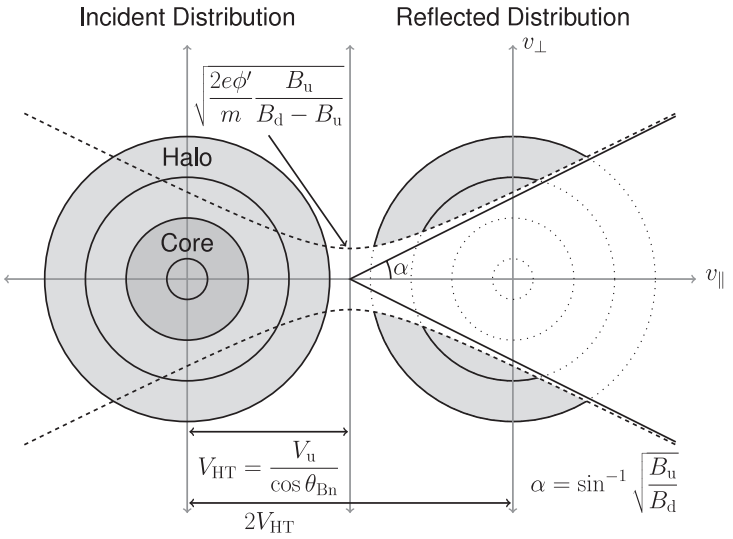

Figure 6.1: Diagram illustrating process for reflection of upstream electrons according to the theory of Leroy & Mangeney (1984) and Wu (1984). The incident distribution is shown on the left in the solar wind frame. Electrons which lie above the separatrix determined by the cross shock potential and mirror ratio (described in Equation 6.2) are reflected, while the remaining electrons pass through the shock to the downstream region. In this figure, the ratio $V_\mathrm{HT}/V_\mathrm{th}$ is exaggerated compared to the measured ratio at a typical IP shock for clarity.

The main difference between the two original papers describing the Fast Fermi model is that Leroy & Mangeney (1984) included the effect of Φ' and used a single Maxwellian to model the electron population, while Wu (1984) did not include Φ' but included the effect of both the halo and core electron populations, using a bi-Maxwellian distribution. Despite these differences, the models yield similar results, and both concur that energization is most efficient when the angle θ_bn between the upstream magnetic field and the shock normal is almost 90°. Test particles injected into hybrid simulations of quasiperpendicular shocks have confirmed this dependence on θ_bn (Krauss-Varban et al. 1989).

Simulations of Fast Fermi acceleration at nonplanar shocks, using parameters similar to those encountered at the terrestrial foreshock, show that parameters such as θ_{bn} can vary significantly during a reflection due to shock curvature. This variation limits the maximum energy of reflected electrons, but effects of this limitation on observed fluxes at a given energy are somewhat offset by focusing effects (Krauss-Varban & Burgess 1991). Curvature may also be important for IP foreshock regions, since the characteristic dimensions of these regions are on the order of the dimensions of the terrestrial bow shock (Pulupa & Bale 2008).

A model (Knock et al. 2001) using the Fast Fermi reflection mechanism to generate an electron beam and stochastic growth theory (Cairns et al. (2000) and references within) to model the conversion of electron beam energy into radio emission has been applied to the foreshock region studied in Bale et al. (1999), and yields results consistent with observations. A refined version of this model (Knock et al. 2003) predicts that foreshock emission is more likely to appear upstream of fast shocks, shocks with more upstream nonthermal electrons, shocks with large radii of curvature, and shocks which propagate through high density upstream regions. Using *Wind* observations of a large number of shocks, we can compare these results with *in situ* data.

6.3 Shock Database and Langmuir Wave Detection Algorithm

We use a database of IP shocks observed by *Wind*, containing 382 interplanetary shocks observed between 1996 and 2004. This IP shock database consists of determinations of the shock orientation and velocity, asymptotic upstream and downstream parameters, and more than fifty derived quantities including wave speeds and Mach numbers. The database is available online[1] for multiple spacecraft, including Wind, and has been successfully used in previous studies of IP shocks ranging from solar cycle effects (Richardson et al. 2006; Zhang et al. 2007) to shock microphysics (Wilson et al. 2007).

We now briefly review the shock analysis methods employed in the database. We start with a merged dataset of solar wind plasma and field observations from the Faraday Cup instruments and the Magnetic Field Investigation (MFI) *Wind* (Ogilvie et al. 1995; Lepping et al. 1995). This database includes ion bulk properties including hydrogen and helium bulk velocities, densities, temperatures, and temperature anisotropies along with high resolution magnetic field measurements averaged to coincide with the Faraday Cup observations. The dataset is available publically from the National Space Science Data Center and has been described in detail previously (Kasper et al. 2006). The solar wind observations are manually scanned for IP shocks, and candidate events exhibiting sudden changes in velocity, density, temperature, and magnetic field strength are added to the database. For each candidate event we then try to identify 10-15 minute long intervals of measurements upstream and downstream of the shock itself that are repre-

[1] http://www.cfa.harvard.edu/shocks/

sentative of asymptotic steady state conditions. Under the assumption that the IP shock is described by the fluid MHD equations and indeed is in a steady state, the change in the plasma parameters across the shock must satisfy the Rankine-Hugoniot (RH) jump conditions. We then follow the algorithms developed by Vinas & Scudder (1986) and Szabo (1994) and identify the shock orientation that best simultaneously satisfies all of the conserved quantities across the shock. In addition to the full RH method, we also employ the velocity and magnetic coplanarity techniques, and three mixed methods that use combinations of the changes of the magnetic field and velocity across the shock (Abraham-Shrauner 1972). For each of the described methods, we determine the shock orientation, shock speed, and asymptotic upstream and downstream plasma values and their uncertainties in the rest frame of the shock. The plasma values are then used to calculate sound, Alfvén, and magnetosonic wave speeds, and, combined with angles the shock makes with the upstream and downstream fields, the slow, intermediate, and fast wave speeds. These speeds and angles are then used to derive any desired fast, slow or critical Mach numbers. For each derived parameter we store the uncertainty in the derivation based on each method, and the overall standard deviation in the value between all of the analysis methods.

We have employed this large number of shock analysis methods because we find that often many of the methods produce a very similar result, while one or two techniques (often the velocity or magnetic coplanarity methods) produce very different results. For each shock the results from each method are compared, outliers are rejected, and a consensus orientation is determined. As has been noted previously (Szabo 1994), it can sometimes be difficult to identify an asymptotic interval, especially in the disturbed region downstream of a shock where fluctuations and sometimes coherent oscillations may be observed. Sometimes, however, even in the presence of these fluctuations, the different methods all produce similar results, and the event is kept in the list of analyzed shocks. If none of the methods agree, or if there is a large uncertainty in the derived parameters, then the shock is marked as questionable and not used in further analysis. Finally, some of the events turn out to be simple discontinuities and not shocks. They are tracked in the database but also excluded.

While the database includes fast, slow, forward, and reverse IP shocks, only fast mode forward shocks were analyzed in this study. In addition to the reasons described above, shocks were also eliminated from this study for other factors, including proximity to the terrestrial foreshock region, concurrent radio signals such as Type III radio bursts, and gaps in the TNR instrument data set. After this selection process, 178 shocks suitable for analysis remained.

Each selected shock was analyzed for large increases in power at the plasma frequency line in the upstream region. In the TNR data, the plasma line is an ubiquitous feature, located roughly at the plasma frequency, created by the potential fluctuations which arise on the antenna due to electron thermal motion (Meyer-Vernet & Perche 1989). Langmuir waves also appear at the plasma frequency, as a bursty feature with a much

higher intensity than the plasma line from the thermal noise. In order to automatically determine which IP shocks exhibit Langmuir waves, the detection algorithm compares the peak upstream power in the vicinity of the plasma line with the background power from the thermal noise spectrum.

The following simple algorithm was used to fit the plasma line upstream of each shock. First, the plasma density, as measured by the PESA-L instrument from the *Wind* 3DP plasma suite (Lin et al. 1995), was used as an estimate of the plasma frequency. A detection algorithm found the plasma peak by searching for the highest TNR value in the vicinity of the expected plasma frequency. The total power in the plasma line for each TNR sample was estimated by summing several bins around the peak bin.

Each shock is assigned a designated score ($P_{\mathrm{LW}}/P_{f_{\mathrm{p}}}$) determined by the ratio of the maximum 'Langmuir Wave' power to the 'plasma wave' power, i.e. the maximum power occurring in a short and bursty interval versus a baseline of quiet time power. The $P_{\mathrm{LW}}/P_{f_{\mathrm{p}}}$ scores for the shocks in the database range from 1.03, for a very quiet and steady upstream region, to 115.16, for a shock with the largest measured upstream Langmuir waves. We choose a $P_{\mathrm{LW}}/P_{f_{\mathrm{p}}}$ score of 10 as the threshold to separate the shocks into two populations, those with upstream LWA and those without. Section 6.5 describes the selection of this threshold in further detail.

Figure 6.2 shows several examples of the Langmuir wave detection algorithm, using three example shocks. The top panel in each plot shows the GSE magnetic field $\mathbf{B}_{\mathrm{GSE}}$ from MFI. The second panel shows the proton density n_{p} as measured by PESA-L. The arrival of the shock can be seen as a sharp jump in plasma density and a discontinuity in the magnetic field. The red vertical line on each plot shows the time of shock arrival, and the black vertical lines delimit the upstream interval where the algorithm searches for Langmuir waves. The third panel shows the spectrogram from TNR. The black and white dashed lines superimposed on the TNR spectrogram show the frequency window containing the bins summed to yield the plasma line power. The final panel shows the power close to the plasma frequency in the upstream region.

The plot on the left is an example of a shock with a quiet, steady upstream region. There is almost no variation in the upstream plasma frequency power, and the shock is assigned a low $P_{\mathrm{LW}}/P_{f_{\mathrm{p}}}$ score of 1.03. The middle plot shows a shock with moderate levels of LWA ($P_{\mathrm{LW}}/P_{f_{\mathrm{p}}} = 11.68$), as shown by two short bursts of increased power near the plasma line. The plot on the right shows a shock with very strong upstream LWA ($P_{\mathrm{LW}}/P_{f_{\mathrm{p}}} = 64.34$.) This shock has been previously studied (Bale et al. 1999; Pulupa & Bale 2008), using *in situ* wave and particle measurements.

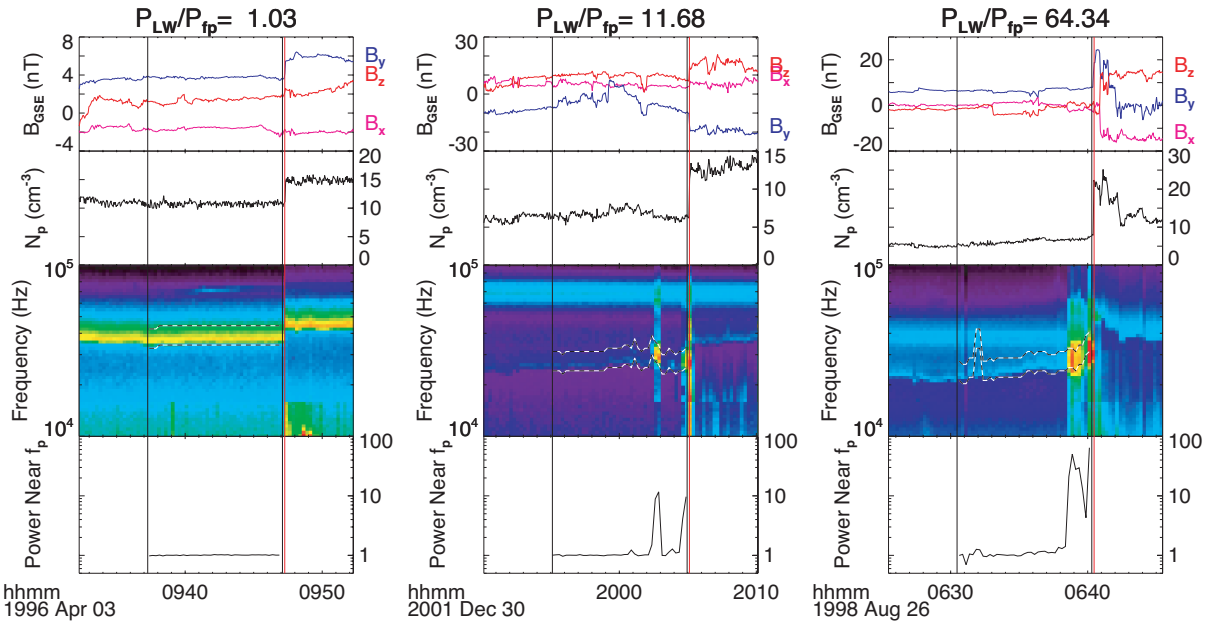

Figure 6.2: Three example shocks illustrating the Langmuir wave detection algorithm described in Section 6.3. From top to bottom, the panels show the GSE magnetic field, the proton density, a spectrogram from the WAVES/TNR instrument, and the power in the vicinity of the plasma line measured by TNR. Large, bursty increases in the power near the plasma line indicate Langmuir waves. The red vertical line marks the arrival of the shock, and the upstream region is denoted by black vertical lines. The white and black dashed lines on the spectrogram show the window over which the TNR power was summed to yield the plasma line power.

6.4 KS Test and Parameter Testing

6.4.1 Test Procedure

As shown in previous sections, the basic mechanism for acceleration of electrons at IP shocks is reasonably well understood, i.e., the electrons are reflected from quasiperpendicular connection sites via a Fast Fermi process. In this respect, IP foreshocks are directly analogous to the terrestrial electron foreshock. However, while the terrestrial foreshock is a steady-state feature of the interaction between the terrestrial magnetosphere and the solar wind, foreshock regions are only seen at a minority of IP shock crossings. Because foreshock regions occupy only a limited area of any given shock front, there is no way to predict with certainty whether an individual IP shock will show evidence of an IP foreshock region for a single spacecraft encounter. We therefore must use statistical methods

to determine the effect of individual shock or plasma parameters on the production of upstream electrons and the resultant Langmuir waves.

The statistical procedure we use for a given parameter x is as follows: choose a threshold value of the $P_{\rm LW}/P_{f_{\rm p}}$ score described in Section 6.3, and from that threshold determine which shocks exhibit upstream LWA. Next, compare the distribution of parameter x for all observed shocks to the distribution of x for the shocks with LWA. We use the Kolmogorov-Smirnov (KS) test to compare the two distributions (Press et al. 1992, §14). The KS test for two sample distributions works by comparing the cumulative distribution functions (CDFs) $S_{\rm N1}(x)$ and $S_{\rm N2}(x)$ of the two samples. The KS statistic $D_{\rm KS}$ measures the maximum distance between the two CDFs:

$$D_{\rm KS} = \max_{-\infty<x<\infty} |S_{\rm N1}(x) - S_{\rm N2}(x)| \tag{6.3}$$

The $D_{\rm KS}$ statistic is a measure of the difference between two distributions. Two samples drawn from the same distribution will lay atop each other when the CDF is plotted (see the $M_{\rm f}$ panel of Figure 6.4 for an example) and will therefore have a small $D_{\rm KS}$, while samples from different distributions will show significant differences (see the $V_{\rm HT}$ panel of the same figure) and $D_{\rm KS}$ will be large. Given the number of samples and the $D_{\rm KS}$ statistic, the probability ($P_{\rm KS}$) that the samples are from the same underlying distribution can be calculated. Parameters with greater influence on the generation of upstream Langmuir waves will have larger differences between the two distributions and, therefore, smaller values of $P_{\rm KS}$.

6.4.2 Tested Parameters

The above procedure can be applied to any continuous shock or plasma parameter and used to determine whether it is correlated with upstream LWA. In this section we list the selected test parameters and explain their relevance to electron acceleration or the formation of foreshock regions. All of the tested parameters, along with the results of the tests, are shown in Figure 6.4.

We test the upstream and downstream magnetic field $B_{\rm u}$ and $B_{\rm d}$, as well as the magnetic compression ratio $B_{\rm max}/B_{\rm u}$. When calculating the mirror ratio, we use $B_{\rm max}$, the maximum value of the magnetic field through the shock transition, including the overshoot region if it is present, since the electron mirror ratio is determined by the maximum B encountered during the reflection process. The downstream magnetic field is measured after any overshoot or undershoot structure. We also test the analogous densities, $n_{\rm u}$, $n_{\rm d}$, and $n_{\rm d}/n_{\rm u}$, although we use the asymptotic downstream value to calculate the density compression.

As can be seen from Figure 6.1, hot electron distribution will contain more electrons which lie above the loss cone in velocity space and can be reflected. The measurement of the downstream thermal velocity $V_{\rm thd}$ is a measurement of electron heating by the shock,

as discussed by Fitzenreiter et al. (2003). We test both the upstream and downstream thermal speeds as well as the ratio $V_{\rm thd}/V_{\rm thu}$. Although the majority of reflected electrons come from the halo portion of the solar wind distribution function, we use the core electron temperature to determine $V_{\rm th}$. This choice was made for ease of computation, and is justified by the correlation between the core and halo temperatures (Feldman et al. 1975). The reflection process will also be affected by temperature anisotropies in the solar wind electron distribution, for this reason we calculate and test the ratio between the perpendicular and parallel electron temperatures, $T_\perp/T_\parallel$.

Plasma β, the ratio of plasma pressure to magnetic pressure, has been linked to the nonstationary structure of shocks (see, e.g., (Hellinger et al. 2002)). We use the total plasma β, including contributions from both ions and electrons. We test $\beta_{\rm u}$ and $\beta_{\rm d}$, as well as the ratio $\beta_{\rm d}/\beta_{\rm u}$. We also measure and test the upstream and downstream solar wind velocities in the shock frame, $V_{\rm u}$ and $V_{\rm d}$.

In addition to the above solar wind plasma parameters, we test various derived shock parameters. $M_{\rm f}$, the fast mode Mach number, given by $M_{\rm f} = V_{\rm u}/V_{\rm f}$, where $V_{\rm f}$ is the speed of the fast mode wave, is a measure of the strength of the shock. The transition from subcritical to supercritical Mach number is generally associated with changes in upstream shock structure due to reformation, and occurs at a fast wave Mach number of 1-2 for typical solar wind plasma conditions (Edmiston & Kennel 1984). Thejappa & MacDowall (2000) found that shocks with Langmuir waves tend to be supercritical.

$V_{\rm s}$ is the measured shock speed in the spacecraft frame, calculated as described in Section 6.3. For CME-driven shocks, higher CME and shock speeds are associated with increased probability that a given CME will drive a Type II-producing shock (Cane et al. 1987; Gopalswamy et al. 2005).

Figure 6.1 shows the effect of V_{HT} and Φ' on the electron reflection process, so these variables are a natural choice to test. Since the fraction of electrons which lie above the velocity space separatrix is dependent on the thermal speed of the electrons, we also test the two parameters normalized to the upstream electron thermal velocity.

$V_{\rm HT}$ is calculated according to Equation 6.1. V_Φ is obtained by setting $v'_\parallel = 0$ in Equation 6.2 and solving for $v'_\perp$. If we approximate Φ' using the relation $e\Delta\Phi' \approx 2\Delta T_{\rm e}$ (Hull et al. 2000), then

$$V_\Phi/V_{\rm th} = \left(2\frac{T_{\rm d} - T_{\rm u}}{T_{\rm u}}\frac{B_{\rm u}}{B_{\rm d} - B_{\rm u}}\right)^{1/2} \tag{6.4}$$

Figure 6.1 shows that a $V_\Phi/V_{\rm th}$ ratio close to or above 1 implies that most of the core electrons cannot be reflected by the shock. This condition obtains for most IP shocks in this study, implying that the halo population is especially important for the formation of the electron beam.

The Fast Fermi theory relies on the adiabatic nature of the electron encounter with the shock. We test $r_{\rm Lh}/(c/\omega_{\rm pi})$, the electron Larmor radius divided by the ion inertial length, to check the validity of this assumption. Simulations (e.g. Burgess (2006)) show

that substructure exists within shock transition regions which is on the order of the ion inertial length $c/\omega_{\rm pi}$, so this is the relevant length scale for reflection. Therefore, the ratio of a halo electron Larmor radius to $c/\omega_{\rm pi}$ is a measure of how well the assumption of small gyroradius (and therefore adiabatic motion) ought to hold. Numerically, $r_{\rm Lh}/(c/\omega_{\rm pi})$ is equivalent to $(mv_h)/(Mv_{\rm A})$ and is given by:

$$\frac{r_{\rm Lh}}{c/\omega_{\rm pi}} = \left(\frac{mv_{\rm h}}{eB}\right)\frac{1}{c}\left(\frac{ne^2}{\varepsilon_0 M}\right)^{1/2} = \frac{mv_h}{Mv_{\rm A}} \approx 0.015 \cdot \frac{E_{\rm h}({\rm eV})^{1/2} \cdot n({\rm cm}^{-3})^{1/2}}{B({\rm nT})} \tag{6.5}$$

where $E_{\rm h} = \frac{1}{2}mv_{\rm h}^2$ is the energy of a halo electron, typically about 6 times the energy of a core electron (Feldman et al. 1975). We use $B_{\rm max}$, the maximum magnetic field observed in the shock transition, in Equation 6.5, and the downstream value for the density $n_{\rm d}$.

Finally, we calculate and test the effect of SSN, the daily sunspot number, a standard measure of solar activity. The sunspot number used for any given shock is the daily number for the day the shock was launched, as opposed to the day the spacecraft encountered the shock. We choose this convected sunspot number as a rough measure of the complexity of structure in the solar wind through which the shock will propagate.

6.5 Results

As mentioned in Section 6.3, we choose a threshold value of $P_{\rm LW}/P_{f_{\rm p}}$ to distinguish between shocks with LWA and those without. In the top panel of Figure 6.3, the number of shocks with $P_{\rm LW}/P_{f_{\rm p}}$ greater than a given threshold (i.e., the number of shocks $N_{\rm LW}$ with LWA) is plotted versus threshold value. A histogram of $P_{\rm LW}/P_{f_{\rm p}}$ is also plotted. It is not immediately apparent from the $N_{\rm LW}$ plot or the histogram that there are two distinct populations of shocks, although the histogram data shows a minimum around a $P_{\rm LW}/P_{f_{\rm p}}$ value of 10, possibly indicating a break between populations. To confirm that this value is a good separator, we use the KS test. The bottom panel of Figure 6.3 shows variation of $P_{\rm KS}$ with different choices of $P_{\rm LW}/P_{f_{\rm p}}$ threshold for several of the parameters described in Section 6.4.

All parameters start at a $P_{\rm KS}$ value of 1, a result of the trivial equality of the two populations when there is no required increase in activity near the plasma line for a shock to be counted as a Langmuir wave shock. Parameters which have a strong controlling effect on LWA will tend toward low values of $P_{\rm KS}$. Several of the predictive parameters plotted in Figure 6.3 ($V_{\rm HT}$, SSN, $B_{\rm max}/B_{\rm u}$) show a sharp downward trend followed by more stable behavior starting at threshold values of $\sim 8-10$, justifying use of 10 as a $P_{\rm LW}/P_{f_{\rm p}}$ threshold. Beyond this point, no parameter shows increased predictive ability. We therefore use for the remainder of this paper a $P_{\rm LW}/P_{f_{\rm p}}$ score of 10 to separate the two populations of shocks. A total of 43 shocks out of the 178 forward shocks analyzed (24%) produced upstream Langmuir waves, which agrees quite well with the result of Thejappa

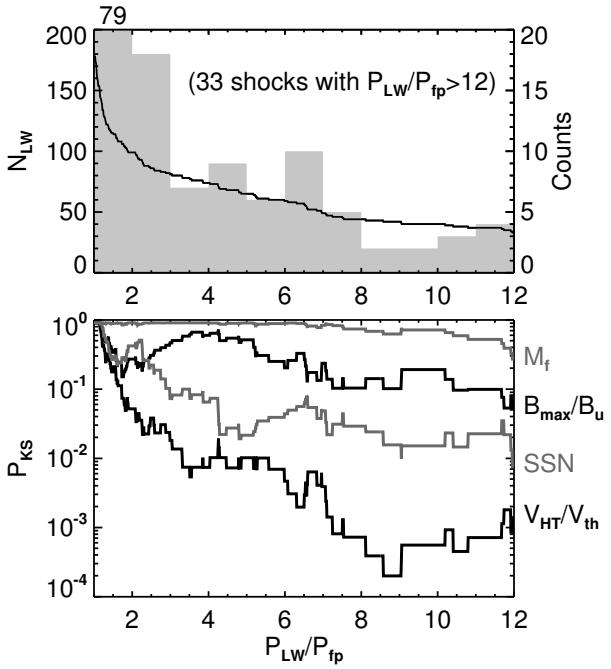

Figure 6.3: The top panel plots the number of shocks exhibiting upstream Langmuir waves versus threshold $P_{\rm LW}/P_{f_{\rm p}}$, showing that there is no clear cutoff value for LWA. A histogram of $P_{\rm LW}/P_{f_{\rm p}}$ values is also plotted, with the right axis showing the counts in each histogram bin. 79 shocks lie in the lowest bin. The bottom panel shows P_{KS} values for different threshold values of $P_{\rm LW}/P_{f_{\rm p}}$. The $P_{\rm KS}$ statistic varies considerably for many tested parameters for threshold values of $P_{\rm LW}/P_{f_{\rm p}}$ ranging from 1 to 8, but after 8 the $P_{\rm KS}$ remains fairly steady, justifying the selection of a threshold value of 10.

& MacDowall (2000), who observed upstream activity at 31 of 160 interplanetary shocks (19%), and at 22 of 97 forward shocks (23%).

Most tested parameters, both measured and derived, show some association with upstream Langmuir wave activity, as can be seen by examining the CDF plots in Figure 6.4. The direction of the effect, i.e. whether an increase or decrease in the parameter is associated with activity, is apparent from which direction the red line (shocks with LWA) in the KS plot is shifted compared to the black line (all shocks.) The magnitude of the effect is shown by $P_{\rm KS}$, which is the probability that the LWA CDF for a given parameter could be drawn randomly from the distribution of all shocks. Following Press et al. (1992, §14), we use $P_{\rm KS} \sim 0.2$ as a rough dividing line between parameters which have a significant effect on LWA and those that do not—for parameters with $P_{\rm KS} >\sim 0.2$ the KS test essentially states that there is no statistically significant difference between the two distributions.

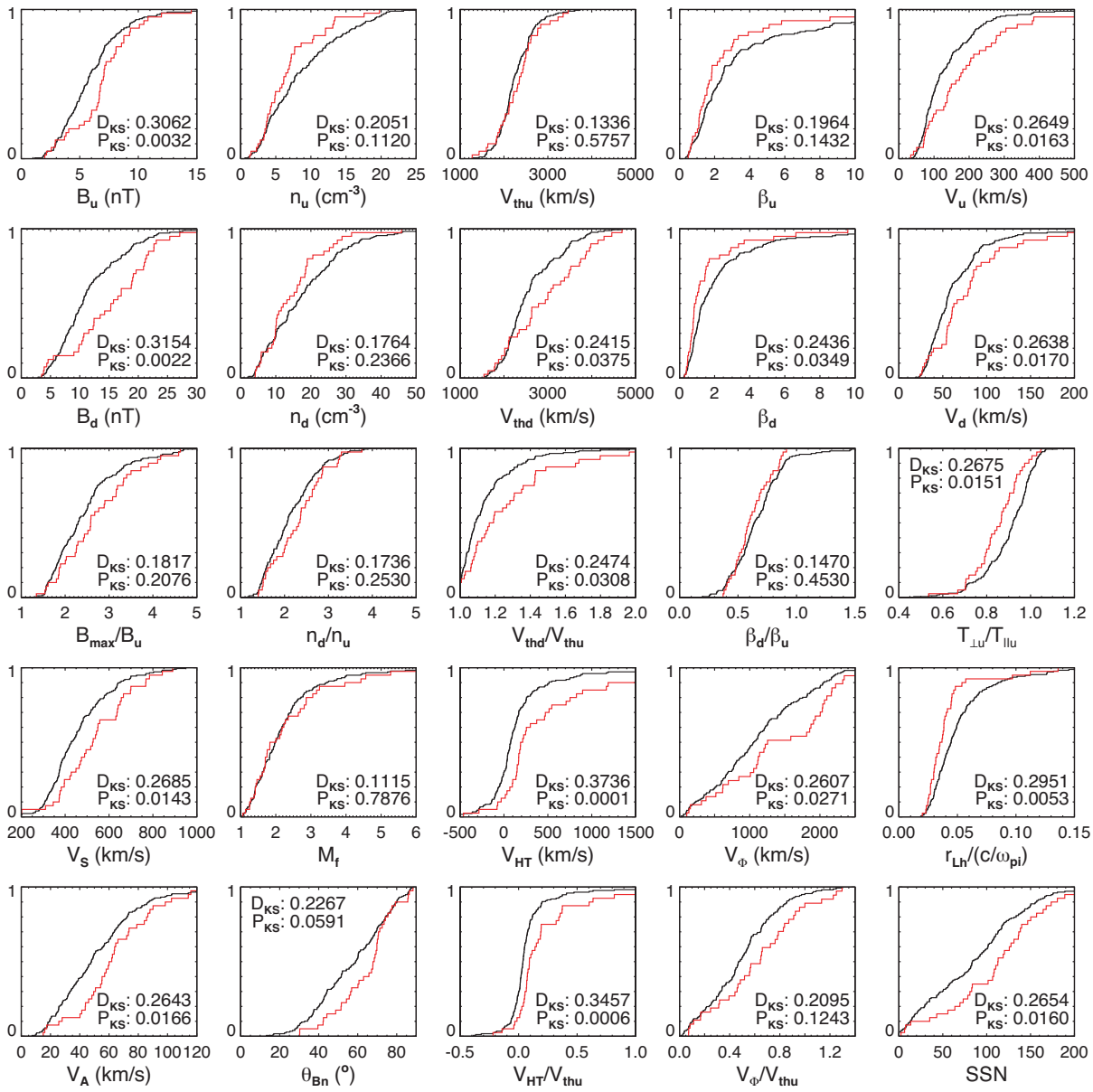

Figure 6.4: Results of the Kolmogorov-Smirnov test for the selected shock and plasma parameters. In each panel, the black line shows the CDF for all shocks. The red line shows the CDF for the subset of shocks which exhibit upstream Langmuir waves. The maximum difference between the two populations (the $D_{\rm KS}$ statistic) can be used to calculate the probability ($P_{\rm KS}$) that the two populations come from the same underlying distribution.

Quantity	D_{KS}	P_{KS}
V_{HT}	0.3736	0.0001
$V_{\mathrm{HT}}/V_{\mathrm{thu}}$	0.3457	0.0006
B_{d}	0.3154	0.0022
B_{u}	0.3062	0.0032
$r_{\mathrm{Lh}}/(c/\omega_{\mathrm{pi}})$	0.2951	0.0053
V_{S}	0.2685	0.0143
$T_{\perp \mathrm{u}}/T_{\parallel \mathrm{u}}$	0.2675	0.0151
SSN	0.2654	0.0160
V_{u}	0.2649	0.0163
V_{A}	0.2643	0.0166
V_{d}	0.2638	0.0170
V_{Φ}	0.2607	0.0271
$V_{\mathrm{thd}}/V_{\mathrm{thu}}$	0.2474	0.0308
β_{d}	0.2436	0.0349
V_{thd}	0.2415	0.0375
θ_{Bn}	0.2267	0.0591
n_{u}	0.2051	0.1120
$V_{\Phi}/V_{\mathrm{thu}}$	0.2095	0.1243
β_{u}	0.1964	0.1432
$B_{\mathrm{max}}/B_{\mathrm{u}}$	0.1817	0.2076
n_{d}	0.1764	0.2366
$n_{\mathrm{d}}/n_{\mathrm{u}}$	0.1736	0.2530
$\beta_{\mathrm{d}}/\beta_{\mathrm{u}}$	0.1470	0.4530
V_{thu}	0.1336	0.5757
M_{f}	0.1115	0.7876

Table 6.1: For each tested parameter, the Kolmogorov-Smirnov statistic (D_{KS}) and the associated significance (P_{KS}), comparing the distribution of all shocks to shocks with Langmuir waves, and using a $P_{\mathrm{LW}}/P_{\mathrm{fp}}$ threshold of 10.

Since many of the derived parameters are combinations of the measured parameters, comparing the relative $P_{\rm KS}$ values allows us to determine which components of derived quantities are most crucial to the physics of electron acceleration. For example, the best predictor of LWA is the de Hoffmann-Teller speed $V_{\rm HT}$. The calculation of $V_{\rm HT}$ incorporates both $\theta_{\rm bn}$ and $V_{\rm u}$, and comparison of the relative $P_{\rm KS}$ scores shows that $V_{\rm HT}$ is a much better predictor than either measured parameter by itself.

This case can be contrasted with $r_{\rm Lh}/(c/\omega_{\rm pi})$, which is also strongly associated with LWA. However, the absolute strength of the magnetic field are better predictors than the derived quantity $r_{\rm Lh}/(c/\omega_{\rm pi})$, so we can conclude that B is the most important factor in determining the validity of the adiabatic reflection assumption, for the typical range of parameters encountered in the solar wind. In terms of the physics of electron reflection, this corresponds to the fact that in regions of low magnetic field, electrons can become demagnetized and drift away from regions where acceleration is favored.

The strength of the cross shock potential, expressed as a critical velocity V_ϕ for reflection, is also associated with increased LWA. The normalized quantities $V_{\rm HT}/V_{\rm th}$ and $V_\phi/V_{\rm th}$ are roughly equally good as predictors as the unnormalized quantities, despite the fact that higher thermal velocities should lead to more and higher energy electrons reflected from the shock front. This contradiction can be explained by observing that V_ϕ is of the order of $V_{\rm th}$, and that therefore most of the core thermal population of electrons will be drawn through the shock front by the cross shock potential into the downstream region. Therefore, the relevant population of electrons is the halo. Although the density and temperature of the halo are well correlated to the density and temperature of the core (Feldman et al. 1975), the variation in these parameters and the fact that the bulk velocity of the halo may not coincide with the core bulk velocity means that the core thermal speed is an imprecise proxy for the thermal speed of the reflected electrons.

Surprisingly, the temperature anisotropy analysis shows that shocks with low $T_\perp$ are correlated with LWA, despite the fact that high $T_\perp$ should lead to more reflected electrons, according to Equation 6.2. This result may also be due to the difference between the core and halo population—the measured temperature anisotropy we use is for the core population, and the statistics of the halo anisotropy are quite different. (Štverák et al. 2008)

A significant finding of Thejappa & MacDowall (2000) was that Langmuir waves occur upstream of both quasiperpendicular shocks and quasiparallel shocks. We confirm this finding, however, we find that quasiperpendicular shocks are highly favored to produce upstream waves, as expected from Fast Fermi theory. The few instances of quasiparallel shocks with observed LWA may be a result of the fact that the single spacecraft measurement of $\theta_{\rm bn}$ is made at the point that the spacecraft crosses the shock, and not at the point on the shock where the electrons are accelerated. Nonplanar shock structure and curvature or diffusion of the upstream magnetic field could cause the measurement of $\theta_{\rm bn}$ to differ between these two points.

Both the magnetic compression and the density compression ratios exhibit only a

weak relationship with LWA compared to those due to the upstream and downstream absolute values of B and n. In the case of the magnetic compression, this implies that the opening angle α of the magnetic mirror has a much smaller influence on the appearance of upstream waves than does B or V_{HT}.

We find that the fast Mach number M_{f} of the shock is unimportant in predicting LWA. This is true despite the fact that both the shock velocity V_{s} and the Alfvén velocity V_{A} are reasonably good predictors of upstream activity. The dependence of LWA on V_{A} is likely due to the dependence of V_{A} on B. Since high V_{s} and high V_{A} are both correlated with upstream activity and both correlations are comparable in magnitude, the combined effects effectively cancel out dependence on M_{f}. However, this result is not inconsistent with the findings of Thejappa & MacDowall (2000) that most LWA is found upstream of supercritical shocks—we suggest that it is simply a corollary of the fact that most IP shocks are supercritical at helioradial distances equal to or greater than 1 AU.

We also find that the sunspot number is quite good as a predictor of upstream LWA at a given shock. There are two possible explanations for this effect. The first is that the variation in the solar cycle causes variation in shock and plasma parameters which control LWA. Several solar wind parameters are correlated well with solar activity, including wind speed and magnetic field (see, e.g. Veselovsky et al. (2000)). However, electron heat flux does not vary with solar activity (Scime et al. 2001). The other explanation is that shock structure may be sensitive to the environment into which the shock propagates through the heliosphere. A shock propagating into a relatively quiet solar wind environment, such as that found during periods of low solar activity, encounters a more homogeneous environment than a shock propagating into the relatively variable solar wind existing during periods of intense solar activity. Inhomogeneities may lead to differences in shock formation and a greater level of structure on the front of the shock, creating favorable conditions for the generation of foreshock bays.

Table 6.1 lists all of the analyzed shock and plasma parameters, in order of decreasing correlation with upstream Langmuir wave activity.

6.6 Discussion and Summary

The results of the previous section emphasize the complexity of Type II radio burst generation. Pulupa & Bale (2008) have shown that the characteristic scale of foreshock bays is on the order of tens to hundreds of Mm, but parameters on scales both significantly smaller ($r_{\mathrm{Lh}}/(c/\omega_{\mathrm{pi}})$, which describes structure on the scale of the shock width) and significantly larger (SSN, which serves as a proxy of structure in the entire solar wind) than this also play a role in determining the existence of upstream Langmuir waves.

A picture of the dependence of Type II radio bursts on shock and plasma parameters emerges from these results, as follows: An IP shock is launched into the heliosphere. If the shock propagates into a highly inhomogeneous environment, it is likely to develop

structure on the shock front, which by 1 AU has the characteristic dimensions of the observed foreshock bays. A shock which forms a foreshock region can accelerate electrons effectively to form electron beams and Langmuir waves, if the following conditions apply: the local HT speed is large compared to the speed of the typical halo electron, and the magnetic field is strong enough to keep the electron bound to a quasiperpendicular acceleration site throughout its encounter with the shock. For a given shock crossing, whether the spacecraft encounters LWA depends on the exact location of the crossing on the shock front.

In summary, we have surveyed a large number of shocks observed by the *Wind* spacecraft, searching for upstream Langmuir waves using the TNR instrument on *Wind/WAVES* and statistically analyzing the data set to determine which parameters affect upstream activity. We show that $V_{\rm HT}$ is clearly the best predictor of upstream LWA. This agrees well with the predictions of Fast Fermi theory. We confirm the conclusions of Thejappa & MacDowall (2000) that LWA occurs upstream of slightly more than 20% of interplanetary fast shocks, and that activity occurs upstream of both quasiperpendicular and quasiparallel shocks. However, we note that there is a strong preference for quasiperpendicular shocks, and that observations of quasiparallel shocks may be an artifact of nonlocal measurements of the upstream connection site. Of the parameters measured by both this study and calculated by Knock et al. (2003), we agree that upstream activity is very sensitive to the upstream speed of the shock. However, we find that shocks with lower rather than higher upstream densities are favored for LWA. We show an intriguing relationship between LWA and solar activity, which may indicate that structure in the solar wind leads to corresponding structure on shock fronts. The ratio between the Larmor radius and the ion inertial length is also a good predictor of upstream activity, which suggests that the microphysics of shock structure also is important. The large number of parameters which are associated with upstream LWA underscores the complexity of Type II burst generation and suggests that a complete model of Type II generation must include both the microphysics of shock structure and the global view of the solar wind into which the IP shock is propagating.

Work at UC Berkeley is sponsored by the NASA grant NNX08AE34G. Wind/MFI data is courtesy of the MFI team (PI: R. P. Lepping) at Goddard Space Flight Center.

Chapter 7

Upstream Electron Beam

The previous results presented in this thesis have dealt with electron acceleration at interplanetary shocks. This chapter deals with observations of the electrons accelerated by the terrestrial bow shock which were made by the STEREO/Behind spacecraft shortly after its launch. Two individual electron events are analyzed in this chapter. The combined capabilities of the SWEA and STE instruments on the STEREO spacecraft can resolve the accelerated electron foreshock spectrum from several eV to 100 keV. The highest observed electron beam energies reach up to several tens of keV. These energies are of particular interest because electrons at keV energies and higher have Larmor radii of tens of km or greater, and therefore the adiabatic condition ($r_{\mathrm{Le}} \ll c/\omega_{\mathrm{pi}}$), on which the Fast Fermi theory is based, no longer applies.

7.1 STEREO Early Orbit

The STEREO spacecraft were launched in late 2006. For the first several weeks of the mission, both spacecraft were in a petal orbit with an apogee of roughly 65 R_{E}. The early orbit of the STEREO/Behind spacecraft is shown in Figure 7.1 in geocentric solar ecliptic (GSE)[1] coordinates. Near the end of 2006, the spacecraft used lunar encounters to separate and begin moving away from the Earth in different directions (the first lunar encounter can be seen on the orbit plot as a kink near December 16).

At 1 AU, the nominal Parker spiral angle lies in the ecliptic plane and points approximately 45° above the $-\mathbf{x}_{\mathrm{GSE}}$ axis. Both STEREO spacecraft therefore spent significant time magnetically connected to the terrestrial bow shock during the first two months of the mission. The region upstream of the bow shock which is magnetically connected to

[1] $\mathbf{x}_{\mathrm{GSE}}$ is in the direction of the Sun-Earth line pointing sunward, $\mathbf{z}_{\mathrm{GSE}}$ points north out of the ecliptic plane, and $\mathbf{y}_{\mathrm{GSE}}$ completes the right-handed triple.

the shock is known as the foreshock, and is subdivided into the electron and ion foreshocks. Electrons, which travel more quickly than ions, can more easily escape from the shock front and reach distances far upstream of the shock, while ions are restricted to areas of the foreshock that are farther downstream (Eastwood et al. 2005), so the electron foreshock extends farther in front of the Earth. In terms of shock geometry, this implies that the electron foreshock is connected to the quasiperpendicular region of the bow shock, while the ion foreshock is a feature of the quasiparallel region.

As mentioned in previous chapters, observations of shock-accelerated electrons (Anderson et al. 1979; Fitzenreiter 1995) and Langmuir waves (Filbert & Kellogg 1979) are common in the electron foreshock. The foreshock Langmuir waves have been studied in detail by Malaspina et al. (2009), who found a power law relation between Langmuir wave amplitude and distance from the shock, consistent with a model including the effects of density fluctuations on the propagation of the electron beam and generation of radiation. The locations of electron events observed by STEREO/Behind are shown in Figure 7.1 as red circles. It should be noted that during the early part of this period, a solar active region was producing multiple Type III radio bursts (Eastwood et al. 2010), and so some of the electron events in Figure 7.1 may not be associated with the foreshock. However, the selected events presented in this chapter occur during a period free of radio bursts and are therefore associated with foreshock and not solar activity.

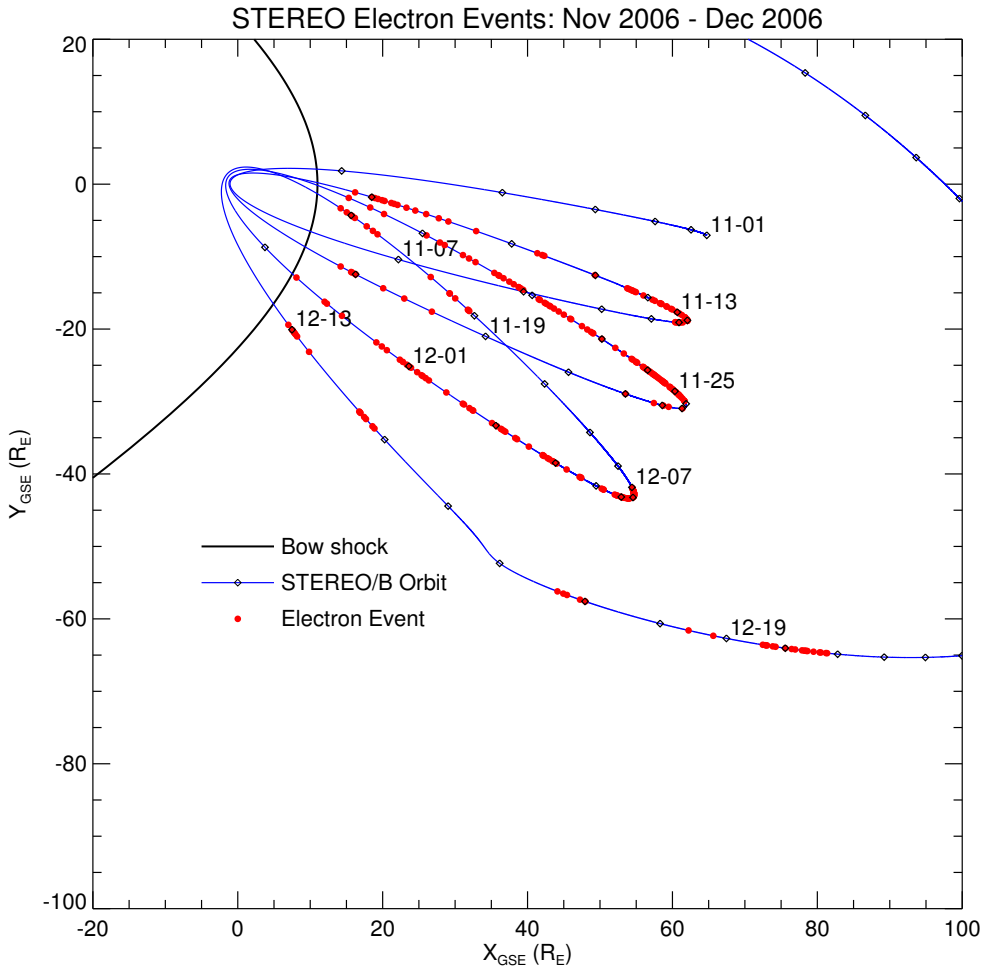

Figure 7.1: STEREO orbit during late 2006 in GSE coordinates. Each day is marked with a black diamond. Each electron event is marked with a red circle.

7.2 Reflected Electron Beam

Figure 7.2 shows an electron event (which will be referred to as Event 1 throughout this chapter) observed by the STEREO/Behind spacecraft on 2006 December 20 at approximately 0730 UT. The top panel shows the magnetic field at the spacecraft in GSE coordinates. The fact that the $\mathbf{x}_{\mathrm{GSE}}$ component of the magnetic field is negative implies that particles traveling with pitch angles $< 90°$ are traveling in the antisunward direction, while particles with pitch angle $> 90°$ are traveling in the sunward direction (this includes particles accelerated by the terrestrial bow shock). The second panel shows the electrostatic Langmuir waves generated by the foreshock electron beam.

The third panel shows an energy spectrogram from the STE instrument. Units for the scale on the right of this panel are counts. The electron beams are the features which originate and have the highest count levels at low energies, and which extend up to tens of keV. Also seen are features (examples are at 07:15 UT, 07:32 UT and (above an electron beam) at 07:36 UT) which start at around 10 keV and extend up to the top of the STE energy range. These features are probably ions accelerated from the bow shock, since electron features at these energies would constitute a very unstable bump on tail electron beam. At all times, there is a background level of superhalo solar wind electrons.

The fourth and fifth panels are pitch angle distribution (PAD) plots for the STE instrument. The STE PADs illustrate the variable amount of pitch angle coverage provided by the instrument, and its dependence on the magnetic field. It is apparent that the $\mathbf{z}$ component of magnetic field is dominant in determining the amount of pitch angle information that can be obtained from STE observations (see Figure 4.6). From about 7:25 to 7:30, STE observes electron beams, has sufficient angular coverage to determine that the beams originate from the bow shock, and does not observe simultaneous ion events.

The final two panels show PADs for the SWEA data, displaying sunward-traveling electron beams from the bow shock. The anti-sunward beam present in the small pitch angle SWEA data is possibly a signature of the electron strahl.

Figure 7.3 shows the incident solar wind electron spectrum for Event 1. The incident distribution function is a combination of a thermal (Maxwellian) core and suprathermal halo and superhalo κ distributions, as described in Chapter 3. For all three components, there is not a major difference between the parallel (red) and perpendicular (blue) spectra,[2] so we can model each component using an isotropic ($T = T_{\perp} = T_{\parallel}$) distribution with no offset (Δ_{c}) between the core and halo. Equation (3.1) can then be parametrized by an amplitude a_{c} representing the constant factor outside of the exponential, and a single temperature T_{c}. The κ distributions can similarly be represented by a constant

[2]For each event presented here, STE D3 was the bin closest to perpendicular in pitch angle. Several of the lowest STE D3 energy bins during this time period are noisy, and these bins have been removed from the spectra.

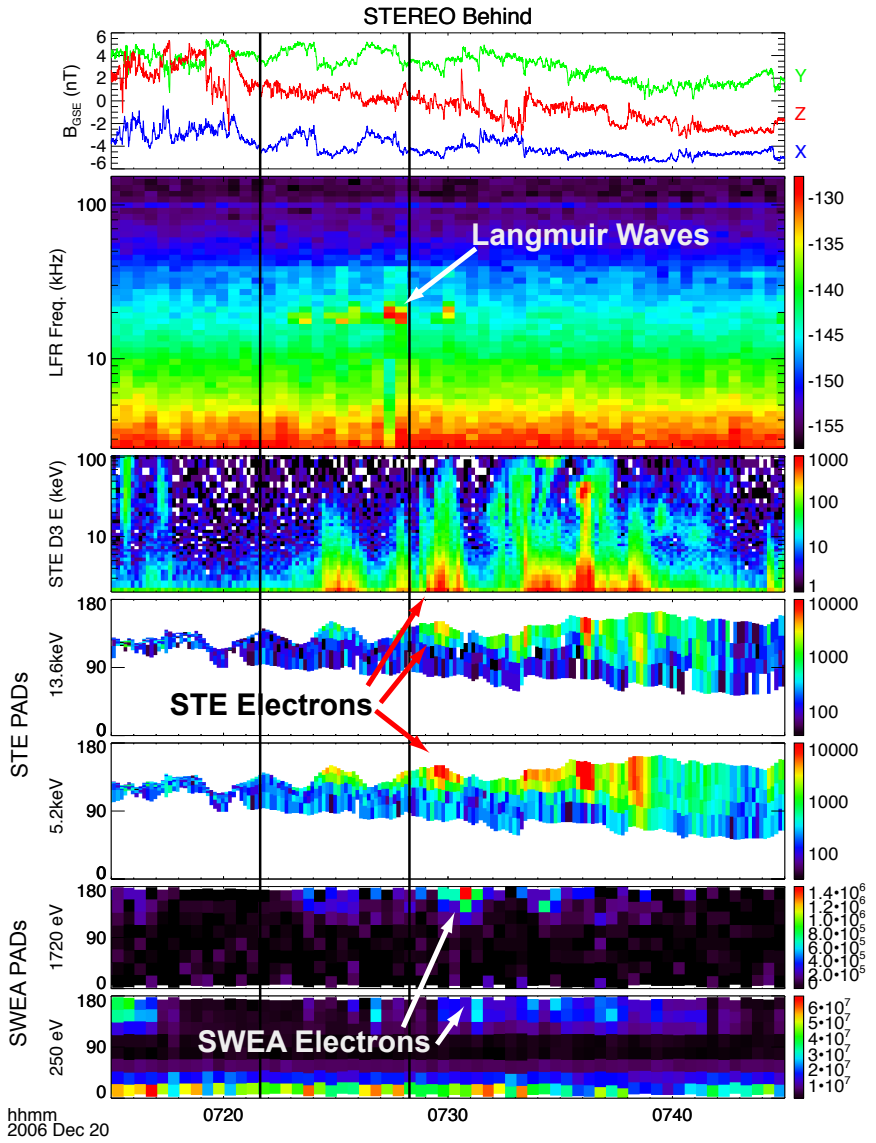

Figure 7.2: Upstream electron event (Event 1) observed by STEREO/Behind on 2006 December 20 at approximately 07:30 UT. The top panel shows the GSE magnetic field. The second panel shows Langmuir waves observed with LFR. The third panel shows an energy spectrogram for one of the STE detectors. The fourth and fifth panels show STE PADs, and the final two panels show SWEA PADs. The electron beam is apparent in the spectrogram and all of the PAD plots. Units for the LFR spectrum are dB (V^2/Hz). Units for the energy spectrogram are counts, for all PADs the units are units of energy flux, eV/sec/cm^2/ster/eV. The vertical black bars show the times for the analyzed incident and foreshock distribution functions.

($a_{\rm h}$ for the halo, $a_{\rm s}$ for the superhalo), a temperature ($T_{\rm h}$ and $T_{\rm s}$) and a value for κ ($\kappa_{\rm h}$ and $\kappa_{\rm s}$). These fit values are listed in Table 7.1.

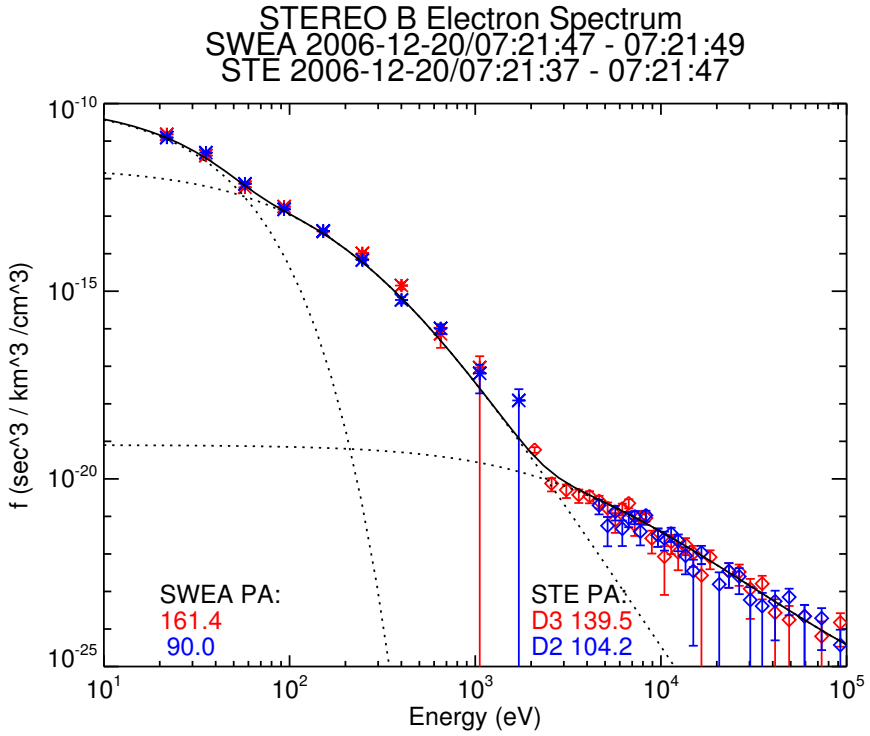

Figure 7.3: Incident electron spectrum observed by STEREO/Behind: 2006 Dec 20, 07:21 UT. The spectrum consists of a thermal core, a κ halo, and a κ superhalo. Each separate component of the fit is plotted as a dotted line, and the sum is plotted as a solid black line. Points from the SWEA detector are marked with asterisks, while points from STE are marked with diamonds. The blue points represent sectors of each detector that are pointed nearly perpendicular to the magnetic field (PA $\approx 90°$), while the red points represent sectors which are pointed nearly antiparallel to the magnetic field (PA $\approx 180°$). The magnetic field is pointed anti-sunward (see Figure 7.1), so the antiparallel pitch angles contain particles from the direction of the bow shock. Parameters for the fit are listed in the text.

For a given incident distribution function $f_{\rm i}$, the reflected distribution function $f_{\rm r}$ created by the Fast Fermi process is a function of three parameters: the mirror angle α of the magnetic field jump, the HT velocity $\mathbf{V}_{\rm HT}$, and the cross shock potential ϕ. It is difficult to accurately determine these parameters, especially at a distance of more than 100 $R_{\rm E}$ upstream of the bow shock. The mirror angle α is estimated as approximately 30°, which is the mirror angle given by the magnetic field jump ($B_{\rm d}/B_{\rm u} = 4$) in the limit

Event Times	Event 1	Event 2
Incident Dist. Time Interval (SWEA)	07:21:47–07:21:49	15:58:17–15:58:19
Incident Dist. Time Interval (STE)	07:21:37–07:21:47	15:58:17–15:58:27
Foreshock Dist. Time Interval (SWEA)	07:28:17–07:28:19	16:01:47–16:01:49
Foreshock Dist. Time Interval (SWEA)	07:28:07–07:28:17	16:01:47–16:01:57
Incident Distribution Fit Parameters	Event 1	Event 2
a_c [sec^3/km^3/cm^3]	1.0×10^{-10}	0.9×10^{-10}
T_c [eV]	10.	11.
a_h [sec^3/km^3/cm^3]	2.0×10^{-12}	1.0×10^{-12}
T_h [eV]	33.	40.
κ_h	6.7	9.8
a_s [sec^3/km^3/cm^3]	8.0×10^{-20}	4.5×10^{-20}
T_s [eV]	1140.	1250.
κ_s	2.8	2.6
Fast Fermi Parameters	Event 1	Event 2
α	30°	30°
$\mathbf{V}_{HT}$ [km/s]	7.5×10^3	1.8×10^4
ϕ [eV]	20.	25.

Table 7.1: Event times and incident distribution and Fast Fermi acceleration fit parameters for the upstream electron events presented in this chapter.

of a strong shock. This is consistent with the shock jump observed at the STEREO bow shock crossing previous to Event 1 and 2. However, that crossing was a week prior to these observations. $\mathbf{V}_{\mathrm{HT}}$ and ϕ are determined from the spectrum of reflected electrons, as described in the following paragraphs.

Figure 7.4 shows a two-dimensional contour plot of f_{r}, similar to Figure 6.1. The boundary of the loss cone is plotted as a dotted line. The bottom horizontal scale shows the parallel velocity in the solar wind frame, while the top scale shows the velocity in the HT frame. The unstable bump on the tail of the electron distribution is flattened by a quasilinear process ((Robinson & Benz 2000), see also references in Chapter 3). Figure 7.5 shows the results of a quasi-linear relaxation model for Event 1. The beam produced by the Fast Fermi acceleration is shown as a dotted line, and the plateau to which the beam decays is shown as a solid line. The distribution function for velocities outside of the area marked by the dashed vertical lines is unchanged by the relaxation process. These dashed lines are also plotted on Figure 7.4. Also plotted in Figure 7.4 are the locations and approximate widths of the SWEA and STE detector bins, with SWEA bins again marked with asterisks and STE bins with diamonds, and with blue and red representing the perpendicular and parallel bins.

The observed foreshock (reflected) electron spectrum is shown in Figure 7.6. As is apparent from Figure 7.4, the quasilinear relaxation energy regime is different for the perpendicular and parallel spectra. The solid lines are curves showing the spectrum in the absence of quasilinear relaxation. Therefore, we should not expect the spectra and the fits to match in the regimes denoted 'QL'. However, outside of the quasilinear regime the spectra should match if the Fast Fermi theory holds and we have determined the correct values of $\mathbf{V}_{\mathrm{HT}}$ and ϕ.

The fitting procedure, then, consists of varying $\mathbf{V}_{\mathrm{HT}}$ and ϕ until the following criteria are satisfied as far as can be achieved: (a) the start of the rise in the Fast Fermi parallel spectrum (i.e., the low end of the red QL bar in Figure 7.6) occurs at the same point where the measured parallel spectrum starts to depart from the measured perpendicular spectrum, and (b) the high energy tail of the Fast Fermi spectrum, which ought to be unaffected by the quasilinear flattening, matches well with its measured counterpart for both the parallel and perpendicular case.

For Event 1, the Fast Fermi parameters can be adjusted to provide reasonable values for both the start of the rise and for the high energy tails. However, for the lower end of the parallel STE energies (from about 2-5 keV) lie beyond the QL region but show signs of lower flux, indicating that the quasilinear relaxation process may leak beyond its boundaries as defined in Figure 7.5.

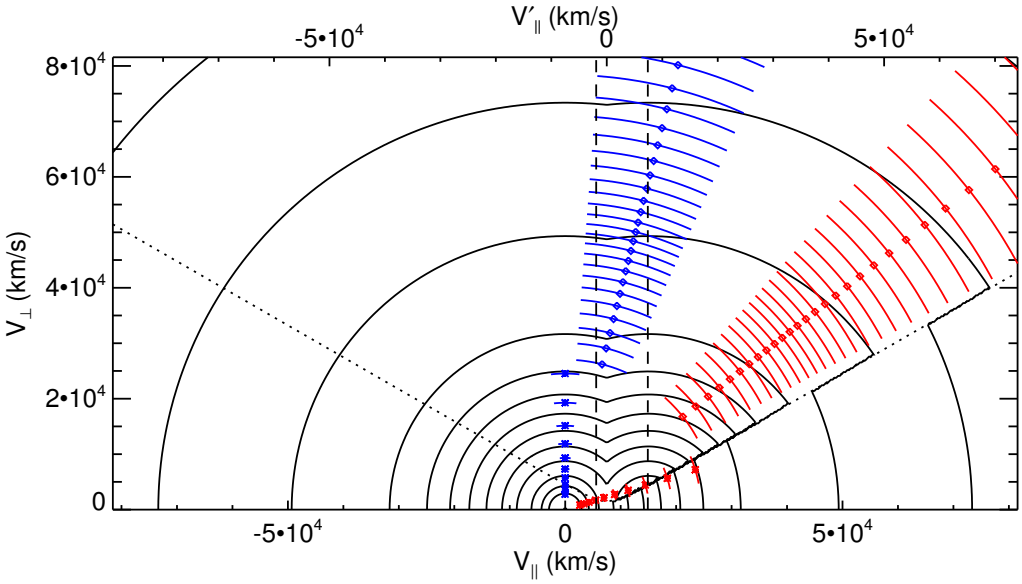

Figure 7.4: Fast Fermi plot with location of pitch angle bins for STE and SWEA detectors in phase space, for the foreshock electron spectrum observed by STEREO/Behind: 2006 Dec 20, 07:28 UT (compare to Figure 6.1). Points from the SWEA detector are marked with asterisks, while points from STE are marked with diamonds, and perpendicular and antiparallel pitch angle bins are colored blue and red, respectively. The arcs which intersect each point show the approximate width in pitch angle of the detector bins. The vertical dashed lines show the limits of the region affected by quasilinear relaxation of the electron distribution function (see Figure 7.5).

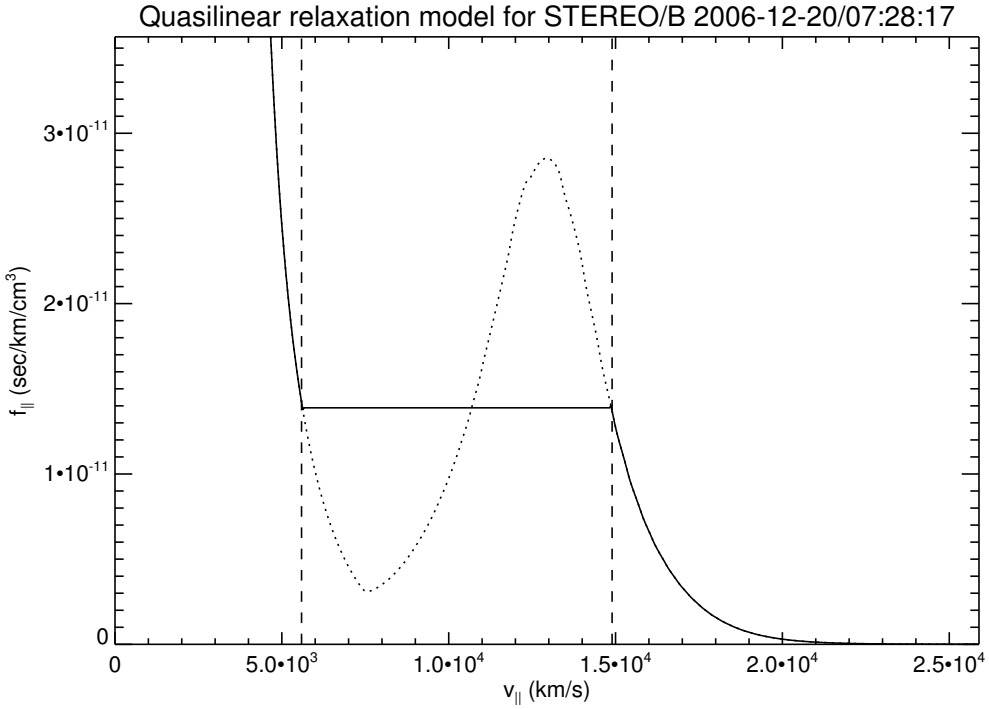

Figure 7.5: Quasi-linear relaxation model for foreshock distribution function observed by STEREO/Behind: 2006 Dec 20, 07:28 UT. The reduced $v_{\|}$ distribution function generated by the Fast Fermi acceleration process is plotted as a dotted line. The quasilinear relaxation process creates a flat plateau from the bump on tail beam. The distribution function after quasilinear flattening is plotted as a solid line. The region over which the flattening takes place can be used to parametrize the beam speed and width (see Figure 3.6), and is denoted by vertical dashed lines.

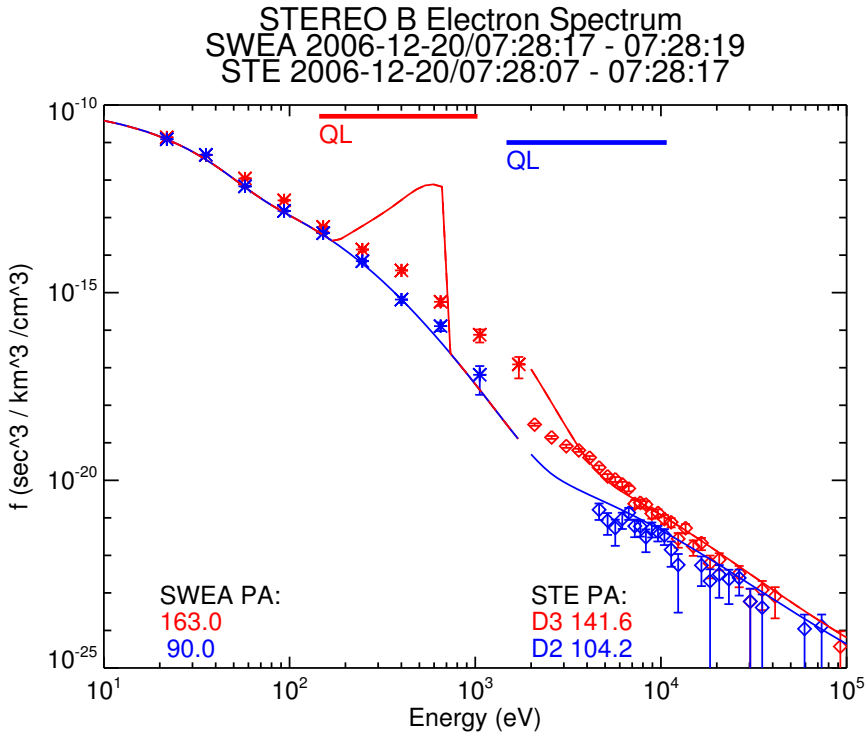

Figure 7.6: Foreshock electron spectrum observed by STEREO/Behind: 2006 Dec 20, 07:28 UT. The blue and red lines show Fast Fermi predictions (without taking quasilinear relaxation into account) for the perpendicular and parallel cuts through the electron distribution function (see Figure 7.4). The red and blue horizontal lines above the spectra show the range of energies over which the quasilinear relaxation affects each spectrum (see Figure 7.5).

7.3 Loss Cone Dynamics

The loss cone feature present in the foreshock electron distribution is a key signature of Fast Fermi acceleration. Evidence of measured loss cone distributions can be seen in Figure 5.3 and in simulations (Yuan et al. 2008). It is apparent from Figure 7.4 that the STE observations for Event 1 do not extend into the loss cone. Of all of the foreshock electron events observed by STE in late 2006, none offered a field of view made up entirely of the loss cone. However, the event on 2006 December 20 at approximately 07:30 UT (Event 2) offers a partial view into this depleted region at the highest STE energies.

Figures 7.7 and 7.8, which show an overview plot of Event 2 and the incident solar wind electron spectrum, correspond to Figures 7.2 and 7.3 for Event 1. The spacecraft position and magnetic field geometry are similar in both events. The fit parameters for the incident distribution are shown in Table 7.1. Similarly, Figures 7.9 and 7.10 show the results of the electron reflection process, and correspond to Figures 7.4 and 7.6. The Fast Fermi fit parameters for Event 2 are also listed in Table 7.1.

The individual electron spectrum analyzed from Event 2 shows accelerated electrons up to $\sim$ 50 keV. The electron spectrum from the detectors with nearly perpendicular pitch angles matches reasonably well with the predicted spectrum. The parallel electron spectrum (Figure 7.6) deviates from the model both above and below the quasilinear regime (as well as within the QL regime, where a match is not expected). Below, the rise in the parallel electrons begins at $\sim$ 100 eV, instead of $\sim$ 500 eV as predicted by the position of the quasilinearly relaxed beam. Above $\sim$ 40 keV, the measured electron spectrum begins to drop below the prediction. This may be a result of the fact that the STE bins at high energy are coming increasingly close to the boundary between reflected and transmitted electrons, and portions of the field of view may actually be in the loss cone (Figure 7.9).

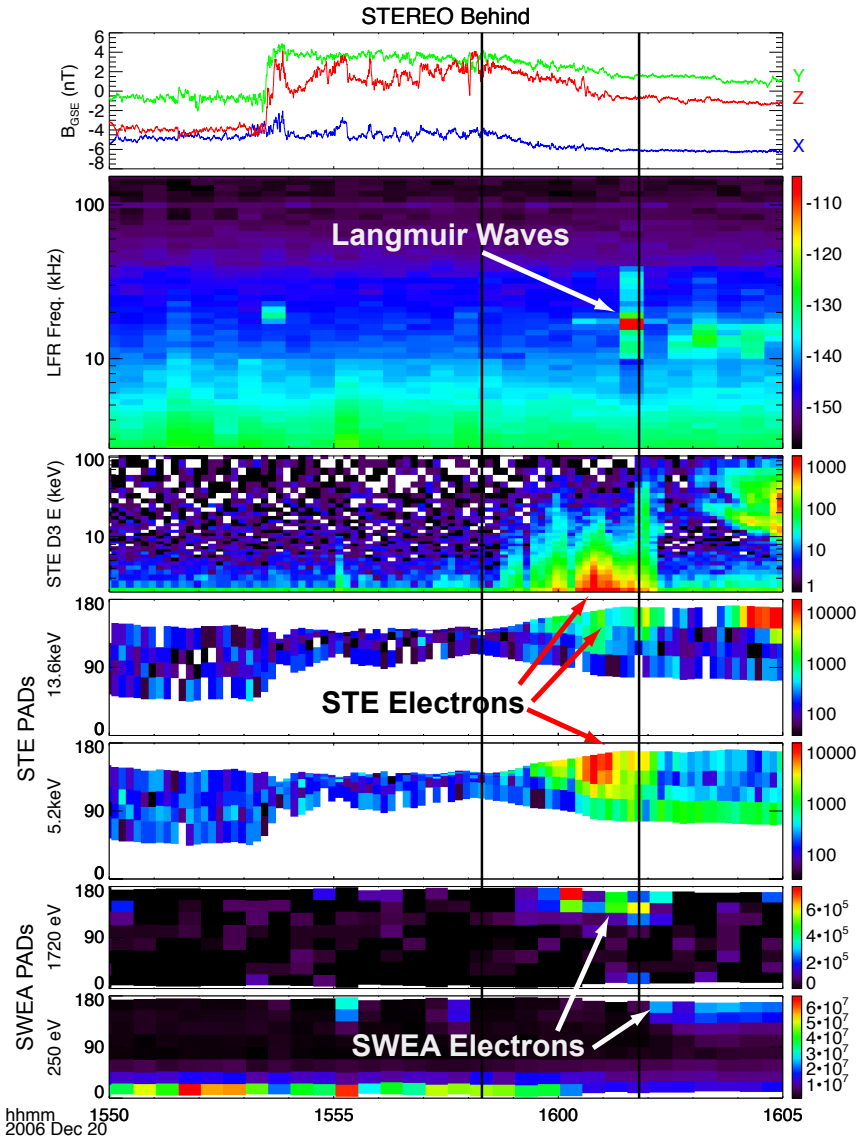

Figure 7.7: Upstream electron event observed by STEREO/Behind on 2006 December 20 at approximately 1600 UT. The plotted quantities are the same as those plotted in Figure 7.2.

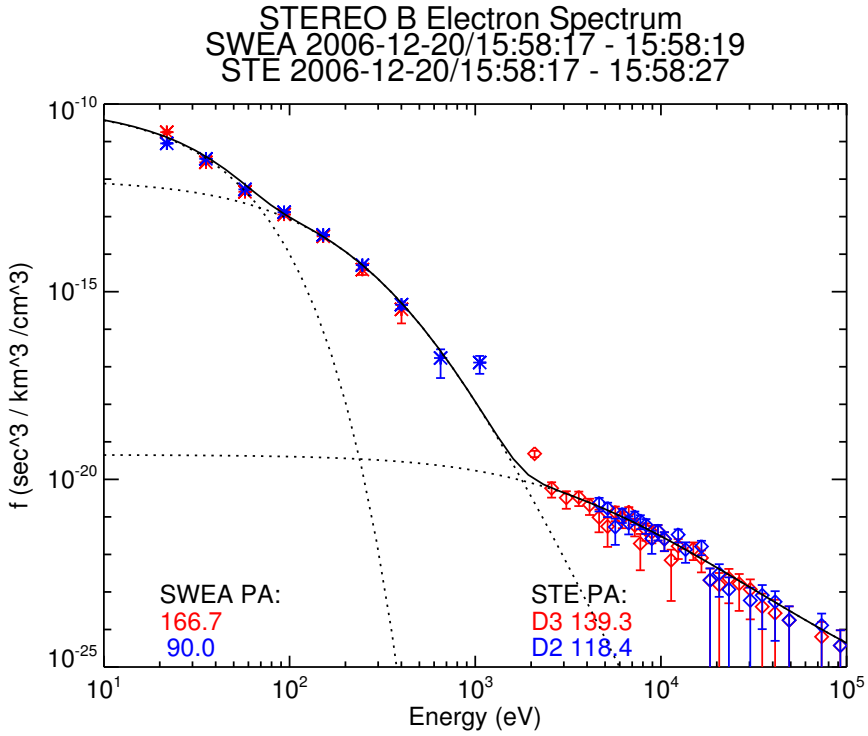

Figure 7.8: Incident electron spectrum observed by STEREO/Behind: 2006 Dec 20, 15:58 UT. See the caption of Figure 7.3 for plot description.

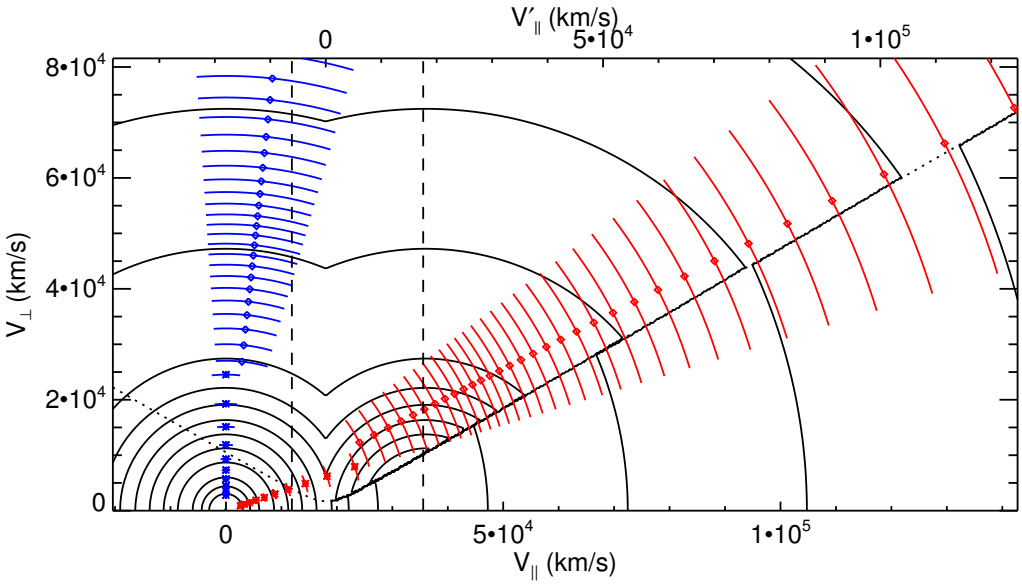

Figure 7.9: Fast Fermi parameters and location of pitch angle bins for STE and SWEA detectors in phase space, for the foreshock electron spectrum observed by STEREO/Behind: 2006 Dec 20, 16:01 UT. See the caption of Figure 7.4 for plot description. Note that in this plot, the field of view of the antiparallel STE detector extends into the loss cone.

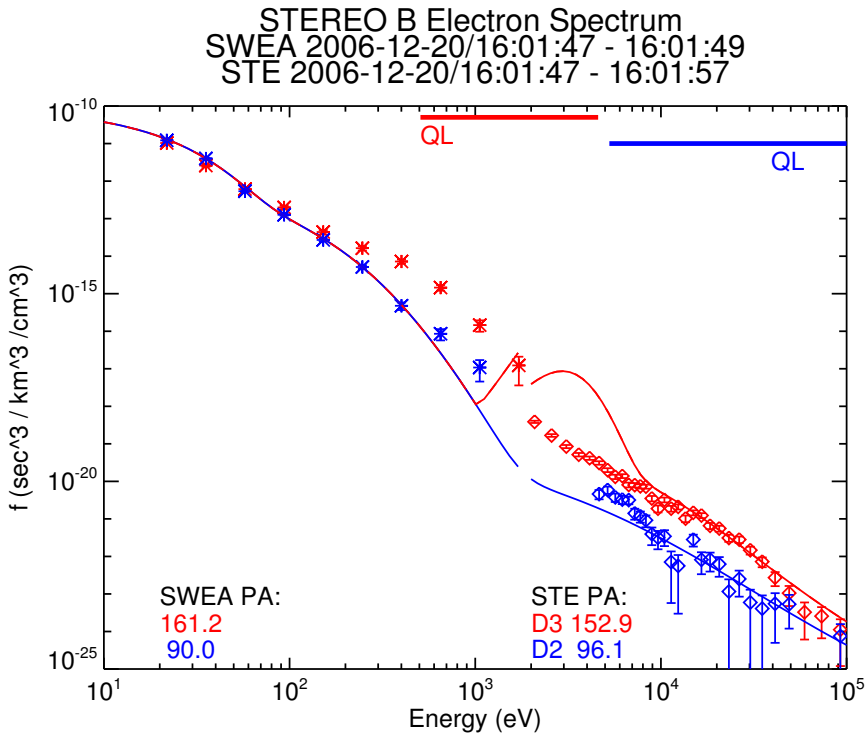

Figure 7.10: Foreshock electron spectrum observed by STEREO/Behind: 2006 Dec 20, 16:01 UT. See the caption of Figure 7.6 and the text for plot description.

7.4 Continuing Work with Foreshock Electron Beams

Analysis of Events 1 and 2 are in broad agreement with the theory of Fast Fermi acceleration. The observation that the high energy tail seen in Event 1 is consistent with the basic Fast Fermi mechanism is evidence that the theory may describe the reflected electron spectrum even if the adiabatic conservation condition that the electron Larmor radius remains much smaller than the scale size of the shock is violated. However, the results presented in this chapter are a work in progress. The next paragraphs describe various improvements which can be made to better analyze the foreshock electron beams.

First, the fit parameters for the incident distributions and the Fast Fermi parameters have been determined qualitatively by hand. Future work using statistical fitting procedures will be valuable particularly for the high energy range of the spectrum, enabling quantitative comparison of Fast Fermi predictions with the observed power law spectra.

Additional improvements to the fit and, therefore, to the comparison of the fit to the Fast Fermi prediction, will be obtained by a more realistic treatment of the pitch angle distributions. The current pitch angle spectra are plotted using a single value for the STE look direction, as shown in Figure 4.6. However, as can be seen in Figure 7.9, the field of view of a single STE bin is quite wide and samples portions of the distribution function with very different values of f. Integrating and normalizing over the STE field of view will yield a more accurate comparison of observed and measured spectra.

In addition to the beam produced directly by the Fast Fermi mechanism, kinematic time of flight effects (Filbert & Kellogg 1979; Cairns 1987; Kuncic et al. 2004) contribute to the generation of upstream bump on tail distributions via a time of flight velocity cutoff effect. We have not included this velocity cutoff in the present analysis, since (a) the Fast Fermi mechanism produces a significant bump on tail even in the absence of a velocity cutoff, and (b) it is difficult to establish the geometry of the shock interaction ($\theta_{\rm bn}$ and consequently $\mathbf{V}_{\rm HT}$) when the spacecraft is more than 100 $R_{\rm E}$ upstream of the bow shock and magnetic field motion (Zimbardo & Veltri 1996) limits the accuracy of field line projection back to the shock. It may be possible to use data from other spacecraft (for example, the Geotail spacecraft made a bow shock crossing on 2006 December 20 at approximately the same location as the source region for the observed STEREO electrons) or to use a long period of observed (via upstream electrons) connection with a stable magnetic field to investigate the relationship between depth in the foreshock and energy in the upstream electron beam.

The present analysis also ignores the beam dynamics in the region of quasilinear flattening, because the theory is based on a one-dimensional view of the reduced distribution function, while the measurements correspond to cuts through a two-dimensional function. Direct comparison of measured values with simulations of shock-accelerated electrons and comparison of nonlinear two-dimensional relaxation of electron beams (both are mentioned in the next chapter) will be useful points of comparison to the measured data.

Chapter 8

Summary and Future Work

8.1 Summary

Each result presented in this thesis underlines the complexity of electron acceleration and the importance of *in situ* measurements for the interpretation of remote observations. In this section, the key results from the three previous chapters are reviewed and connections with current related research are emphasized.

Chapter 5 discusses the importance of shock structure for the acceleration of electrons at interplanetary shocks. The scale sizes of these structures is on the order of several to tens of R_{E}. Recent observations using multispacecraft timing and Rankine-Hugoniot analysis of interplanetary shock crossings show that shocks also have nonplanar structure on spatial scales which are orders of magnitude larger than the foreshock regions (Neugebauer & Giacalone 2005; Koval & Szabo 2009). Simulations of shocks with shock front magnetic instabilities and upstream turbulence (Burgess 2006; Guo & Giacalone 2010) also reveal complex shock front structure. In this case, the structure is on the order of several ion inertial lengths (c/ω_{pi}), much smaller than the dimensions of the measured foreshock regions, and the rippling has significant effects on the acceleration of upstream electrons. It seems reasonable, from all of these observations, to expect that significant structure exists on IP shock fronts at all spatial scales from c/ω_{pi} up to the ~ 1 AU size of the shock itself.

The results of Chapter 6 show that a large number of factors play a role in generating shock accelerated electrons and Langmuir waves upstream of shocks. Although the most prominent role is played by $\mathbf{V}_{\mathrm{HT}}$, as is expected from Fast Fermi theory, the fact that many different but interdependent plasma parameters seem to have some association with upstream Langmuir wave activity again underscores the complexity of the phenomenon and the necessity of large numbers of events in order to examine a statistically significant sample of IP shocks. Simulations of electron beams and Langmuir wave growth (Kuncic

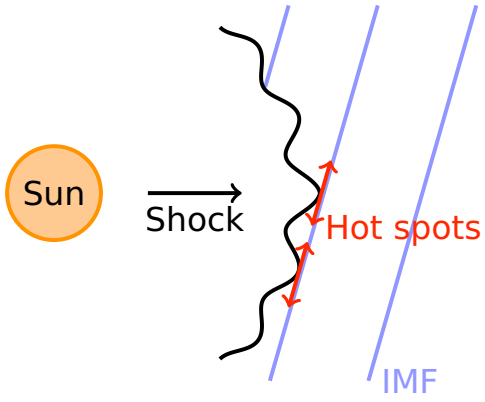

Figure 8.1: Cartoon CME-driven shock creating electron beams which lead to Type II generation. Electrons are not generated uniformly along the shock front but are accelerated in 'hot spots', IP foreshock regions defined by the locations of quasiperpendicular acceleration points. Chapters 5 and 6 describe measurements of these regions and show which shock conditions are statistically favorable for beam generation. Simulations (Burgess 2006; Guo & Giacalone 2010) show effects of shock structure on smaller scales.

et al. 2002; Knock et al. 2003; Li et al. 2003) offer a way to understand observations by quickly and systematically sampling the entirety of parameter space.

In Chapter 7, the microphysics of the electron distribution upstream of the shock is examined, using new instruments on the STEREO spacecraft, with greater sensitivity than had been previously available in the energy range corresponding to the electron superhalo. However, the limited angular resolution of the STEREO electron instruments implies that we cannot construct a reduced distribution function to directly compare observations to a one-dimensional quasilinear plateau. Two-dimensional simulations (Ziebell et al. 2008; Pavan et al. 2009) are necessary for comparison with the angled cuts through the distribution function that are available from the STEREO data.

8.2 Future Work

The final section of the previous chapter outlines the work to be completed for analysis of the upstream beams, and the previous section of this chapter outlined some direct connections to current theoretical and simulation areas of study. This final section briefly points the way towards several areas of future work.

In a broad sense, the process of electron acceleration and Langmuir wave emission plays a role in the overall picture of wave-particle interactions at collisionless shocks. Although the dynamics of a shock are dominated by ion motion, the results of Chapter 6 strongly suggest that internal shock structure plays an important role in electron

acceleration. Future work will examine this connection explicitly.

The STEREO/Ahead spacecraft spent the first several months of 2007 moving steadily farther away from the Earth, but remained intermittently connected to the electron foreshock, as shown by electron beams of terrestrial origin, for a distance of several hundred R_{E}. The dependence of the energy of the observed electron beams on the distance from the shock will be analyzed and compared to the observed dependence of Langmuir wave energy on distance (Malaspina et al. 2009).

The database of *Wind* IP shocks remains a fertile ground for analysis (Koval & Szabo 2008; Wilson et al. 2009), and will become more useful still as solar activity rises in the new solar cycle. Multispacecraft observations of shocks and Type II bursts combining *Wind* and STEREO observations will help fulfill the promise of the STEREO mission.

Bibliography

Abraham-Shrauner, B. 1972, J. Geophys. Res., 77, 736 [ADS] 17, 85

Acuña, M. H. 2002, Review of Scientific Instruments, 73, 3717 [ADS] 56

Acuña, M. H., Curtis, D., Scheifele, J. L., Russell, C. T., Schroeder, P., Szabo, A., & Luhmann, J. G. 2008, Space Science Reviews, 136, 203 [ADS] 56

Acuña, M. H., Ogilvie, K. W., Baker, D. N., Curtis, S. A., Fairfield, D. H., & Mish, W. H. 1995, Space Science Reviews, 71, 5 [ADS] 51

Amsler, C., *et al.* 2008, Phys. Lett. B, 667, 1 25

Anderson, K. A. 1968, J. Geophys. Res., 73, 2387 [ADS] 25, 80

Anderson, K. A., Lin, R. P., Martel, F., Lin, C. S., Parks, G. K., & Reme, H. 1979, Geophys. Res. Lett., 6, 401 [ADS] 62, 80, 98

Armstrong, T. P., Pesses, M. E., & Decker, R. B. 1985, Washington DC American Geophysical Union Geophysical Monograph Series, 35, 271 [ADS] 25, 27

Asbridge, J. R., Bame, S. J., & Strong, I. B. 1968, J. Geophys. Res., 73, 5777 [ADS] 25

Axford, W. I., Leer, E., & Skadron, G. 1977, in International Cosmic Ray Conference, Vol. 11, International Cosmic Ray Conference, 132–+ [ADS] 25

Bagenal, F. 2009, in Heliophysics: Plasma Physics of the Local Cosmos, ed. Schrijver, C. J. and Siscoe, G. L. (Cambridge University Press), 360–398 10, 11

Baker, J. L. 2005, in Effects of Space Weather on Technology Infrastructure, ed. I. A. Daglis (Springer), 1–25 5

Bale, S. D. 1997, J. Geophys. Res., 102, 19773 [ADS] 11

Bale, S. D., Kasper, J. C., Howes, G. G., Quataert, E., Salem, C., & Sundkvist, D. 2010, Physical Review Letters, submitted 4

Bale, S. D., Kellogg, P. J., Goetz, K., & Monson, S. J. 1998, Geophys. Res. Lett., 25, 9 [ADS] 43, 44

Bale, S. D., Kellogg, P. J., Mozer, F. S., Horbury, T. S., & Reme, H. 2005, Physical Review Letters, 94, 215002 [ADS] 3

Bale, S. D., Larson, D. E., Lin, R. P., Kellogg, P. J., Goetz, K., & Monson, S. J. 2000, J. Geophys. Res., 105, 27353 [ADS] 41, 42, 44

Bale, S. D. & Mozer, F. S. 2007, Physical Review Letters, 98, 205001 [ADS] 23

Bale, S. D., Mozer, F. S., & Horbury, T. S. 2003, Physical Review Letters, 91, 265004 [ADS] 24

Bale, S. D., Reiner, M. J., Bougeret, J., Kaiser, M. L., Krucker, S., Larson, D. E., & Lin, R. P. 1999, Geophys. Res. Lett., 26, 1573 [ADS] 62, 65, 71, 74, 81, 84, 86

Bale, S. D., Ullrich, R., Goetz, K., Alster, N., Cecconi, B., Dekkali, M., Lingner, N. R., Macher, W., Manning, R. E., McCauley, J., Monson, S. J., Oswald, T. H., & Pulupa, M. 2008, Space Science Reviews, 136, 529 [ADS] 55, 151, 152, 154

Ball, L. & Melrose, D. B. 2001, Publications of the Astronomical Society of Australia, 18, 361 [ADS] 27

Barth, J. L. 2005, in Effects of Space Weather on Technology Infrastructure, ed. I. A. Daglis (Springer), 123–145 5

Bell, A. R. 1978, MNRAS, 182, 147 [ADS] 25

Bellan, P. 2006, Fundamentals of Plasma Physics (Cambridge University Press) 34, 38, 46

Benson, R. F., Webb, P. A., Green, J. L., Carpenter, D. L., Sonwalkar, V. S., James, H. G., & Reinisch, B. W. 2006, in Lecture Notes in Physics, Berlin Springer Verlag, Vol. 687, Geospace Electromagnetic Waves and Radiation, ed. J. W. Labelle & R. A. Treumann, 3–+ [ADS] 43

Biermann, L. 1957, The Observatory, 77, 109 [ADS] 2

Blandford, R. D. & Ostriker, J. P. 1978, ApJ, 221, L29 [ADS] 25

Bohm, D. & Gross, E. P. 1949, Physical Review, 75, 1851 [ADS] 37

Bougeret, J., Kaiser, M. L., Kellogg, P. J., Manning, R., Goetz, K., Monson, S. J., Monge, N., Friel, L., Meetre, C. A., Perche, C., Sitruk, L., & Hoang, S. 1995, Space Science Reviews, 71, 231 [ADS] 54, 63, 81

Bougeret, J. L., Goetz, K., Kaiser, M. L., Bale, S. D., Kellogg, P. J., Maksimovic, M., Monge, N., Monson, S. J., Astier, P. L., Davy, S., Dekkali, M., Hinze, J. J., Manning, R. E., Aguilar-Rodriguez, E., Bonnin, X., Briand, C., Cairns, I. H., Cattell, C. A., Cecconi, B., Eastwood, J., Ergun, R. E., Fainberg, J., Hoang, S., Huttunen, K. E. J., Krucker, S., Lecacheux, A., MacDowall, R. J., Macher, W., Mangeney, A., Meetre, C. A., Moussas, X., Nguyen, Q. N., Oswald, T. H., Pulupa, M., Reiner, M. J., Robinson, P. A., Rucker, H., Salem, C., Santolik, O., Silvis, J. M., Ullrich, R., Zarka, P., & Zouganelis, I. 2008, Space Science Reviews, 136, 487 [ADS] 54

Büchner, J. & Elkina, N. 2005, Space Science Reviews, 121, 237 [ADS] 23

Burgess, D. 1995, in Introduction to Space Physics, ed. Kivelson, M. G. & Russell, C. T. (Cambridge University Press), 129–163 16, 17, 19

—. 2006, ApJ, 653, 316 [ADS] 89, 115, 116

Burlaga, L. F. 1971, Space Science Reviews, 12, 600 [ADS] 9

Burlaga, L. F., Ness, N. F., Acuña, M. H., Lepping, R. P., Connerney, J. E. P., & Richardson, J. D. 2008, Nature, 454, 75 [ADS] 11

Burlaga, L. F., Ness, N. F., Acuña, M. H., Lepping, R. P., Connerney, J. E. P., Stone, E. C., & McDonald, F. B. 2005, Science, 309, 2027 [ADS] 11

Cairns, I. H. 1986, Proceedings of the Astronomical Society of Australia, 6, 444 [ADS] 62

—. 1987, J. Geophys. Res., 92, 2315 [ADS] 113

Cairns, I. H., Knock, S. A., Robinson, P. A., & Kuncic, Z. 2003, Space Science Reviews, 107, 27 [ADS] 62

Cairns, I. H. & Robinson, P. A. 1999, Physical Review Letters, 82, 3066 [ADS] 41

Cairns, I. H., Robinson, P. A., & Smith, N. I. 1998, J. Geophys. Res., 103, 287 [ADS] 43

Cairns, I. H., Robinson, P. A., & Zank, G. P. 2000, Publications of the Astronomical Society of Australia, 17, 22 [ADS] 41, 84

Cane, H. V. & Richardson, I. G. 2003, Journal of Geophysical Research (Space Physics), 108, 1156 [ADS] 65

Cane, H. V., Sheeley, Jr., N. R., & Howard, R. A. 1987, J. Geophys. Res., 92, 9869 [ADS] 4, 10, 80, 89

Cane, H. V., Stone, R. G., Fainberg, J., Steinberg, J. L., & Hoang, S. 1982, Sol. Phys., 78, 187 [ADS] 80

Cane, H. V., Stone, R. G., Fainberg, J., Steinberg, J. L., Hoang, S., & Stewart, R. T. 1981, Geophys. Res. Lett., 8, 1285 [ADS] 80

Carrington, R. C. 1859, MNRAS, 20, 13 [ADS] 4

Cecconi, B., Bonnin, X., Hoang, S., Maksimovic, M., Bale, S. D., Bougeret, J., Goetz, K., Lecacheux, A., Reiner, M. J., Rucker, H. O., & Zarka, P. 2008, Space Science Reviews, 136, 549 [ADS] 45

Cecconi, B. & Zarka, P. 2005, Radio Science, 40, 3003 [ADS] 55, 154

Cerruti, A. P., Kintner, P. M., Gary, D. E., Mannucci, A. J., Meyer, R. F., Doherty, P., & Coster, A. J. 2008, Space Weather, 6, 10 [ADS] 5

Chandran, B. D. G. & Hollweg, J. V. 2009, ApJ, 707, 1659 [ADS] 3

Chao, J. K. & Lepping, R. P. 1974, J. Geophys. Res., 79, 1799 [ADS] 9

Chao, J. K., Lyu, L. H., Wu, B. H., Lazarus, A. J., Chang, T. S., & Lepping, R. P. 1993, J. Geophys. Res., 98, 17443 [ADS] 19

Chao, J. K. & Olbert, S. 1970, J. Geophys. Res., 75, 6394 [ADS] 19

Chapman, S. & Zirin, H. 1957, Smithsonian Contributions to Astrophysics, 2, 1 [ADS] 2

Chen, F. F. 2006, Introduction to Plasma Physics and Controlled Fusion (Springer) 38

Cliver, E. W. & Svalgaard, L. 2004, Sol. Phys., 224, 407 [ADS] 5

Committee On The Societal and Economic Impacts Of Severe Space Weather Events. 2008, Understanding Societal and Economic Impacts: A Workshop Report, Tech. rep., National Academies Press [ADS] 4

Couturier, P., Hoang, S., Meyer-Vernet, N., & Steinberg, J. L. 1981, J. Geophys. Res., 86, 11127 [ADS] 45

Cranmer, S. R., Matthaeus, W. H., Breech, B. A., & Kasper, J. C. 2009, ApJ, 702, 1604 [ADS] 23

Cravens, T. E. & Gombosi, T. I. 2004, Advances in Space Research, 33, 1968 [ADS] 11

Cremades, H., St. Cyr, O. C., & Kaiser, M. L. 2007, Space Weather, 5, 8001 [ADS] 80

CYRO Industries. 2002, Physical Properties of Acrylite GP 142

de Hoffmann, F. & Teller, E. 1950, Physical Review, 80, 692 [ADS] 35

De Pontieu, B., McIntosh, S. W., Carlsson, M., Hansteen, V. H., Tarbell, T. D., Schrijver, C. J., Title, A. M., Shine, R. A., Tsuneta, S., Katsukawa, Y., Ichimoto, K., Suematsu, Y., Shimizu, T., & Nagata, S. 2007, Science, 318, 1574 [ADS] 3

Decker, R. B. 1988, ApJ, 324, 566 [ADS] 28

—. 1990, J. Geophys. Res., 95, 11993 [ADS] 26, 76

Decker, R. B. 1992, in American Institute of Physics Conference Series, Vol. 264, Particle Acceleration in Cosmic Plasmas, ed. G. P. Zank & T. K. Gaisser, 183–188 [ADS] 25

Decker, R. B., Krimigis, S. M., Roelof, E. C., Hill, M. E., Armstrong, T. P., Gloeckler, G., Hamilton, D. C., & Lanzerotti, L. J. 2005, Science, 309, 2020 [ADS] 11

Dmitriev, A. V. & Yeh, H. 2008, Journal of Atmospheric and Solar-Terrestrial Physics, 70, 1971 [ADS] 4

Draine, B. T. & McKee, C. F. 1993, ARA&A, 31, 373 [ADS] 14, 17

Drake, F. H., Pierce, G. W., & Dow, M. T. 1930, Physical Review, 35, 613 [ADS] 142

Driesman, A., Hynes, S., & Cancro, G. 2008, Space Science Reviews, 136, 17 [ADS] 53, 144

Dulk, G. A. 1985, ARA&A, 23, 169 [ADS] 29

Eastwood, J. P., Lucek, E. A., Mazelle, C., Meziane, K., Narita, Y., Pickett, J., & Treumann, R. A. 2005, Space Science Reviews, 118, 41 [ADS] 98

Eastwood, J. P., Wheatland, M. S., Hudson, H. S., Krucker, S., Bale, S. D., Maksimovic, M., Goetz, K., & Bougeret, J. 2010, ApJ, 708, L95 [ADS] 98

Edlén, B. 1945, MNRAS, 105, 323 [ADS] 2

Edmiston, J. P. & Kennel, C. F. 1984, Journal of Plasma Physics, 32, 429 [ADS] 89

Edmondson, J. K., Lynch, B. J., Antiochos, S. K., De Vore, C. R., & Zurbuchen, T. H. 2009, ApJ, 707, 1427 [ADS] 3

Egeland, A. & Burke, W. J., eds. 2005, Astrophysics and Space Science Library, Vol. 325, Kristian Birkeland, The First Space Scientist [ADS] 2

Ellison, D. C. 1985, J. Geophys. Res., 90, 29 [ADS] 25

Ellison, W. J., Lamkaouchi, K., & Moreau, J. L. 1996, Journal of Molecular Liquids, 68, 171 142

Erdos, G. & Balogh, A. 1994, ApJS, 90, 553 [ADS] 26, 76

Ergun, R. E., Larson, D., Lin, R. P., McFadden, J. P., Carlson, C. W., Anderson, K. A., Muschietti, L., McCarthy, M., Parks, G. K., Reme, H., Bosqued, J. M., D'Uston, C., Sanderson, T. R., Wenzel, K. P., Kaiser, M., Lepping, R. P., Bale, S. D., Kellogg, P., & Bougeret, J. 1998, ApJ, 503, 435 [ADS] 41

Ergun, R. E., Malaspina, D. M., Cairns, I. H., Goldman, M. V., Newman, D. L., Robinson, P. A., Eriksson, S., Bougeret, J. L., Briand, C., Bale, S. D., Cattell, C. A., Kellogg, P. J., & Kaiser, M. L. 2008, Physical Review Letters, 101, 051101 [ADS] 43

Fejer, J. A. & Kan, J. R. 1969, Radio Science, 4, 721 [ADS] 45

Feldman, W. C., Anderson, R. C., Bame, S. J., Gary, S. P., Gosling, J. T., McComas, D. J., Thomsen, M. F., Paschmann, G., & Hoppe, M. M. 1983, J. Geophys. Res., 88, 96 [ADS] 80

Feldman, W. C., Asbridge, J. R., Bame, S. J., Montgomery, M. D., & Gary, S. P. 1975, J. Geophys. Res., 80, 4181 [ADS] 32, 33, 89, 90, 94

Feng, H. & Wang, J. M. 2008, Sol. Phys., 247, 195 [ADS] 19

Fermi, E. 1949, Physical Review, 75, 1169 [ADS] 25

—. 1954, ApJ, 119, 1 [ADS] 25

Filbert, P. C. & Kellogg, P. J. 1979, J. Geophys. Res., 84, 1369 [ADS] 41, 62, 66, 74, 80, 98, 113

Fisk, L. A. 1971, J. Geophys. Res., 76, 1662 [ADS] 25

Fitzenreiter, R. J. 1995, Advances in Space Research, 15, 9 [ADS] 98

Fitzenreiter, R. J., Klimas, A. J., & Scudder, J. D. 1984, Geophys. Res. Lett., 11, 496 [ADS] 41, 62, 66

Fitzenreiter, R. J., Ogilvie, K. W., Bale, S. D., & Viñas, A. F. 2003, Journal of Geophysical Research (Space Physics), 108, 1415 [ADS] 67, 81, 89

Fitzenreiter, R. J., Viňas, A. F., Klimas, A. J., Lepping, R. P., Kaiser, M. L., & Onsager, T. G. 1996, Geophys. Res. Lett., 23, 1235 [ADS] 41, 62, 67

Foroutan, G., Khalilpour, H., Moslehi-Fard, M., Li, B., & Robinson, P. A. 2008, Physics of Plasmas, 15, 122904 [ADS] 41

Friedrichs, K. O. & Kranzer, H. 1958, in Report No. NYO-6486 (AEC Computing and Applied Mathematics Center, Institute of Mathematical Sciences, New York University), 1–61 17

Giacalone, J. 1992, J. Geophys. Res., 97, 8307 [ADS] 26

Ginzburg, V. L. & Zhelezniakov, V. V. 1959, in IAU Symposium, Vol. 9, URSI Symp. 1: Paris Symposium on Radio Astronomy, ed. R. N. Bracewell, 574–+ [ADS] 43

Goldreich, P. & Sridhar, S. 1995, ApJ, 438, 763 [ADS] 3

Gonzalez, W. D., Joselyn, J. A., Kamide, Y., Kroehl, H. W., Rostoker, G., Tsurutani, B. T., & Vasyliunas, V. M. 1994, J. Geophys. Res., 99, 5771 [ADS] 4

Goodrich, C. C. & Scudder, J. D. 1984, J. Geophys. Res., 89, 6654 [ADS] 21, 82

Gopalswamy, N., Aguilar-Rodriguez, E., Yashiro, S., Nunes, S., Kaiser, M. L., & Howard, R. A. 2005, Journal of Geophysical Research (Space Physics), 110, 12 [ADS] 10, 89

Gopalswamy, N., Xie, H., Mäkelä, P., Akiyama, S., Yashiro, S., Kaiser, M. L., Howard, R. A., & Bougeret, J. 2010, ApJ, 710, 1111 [ADS] 10

Gopalswamy, N., Yashiro, S., & Akiyama, S. 2007, Journal of Geophysical Research (Space Physics), 112, 6112 [ADS] 4

Gopalswamy, N., Yashiro, S., Akiyama, S., Mäkelä, P., Xie, H., Kaiser, M. L., Howard, R. A., & Bougeret, J. L. 2008, Annales Geophysicae, 26, 3033 [ADS] 10

Gosling, J. T. 1993, J. Geophys. Res., 98, 18937 [ADS] 4

Gosling, J. T., Asbridge, J. R., Bame, S. J., Feldman, W. C., Zwickl, R. D., Paschmann, G., Sckopke, N., & Hynds, R. J. 1981, J. Geophys. Res., 86, 547 [ADS] 25

Gosling, J. T., Hansen, R. T., & Bame, S. J. 1971, J. Geophys. Res., 76, 1811 [ADS] 19

Gosling, J. T., Hildner, E., MacQueen, R. M., Munro, R. H., Poland, A. I., & Ross, C. L. 1974, J. Geophys. Res., 79, 4581 [ADS] 4

Gosling, J. T. & Pizzo, V. J. 1999, Space Science Reviews, 89, 21 [ADS] 10

Greenstadt, E. W. 1985, in Collisionless Shocks in the Heliosphere: Reviews of Current Research, ed. Tsurutani, B. T. and Stone, R. G. (AGU Geophysical Monograph 35), 169–184 19

Grognard, R. 1975, Australian Journal of Physics, 28, 731 [ADS] 41

Guo, F. & Giacalone, J. 2010, ArXiv e-prints [ADS] 115, 116

Gurnett, D. A., Neubauer, F. M., & Schwenn, R. 1979, J. Geophys. Res., 84, 541 [ADS] 80

Hansteen, V. H. 2009, in Heliophysics: Plasma Physics of the Local Cosmos, ed. Schrijver, C. J. and Siscoe, G. L. (Cambridge University Press), 225–255 3, 10

Harten, R. & Clark, K. 1995, Space Science Reviews, 71, 23 [ADS] 52

Hector, L. G. & Schultz, H. L. 1936, Journal of Applied Physics, 7, 133 142

Hellinger, P., Trávnícek, P., & Matsumoto, H. 2002, Geophys. Res. Lett., 29, 240000 [ADS] 76, 89

Hellinger, P., Trávníček, P., Kasper, J. C., & Lazarus, A. J. 2006, Geophys. Res. Lett., 33, 9101 [ADS] 4

Hellinger, P., Trávníček, P., Lembège, B., & Savoini, P. 2007, Geophys. Res. Lett., 34, 14109 [ADS] 76

Hinkel-Lipsker, D. E., Fried, B. D., & Morales, G. J. 1992, Physics of Fluids B, 4, 559 [ADS] 44

Hoang, S. 1972, Dép. de Rech. Spaciale Rapport PYR/1105, obs. de Paris, Meudon 151

Hoang, S., Maksimovic, M., Bougeret, J., Reiner, M. J., & Kaiser, M. L. 1998, Geophys. Res. Lett., 25, 2497 [ADS] 80

Howard, R. A., Moses, J. D., Vourlidas, A., Newmark, J. S., Socker, D. G., Plunkett, S. P., Korendyke, C. M., Cook, J. W., Hurley, A., Davila, J. M., Thompson, W. T., St Cyr, O. C., Mentzell, E., Mehalick, K., Lemen, J. R., Wuelser, J. P., Duncan, D. W., Tarbell, T. D., Wolfson, C. J., Moore, A., Harrison, R. A., Waltham, N. R., Lang, J., Davis, C. J., Eyles, C. J., Mapson-Menard, H., Simnett, G. M., Halain, J. P., Defise, J. M., Mazy, E., Rochus, P., Mercier, R., Ravet, M. F., Delmotte, F., Auchere, F., Delaboudiniere, J. P., Bothmer, V., Deutsch, W., Wang, D., Rich, N., Cooper, S., Stephens, V., Maahs, G., Baugh, R., McMullin, D., & Carter, T. 2008, Space Science Reviews, 136, 67 [ADS] 54

Hsieh, K. C., Frisch, P. C., Giacalone, J., Jokipii, J. R., Kóta, J., Larson, D. E., Lin, R. P., Luhmann, J. G., & Wang, L. 2009, ApJ, 694, L79 [ADS] 59

Huba, J. D. 2004, NRL Plasma Formulary, Published by the Naval Research Laboratory 155

Hudson, H., Haisch, B., & Strong, K. T. 1995, J. Geophys. Res., 100, 3473 [ADS] 4

Hufbauer, K. 1991, Exploring the sun: solar science since Galileo (Johns Hopkins University Press) 4

Hulin, R. & Epstein, G. 1973, Dép. de Rech. Spaciale Rapport 103/PYR/9, obs. de Paris, Meudon 151

Hull, A. J., Scudder, J. D., Fitzenreiter, R. J., Ogilvie, K. W., Newbury, J. A., & Russell, C. T. 2000, J. Geophys. Res., 105, 20957 [ADS] 89

Hundhausen, A. J. 1995, in Introduction to Space Physics, ed. Kivelson, M. G. & Russell, C. T. (Cambridge University Press), 91–128 33

Issautier, K., Meyer-Vernet, N., Moncuquet, M., Hoang, S., & McComas, D. J. 1999, J. Geophys. Res., 104, 6691 [ADS] 46, 48

Issautier, K., Moncuquet, M., & Hoang, S. 2003, in American Institute of Physics Conference Series, Vol. 679, Solar Wind Ten, ed. M. Velli, R. Bruno, F. Malara, & B. Bucci, 59–62 [ADS] 33

Issautier, K., Perche, C., Hoang, S., Lacombe, C., Maksimovic, M., Bougeret, J., & Salem, C. 2005, Advances in Space Research, 35, 2141 [ADS] 46

Jian, L., Russell, C. T., Luhmann, J. G., & Skoug, R. M. 2006, Sol. Phys., 239, 337 [ADS] 10

Jones, F. C. & Ellison, D. C. 1991, Space Science Reviews, 58, 259 [ADS] 25

Kantrowitz, A. R. & Petschek, H. E. 1966, in Plasma Physics in Theory and Application, ed. Kunkel, W. B. (McGraw-Hill), 147 12, 15

Kappenman, J. G., Radasky, W. A., Gilbert, J. L., & Erinmez, L. A. 2000, IEEE Transactions on Plasma Science, 28, 2114 [ADS] 5

Kasper, J. C., Lazarus, A. J., Steinberg, J. T., Ogilvie, K. W., & Szabo, A. 2006, Journal of Geophysical Research (Space Physics), 111, 3105 [ADS] 84

Kasper, J. C., Maruca, B. A., & Bale, S. D. 2010, Physical Review Letters, submitted 4

Kellogg, P. J. 1962, J. Geophys. Res., 67, 3805 [ADS] 9

—. 2003, Planet. Space Sci., 51, 681 [ADS] 41

Kellogg, P. J., Goetz, K., Monson, S. J., & Bale, S. D. 1999a, J. Geophys. Res., 104, 6751 [ADS] 43

—. 1999b, J. Geophys. Res., 104, 17069 [ADS] 42

Kellogg, P. J., Goetz, K., Monson, S. J., Bougeret, J., Manning, R., & Kaiser, M. L. 1996, Geophys. Res. Lett., 23, 1267 [ADS] 11

Kim, E., Cairns, I. H., & Robinson, P. A. 2008, Physics of Plasmas, 15, 102110 [ADS] 44

Kintner, P. M. & Ledvina, B. M. 2005, Advances in Space Research, 35, 788 [ADS] 5

Klimchuk, J. A. 2006, Sol. Phys., 234, 41 [ADS] 3

Knock, S. A., Cairns, I. H., Robinson, P. A., & Kuncic, Z. 2001, J. Geophys. Res., 106, 25041 [ADS] 62, 84

—. 2003, Journal of Geophysical Research (Space Physics), 108, 1126 [ADS] 62, 84, 96, 116

Koval, A. & Szabo, A. 2008, Journal of Geophysical Research (Space Physics), 113, 10110 [ADS] 117

—. 2009, AGU Fall Meeting Abstracts, A1471+ [ADS] 115

Krauss-Varban, D. & Burgess, D. 1991, J. Geophys. Res., 96, 143 [ADS] 62, 84

Krauss-Varban, D., Burgess, D., & Wu, C. S. 1989, J. Geophys. Res., 94, 15089 [ADS] 36, 37, 62, 83

Krauss-Varban, D. & Wu, C. S. 1989, J. Geophys. Res., 94, 15367 [ADS] 35

Kuncic, Z., Cairns, I. H., Knock, S., & Robinson, P. A. 2002, Geophys. Res. Lett., 29, 080000 [ADS] 115

Kuncic, Z., Cairns, I. H., & Knock, S. A. 2004, Journal of Geophysical Research (Space Physics), 109, 2108 [ADS] 113

Ladreiter, H. P., Zarka, P., & Lacacheux, A. 1994, Planet. Space Sci., 42, 919 [ADS] 45

Landau, L. D. 1946, J. Physics (USSR), 10, 25 38

Larson, D. E., Lin, R. P., McFadden, J. P., Ergun, R. E., Carlson, C. W., Anderson, K. A., Phan, T. D., McCarthy, M. P., Parks, G. K., Rème, H., Bosqued, J. M., d'Uston, C., Sanderson, T. R., Wenzel, K., & Lepping, R. P. 1996, Geophys. Res. Lett., 23, 2203 [ADS] 62, 66, 82

Lecacheux, A. 1978, A&A, 70, 701 [ADS] 45

Lee, M. A. 2000, in American Institute of Physics Conference Series, Vol. 528, Acceleration and Transport of Energetic Particles Observed in the Heliosphere, ed. R. A. Mewaldt, J. R. Jokipii, M. A. Lee, E. Möbius, & T. H. Zurbuchen , 3–18 [ADS] 25, 26

Lee, M. A. & Fisk, L. A. 1982, Space Science Reviews, 32, 205 [ADS] 25

Lepping, R. P., Acũna, M. H., Burlaga, L. F., Farrell, W. M., Slavin, J. A., Schatten, K. H., Mariani, F., Ness, N. F., Neubauer, F. M., Whang, Y. C., Byrnes, J. B., Kennon, R. S., Panetta, P. V., Scheifele, J., & Worley, E. M. 1995, Space Science Reviews, 71, 207 [ADS] 56, 65, 84

Leroy, M. M. & Mangeney, A. 1984, Annales Geophysicae, 2, 449 [ADS] 35, 62, 66, 82, 83

Li, B., Willes, A. J., Robinson, P. A., & Cairns, I. H. 2003, Physics of Plasmas, 10, 2748 [ADS] 116

Lin, R. P. 1998, Space Science Reviews, 86, 61 [ADS] 33

—. 2005, Advances in Space Research, 35, 1857 [ADS] 39

Lin, R. P., Anderson, K. A., Ashford, S., Carlson, C., Curtis, D., Ergun, R., Larson, D., McFadden, J., McCarthy, M., Parks, G. K., Rème, H., Bosqued, J. M., Coutelier, J., Cotin, F., D'Uston, C., Wenzel, K., Sanderson, T. R., Henrion, J., Ronnet, J. C., & Paschmann, G. 1995, Space Science Reviews, 71, 125 [ADS] 57, 58, 64, 86

Lin, R. P., Curtis, D. W., Larson, D. E., Luhmann, J. G., McBride, S. E., Maier, M. R., Moreau, T., Tindall, C. S., Turin, P., & Wang, L. 2008, Space Science Reviews, 136, 241 [ADS] 58

Lin, R. P., Larson, D., McFadden, J., Carlson, C. W., Ergun, R. E., Anderson, K. A., Ashford, S., McCarthy, M., Parks, G. K., Rème, H., Bosqued, J. M., d'Uston, C., Sanderson, T. R., & Wenzel, K. P. 1996, Geophys. Res. Lett., 23, 1211 [ADS] 33

Lin, R. P., Levedahl, W. K., Lotko, W., Gurnett, D. A., & Scarf, F. L. 1986, ApJ, 308, 954 [ADS] 41

Lin, R. P., Potter, D. W., Gurnett, D. A., & Scarf, F. L. 1981, ApJ, 251, 364 [ADS] 41

Liu, Y., Richardson, J. D., Belcher, J. W., Kasper, J. C., & Elliott, H. A. 2006, Journal of Geophysical Research (Space Physics), 111, 1102 [ADS] 4

Livadiotis, G. & McComas, D. J. 2009, Journal of Geophysical Research (Space Physics), 114, 11105 [ADS] 32

Livi, S., Marsch, E., & Rosenbauer, H. 1986, J. Geophys. Res., 91, 8045 [ADS] 9

Luhmann, J. G. 1986, Space Science Reviews, 44, 241 [ADS] 11

Macher, W., Oswald, T. H., Fischer, G., & Rucker, H. O. 2007, Measurement Science and Technology, 18, 3731 154

MacQueen, R. M., Eddy, J. A., Gosling, J. T., Hildner, E., Munro, R. H., Newkirk, Jr., G. A., Poland, A. I., & Ross, C. L. 1974, ApJ, 187, L85+ [ADS] 4

Maksimovic, M., Hoang, S., Meyer-Vernet, N., Moncuquet, M., Bougeret, J., Phillips, J. L., & Canu, P. 1995, J. Geophys. Res., 100, 19881 [ADS] 46, 48

Maksimovic, M., Zouganelis, I., Chaufray, J., Issautier, K., Scime, E. E., Littleton, J. E., Marsch, E., McComas, D. J., Salem, C., Lin, R. P., & Elliott, H. 2005, Journal of Geophysical Research (Space Physics), 110, 9104 [ADS] 32, 33

Malaspina, D. M., Cairns, I. H., & Ergun, R. E. 2010, Journal of Geophysical Research (Space Physics), 115, 1101 [ADS] 44, 45

Malaspina, D. M. & Ergun, R. E. 2008, Journal of Geophysical Research (Space Physics), 113, 12108 [ADS] 43

Malaspina, D. M., Li, B., Cairns, I. H., Robinson, P. A., Kuncic, Z., & Ergun, R. E. 2009, Journal of Geophysical Research (Space Physics), 114, 12101 [ADS] 98, 117

Malmberg, J. H. & Wharton, C. B. 1964, Physical Review Letters, 13, 184 [ADS] 39

Manning, R. 2000, in Radio Astronomy at Long Wavelengths, ed. Stone, R. G. and Weiler, K. W. and Goldstein, M. L. and Bougeret, J. L. (AGU Geophysical Monograph 119), 329–337 154

Manoharan, P. K., Gopalswamy, N., Yashiro, S., Lara, A., Michalek, G., & Howard, R. A. 2004, Journal of Geophysical Research (Space Physics), 109, 6109 [ADS] 65

Mazelle, C., Winterhalter, D., Sauer, K., Trotignon, J. G., Acuña, M. H., Baumgärtel, K., Bertucci, C., Brain, D. A., Brecht, S. H., Delva, M., Dubinin, E., Øieroset, M., & Slavin, J. 2004, Space Science Reviews, 111, 115 [ADS] 11

McComas, D. J., Elliott, H. A., Schwadron, N. A., Gosling, J. T., Skoug, R. M., & Goldstein, B. E. 2003, Geophys. Res. Lett., 30, 100000 [ADS] 3

Melrose, D. B. 1986, Instabilities in space and laboratory plasmas (Cambridge University Press) 41, 43

Meyer-Vernet, N. 1979, J. Geophys. Res., 84, 5373 [ADS] 45

Meyer-Vernet, N. & Perche, C. 1989, J. Geophys. Res., 94, 2405 [ADS] 45, 46, 48, 85

Meziane, K., Hull, A. J., Hamza, A. M., & Lin, R. P. 2002, Journal of Geophysical Research (Space Physics), 107, 1243 [ADS] 26

Montgomery, M. D., Bame, S. J., & Hundhausen, A. J. 1968, J. Geophys. Res., 73, 4999 [ADS] 33

Mullan, D. J. & Smith, C. W. 2006, Sol. Phys., 234, 325 [ADS] 19

Ness, N. F., Scearce, C. S., & Seek, J. B. 1964, J. Geophys. Res., 69, 3531 [ADS] 9

Neugebauer, M. & Giacalone, J. 2005, Journal of Geophysical Research (Space Physics), 110, 12106 [ADS] 115

Neugebauer, M. & Snyder, C. W. 1962, Science, 138, 1095 [ADS] 2, 19

—. 1966, J. Geophys. Res., 71, 4469 [ADS] 2

Ogilvie, K. W., Chornay, D. J., Fritzenreiter, R. J., Hunsaker, F., Keller, J., Lobell, J., Miller, G., Scudder, J. D., Sittler, Jr., E. C., Torbert, R. B., Bodet, D., Needell, G., Lazarus, A. J., Steinberg, J. T., Tappan, J. H., Mavretic, A., & Gergin, E. 1995, Space Science Reviews, 71, 55 [ADS] 67, 84

Oswald, T. H., Macher, W., Rucker, H. O., Fischer, G., Taubenschuss, U., Bougeret, J. L., Lecacheux, A., Kaiser, M. L., & Goetz, K. 2009, Advances in Space Research, 43, 355 [ADS] 138, 153

Panchenko, M. 2009, presentation at the Fall 2009 S/WAVES Team Meeting 154

Papadopoulos, K. 1985, in Collisionless Shocks in the Heliosphere: A Tutorial Review, ed. Stone, R. G. and Tsurutani, B. T. (AGU Geophysical Monograph 34), 59–90 9

Parker, E. N. 1958a, Physical Review, 109, 1874 [ADS] 2

—. 1958b, ApJ, 128, 664 [ADS] 2

—. 1958c, Physical Review, 109, 1328 [ADS] 25

—. 1965, Space Science Reviews, 4, 666 [ADS] 2

Parks, G. K. 2004, Space Science Reviews, 113, 97 [ADS] 21

Paschmann, G. & Schwartz, S. J. 2000, in ESA Special Publication, Vol. 449, Cluster-II Workshop Multiscale / Multipoint Plasma Measurements, ed. R. A. Harris, 99–+ [ADS] 17, 71, 75

Patsourakos, S. & Vourlidas, A. 2009, ApJ, 700, L182 [ADS] 54

Pavan, J., Ziebell, L. F., Gaelzer, R., & Yoon, P. H. 2009, Journal of Geophysical Research (Space Physics), 114, 1106 [ADS] 116

Phan, T. D., Gosling, J. T., & Davis, M. S. 2009, Geophys. Res. Lett., 36, 9108 [ADS] 3

Phan, T. D., Gosling, J. T., Davis, M. S., Skoug, R. M., Øieroset, M., Lin, R. P., Lepping, R. P., McComas, D. J., Smith, C. W., Reme, H., & Balogh, A. 2006, Nature, 439, 175 [ADS] 3

Pilipp, W. G., Muehlhaeuser, K., Miggenrieder, H., Montgomery, M. D., & Rosenbauer, H. 1987, J. Geophys. Res., 92, 1075 [ADS] 32, 33

Pirjola, R., Viljanen, A., Pulkkinen, A., & Amm, O. 2000, Physics and Chemistry of the Earth C, 25, 333 [ADS] 5

Pizzo, V. 1978, J. Geophys. Res., 83, 5563 [ADS] 10

Podesta, J. J. 2009, ApJ, 698, 986 [ADS] 3

Potter, D. W. 1981, J. Geophys. Res., 86, 11111 [ADS] 80

Press, W. H., Teukolsky, S. A., Vetterling, W. T., & Flannery, B. P. 1992, Numerical Recipes in FORTRAN, 2nd edition. The art of scientific computing (Cambridge University Press) [ADS] 88, 91

Pulkkinen, T. 2007, Living Reviews in Solar Physics, 4, 1 [ADS] 4

Pulupa, M. & Bale, S. D. 2008, ApJ, 676, 1330 [ADS] 81, 84, 86, 95

Pulupa, M. P., Bale, S. D., & Kasper, J. C. 2010, Journal of Geophysical Research (Space Physics), 115, 4106 [ADS]

Reames, D. V. 1999, Space Science Reviews, 90, 413 [ADS] 4

Reiner, M. J., Kaiser, M. L., Fainberg, J., Bougeret, J., & Stone, R. G. 1998a, Geophys. Res. Lett., 25, 2493 [ADS] 45, 62, 80

Reiner, M. J., Kaiser, M. L., Fainberg, J., & Stone, R. G. 1998b, J. Geophys. Res., 103, 29651 [ADS] 62

Richardson, I. G., Webb, D. F., Zhang, J., Berdichevsky, D. B., Biesecker, D. A., Kasper, J. C., Kataoka, R., Steinberg, J. T., Thompson, B. J., Wu, C., & Zhukov, A. N. 2006, Journal of Geophysical Research (Space Physics), 111, 7 [ADS] 84

Richardson, J. D. & Stone, E. C. 2009, Space Science Reviews, 143, 7 [ADS] 11

Robinson, P. A. 1992, Sol. Phys., 139, 147 [ADS] 41

—. 1993, Sol. Phys., 146, 357 [ADS] 155

—. 1996, Sol. Phys., 168, 357 [ADS] 41

Robinson, P. A. & Benz, A. O. 2000, Sol. Phys., 194, 345 [ADS] 104

Robinson, P. A. & Cairns, I. H. 1993, ApJ, 418, 506 [ADS] 41

—. 1998, Sol. Phys., 181, 363 [ADS] 43

Robinson, P. A., Cairns, I. H., & Gurnett, D. A. 1993, ApJ, 407, 790 [ADS] 41

Robinson, P. A., Cairns, I. H., & Willes, A. J. 1994, ApJ, 422, 870 [ADS] 43

Rosenbauer, H., Schwenn, R., Marsch, E., Meyer, B., Miggenrieder, H., Montgomery, M. D., Muehlhaeuser, K. H., Pilipp, W., Voges, W., & Zink, S. M. 1977, Journal of Geophysics Zeitschrift Geophysik, 42, 561 [ADS] 33

Rouillard, A. P., Davies, J. A., Forsyth, R. J., Rees, A., Davis, C. J., Harrison, R. A., Lockwood, M., Bewsher, D., Crothers, S. R., Eyles, C. J., Hapgood, M., & Perry, C. H. 2008, Geophys. Res. Lett., 35, 10110 [ADS] 54

Rucker, H. O., Macher, W., Fischer, G., Oswald, T., Bougeret, J. L., Kaiser, M. L., & Goetz, K. 2005, Advances in Space Research, 36, 1530 [ADS] 153

Rucker, H. O., Macher, W., Manning, R., & Ladreiter, H. P. 1996, Radio Science, 31, 1299 [ADS] 137, 138, 139

Russell, C. T. 1985, in Collisionless Shocks in the Heliosphere: Reviews of Current Research, ed. Tsurutani, B. T. and Stone, R. G. (AGU Geophysical Monograph 35), 109–130 19

Sagdeev, R. Z. 1979, Reviews of Modern Physics, 51, 11 [ADS] 8

Salem, C., Hubert, D., Lacombe, C., Bale, S. D., Mangeney, A., Larson, D. E., & Lin, R. P. 2003, ApJ, 585, 1147 [ADS] 9, 32, 155

Salem, C., Mangeney, A., Bale, S. D., & Veltri, P. 2009, ApJ, 702, 537 [ADS] 3

Sarris, E. T., Krimigis, S. M., & Armstrong, T. P. 1976, Geophys. Res. Lett., 3, 133 [ADS] 26

Sauvaud, J., Larson, D., Aoustin, C., Curtis, D., Médale, J., Fedorov, A., Rouzaud, J., Luhmann, J., Moreau, T., Schröder, P., Louarn, P., Dandouras, I., & Penou, E. 2008, Space Science Reviews, 136, 227 [ADS] 57

Scarf, F. L., Fredricks, R. W., Frank, L. A., & Neugebauer, M. 1971, J. Geophys. Res., 76, 5162 [ADS] 80

Schubert, G. & Lichtenstein, B. R. 1974, Reviews of Geophysics, 12, 592 [ADS] 11

Schwenn, R. 1983, Space Science Reviews, 34, 85 [ADS] 10

Scime, E. E., Littleton, J. E., Gary, S. P., Skoug, R., & Lin, N. 2001, Geophys. Res. Lett., 28, 2169 [ADS] 95

Scudder, J. D., Mozer, F. S., Maynard, N. C., & Russell, C. T. 2002, Journal of Geophysical Research (Space Physics), 107, 1294 [ADS] 24

Sheeley, Jr., N. R., Howard, R. A., Michels, D. J., Koomen, M. J., Schwenn, R., Muehlhaeuser, K. H., & Rosenbauer, H. 1985, J. Geophys. Res., 90, 163 [ADS] 10

Shu, F. H. 1992, Physics of Astrophysics, Vol. II (University Science Books) [ADS] 8

Slavin, J. A. & Holzer, R. E. 1981, J. Geophys. Res., 86, 11401 [ADS] 11

Smith, E. J. & Wolfe, J. H. 1976, Geophys. Res. Lett., 3, 137 [ADS] 10

Soucek, J., Santolik, O., Dudok de Wit, T., & Pickett, J. S. 2009, Journal of Geophysical Research (Space Physics), 114, 2213 [ADS] 42

Spitzer, L. 1962, Physics of Fully Ionized Gases (Interscience) [ADS] 23

Spreiter, J. R., Summers, A. L., & Alksne, A. Y. 1966, Planet. Space Sci., 14, 223 [ADS] 11

Szabo, A. 1994, J. Geophys. Res., 99, 14737 [ADS] 15, 85

Thejappa, G. & MacDowall, R. J. 2000, ApJ, 544, L163 [ADS] 81, 89, 90, 94, 95, 96

Tonks, L. & Langmuir, I. 1929, Physical Review, 33, 195 [ADS] 37

Tsurutani, B. T., Gonzalez, W. D., Lakhina, G. S., & Alex, S. 2003, Journal of Geophysical Research (Space Physics), 108, 1268 [ADS] 5

Tsurutani, B. T. & Lin, R. P. 1985, J. Geophys. Res., 90, 1 [ADS] 25, 26

Ullrich, R., McCauley, J., Turin, P., McKee, K., & Donokowski, B. 2008, Space Science Reviews, 136, 185 [ADS] 56

Štverák, Š., Maksimovic, M., Trávníček, P. M., Marsch, E., Fazakerley, A. N., & Scime, E. E. 2009, Journal of Geophysical Research (Space Physics), 114, 5104 [ADS] 32, 33

Štverák, Š., Trávníček, P., Maksimovic, M., Marsch, E., Fazakerley, A. N., & Scime, E. E. 2008, Journal of Geophysical Research (Space Physics), 113, 3103 [ADS] 94

van Nes, P., Reinhard, R., Sanderson, T. R., Wenzel, K., & Zwickl, R. D. 1984, J. Geophys. Res., 89, 2122 [ADS] 25, 26

Vasyliunas, V. M. 1968, J. Geophys. Res., 73, 2839 [ADS] 32

—. 1975, Reviews of Geophysics and Space Physics, 13, 303 [ADS] 21, 23

—. 2009, in Heliophysics: Plasma Physics of the Local Cosmos, ed. Schrijver, C. J. and Siscoe, G. L. (Cambridge University Press), 256–294 11

Veselovsky, I., Dmitriev, A. V., Suvorova, A. V., & Tarsina, M. V. 2000, Journal of Astrophysics and Astronomy, 21, 423 [ADS] 95

Vinas, A. F. & Scudder, J. D. 1986, J. Geophys. Res., 91, 39 [ADS] 85

Volkmer, P. M. & Neubauer, F. M. 1985, Annales Geophysicae, 3, 1 [ADS] 19

Wang, C., Li, C. X., Huang, Z. H., & Richardson, J. D. 2006, Geophys. Res. Lett., 33, 14104 [ADS] 9

Wang, L., Lin, R. P., Larson, D. E., & Luhmann, J. G. 2008, Nature, 454, 81 [ADS] 59

Watt, C. E. J., Horne, R. B., & Freeman, M. P. 2002, Geophys. Res. Lett., 29, 010000 [ADS] 23

Whang, Y. C., Larson, D., Lin, R. P., Lepping, R. P., & Szabo, A. 1998, Geophys. Res. Lett., 25, 2625 [ADS] 19

Whitham, G. B. 1974, Linear and nonlinear waves (Wiley) 8

Wild, J. P. 1985, in Solar Radiophysics, ed. McLean, D. J. and Labrum, N. R. (Cambridge University Press), 3–18 29

Wild, J. P., Murray, J. D., & Rowe, W. C. 1954, Australian Journal of Physics, 7, 439 [ADS] 29

Willes, A. J. & Cairns, I. H. 2001, Publications of the Astronomical Society of Australia, 18, 355 [ADS] 44

Wilson, L. B., Cattell, C. A., Kellogg, P. J., Goetz, K., Kersten, K., Kasper, J. C., Szabo, A., & Meziane, K. 2009, Journal of Geophysical Research (Space Physics), 114, 10106 [ADS] 117

Wilson, III, L. B., Cattell, C., Kellogg, P. J., Goetz, K., Kersten, K., Hanson, L., MacGregor, R., & Kasper, J. C. 2007, Physical Review Letters, 99, 041101 [ADS] 23, 81, 84

Wu, C. S. 1982, Space Science Reviews, 32, 83 [ADS] 9

—. 1984, J. Geophys. Res., 89, 8857 [ADS] 35, 62, 66, 82, 83

Yashiro, S., Gopalswamy, N., Michalek, G., St. Cyr, O. C., Plunkett, S. P., Rich, N. B., & Howard, R. A. 2004, Journal of Geophysical Research (Space Physics), 109, 7105 [ADS] 10

Yin, L., Ashour-Abdalla, M., El-Alaoui, M., Bosqued, J. M., & Bougeret, J. L. 1998, Geophys. Res. Lett., 25, 2609 [ADS] 44

Yuan, X., Cairns, I. H., & Robinson, P. A. 2008, Journal of Geophysical Research (Space Physics), 113, 8109 [ADS] 108

Zakharov, L. & Rogers, B. 1992, Physics of Fluids B, 4, 3285 [ADS] 24

Zank, G. P. 1999, Space Science Reviews, 89, 413 [ADS] 11

Zarka, P. 2000, in Radio Astronomy at Long Wavelengths, ed. Stone, R. G. and Weiler, K. W. and Goldstein, M. L. and Bougeret, J. L. (AGU Geophysical Monograph 119), 167–178 154

Zhang, J., Richardson, I. G., Webb, D. F., Gopalswamy, N., Huttunen, E., Kasper, J. C., Nitta, N. V., Poomvises, W., Thompson, B. J., Wu, C., Yashiro, S., & Zhukov, A. N. 2007, Journal of Geophysical Research (Space Physics), 112, 10102 [ADS] 4, 84

Ziebell, L. F., Gaelzer, R., Pavan, J., & Yoon, P. H. 2008, Plasma Physics and Controlled Fusion, 50, 085011 [ADS] 116

Zimbardo, G. & Veltri, P. 1996, Geophys. Res. Lett., 23, 793 [ADS] 74, 113

Zouganelis, I., Maksimovic, M., Meyer-Vernet, N., Bale, S. D., Eastwood, J. P., Zaslavsky, A., Dekkali, M., Goetz, K., & Kaiser, M. L. 2010, Radio Science, 45, 1005 [ADS] 48

Appendix A

Antenna Calibration

The response pattern of a spacecraft-mounted radio antenna to an electric field differs from the response of an ideal dipole or monopole antenna. This difference is due to the presence of conducting material, such as the spacecraft chassis, solar panels, or other instruments, in the vicinity of the antenna. For low frequency, long wavelength signals, this effect can be accurately modeled using a scale model of the spacecraft which is immersed in an electrolyte-filled tank. This method of antenna calibration is known as rheometry. Rheometry is one of several methods that have been used to calibrate the "effective length" of electric antennas for three-axis stabilized spacecraft missions, and serves as a complementary method to computer simulations and in-flight calibration methods.

This appendix describes the theory of rheometry and serves as a practical guide to the use of the rheometry equipment at the UC Berkeley Space Sciences Laboratory (SSL). The SSL rheometry apparatus is based on the apparatus constructed at the Space Research Institute in Graz, Austria. A full description of the Graz apparatus, as well as a detailed outline of the theoretical background of rheometry, is given in Rucker et al. (1996). Results for the STEREO/WAVES (S/WAVES) antennas are also presented.

IDL, C, and Java code used in running the experiment and in performing the data analysis can be found in the `/home/pulupa/rheosoft` directory on the SSL Space Physics Research Group (SPRG) server.

A.1 Introduction: Antennas

Electric field and plasma wave antennas on three-axis stabilized spacecraft usually consist of straight rods, implemented as a nested 'stacer' configuration or as a rigid single piece of conductive material. For mechanical and environmental reasons, the length of these rods is limited to several meters. (Antennas in the spin plane of spin-stabilized spacecraft,

in contrast, can be constructed of wire which is held taut by centripetal force, and can therefore be much longer.)

Since the length of the fixed antennas is comparable to the dimensions of other conductive spacecraft components, the electrical response of the antennas varies significantly from the response of an ideal monopole antenna. Conducting surfaces which can affect the electrical response of a given antenna include the spacecraft chassis, solar panels, the high gain telemetry antenna, the other radio antennas, and the instrument booms. These elements are parasitic conductors with respect to the electromagnetic properties of the antenna system. In general, the worst parasitic conductors (i.e., the ones which most affect the electrical response of a given antenna) are those which are large and which extend away from the spacecraft in the same general direction as the antenna.

The response of the antenna to incident electromagnetic radiation with a given wave vector $\mathbf{k}$ is known as the antenna pattern. The antenna pattern is in general a frequency-dependent and complex surface in $\mathbf{k}$-space, possibly with many maxima and nulls in various directions. However, in the low frequency "short antenna" limit, the ideal antenna response can be well characterized by a simple static dipole response. Ignoring the parasitic conductors, the antenna response is given by $V = \mathbf{E} \cdot \mathbf{L}/2$, where V is the measured potential on the antenna, $\mathbf{E}$ is the incident electric field, and $\mathbf{L}$ is the physical antenna vector. This regime is also known as the quasistatic range (Rucker et al. 1996).

The effect of parasitic conductors is to change the vector which characterizes the electric response to a new vector known as the "effective electrical antenna vector", or the "effective antenna vector" for short. The effective antenna vector $\mathbf{h}$ satisfies $V = \mathbf{E} \cdot \mathbf{h}$. The short antenna limit is defined as $\lambda \gg L$, where λ is the wavelength of the radio wave and L is the length of the antenna. For the S/WAVES antennas, which are 6 m long, the quasistatic range extends up to around 2 MHz (Oswald et al. 2009). In this quasistatic regime, it is possible to make experimental rheometry measurements of the effective antennas using a scale model spacecraft immersed in an electrolytic tank.

A.2 Rheometry Theory

The effectiveness of scale model measurements is justified by the linearity of Maxwell's equations. There are two reasons for making the measurement in water, as opposed to in free space. The first is related to the impedance characteristics of the measurement apparatus, while the second reason has to do with the uniformity of the experimental electric field. The derivations and notation in this section follow Rucker et al. (1996).

A.2.1 Impedance of the Rheometry Model

We measure the response of the antenna to the incident electric field by attaching a voltmeter across the gap between the antenna and the spacecraft body. The impedance

across this gap has two elements in parallel: a resistive element and a capacitive element (see Figure A.1). In air, the resistive element is immense (the breakdown voltage of air depends on the humidity and electrode shape, but is in the several kV/mm range) so the impedance is dominated by the capacitive element. For typical spacecraft models, the capacitance in air is several pF, which at 1 kHz[1] leads to an impedance on the order of 100 MΩ. This impedance is significantly higher than the 50 MΩ impedance of the differential amplifier we use to make the voltage measurements, and so the measurement will not be accurate.

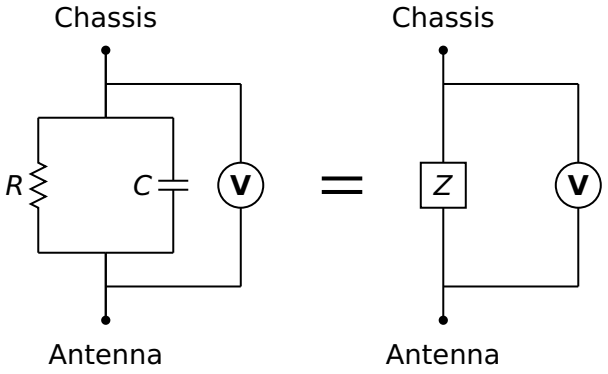

Figure A.1: Capacitive and resistive impedances of the antenna-chassis system.

	Z_R	Z_C	Z
Air	∞ (eff.)	100 MΩ	100 MΩ $> Z_{\mathrm{V}}$
Water	0.1 Ω	1 MΩ	0.1 Ω $\ll Z_{\mathrm{V}}$

Table A.1: Capacitive and resistive impedances of the antenna-chassis system, in air and in water. $Z_{\mathrm{V}} = 50$ MΩ represents the voltmeter (in this case, the differential amplifier) impedance.

Placing the spacecraft model in the water tank greatly decreases the resistive impedance, so much so that the resistive element dominates the parallel impedance. The conductivity of the tap water, as determined by measuring the current between the capacitor plates at a given voltage, is on the order of 0.05 S/m. (The conductivity is somewhat higher than that of ordinary tap water, due to the addition of a small amount

[1]The rheometry measurement is made at a frequency of 1 kHz, which is well within the quasistatic range. This avoids polarization effects in the electrolyte that would arise if a DC field was used (Rucker et al. 1996).

of chlorine bleach in the tank to inhibit the growth of algae.) This conductivity lowers the resistance (and therefore the impedance) between a model antenna and chassis to typical values of $R \approx \varepsilon_0/\sigma C \approx 0.1\ \Omega$. The capacitive impedance is lowered as well, but it remains much higher than the resistive impedance, so the resistive impedance dominates the parallel impedance. At this $Z = 0.1\ \Omega$, the voltmeter can make a good measurement.

A.2.2 Boundary Conditions

The second reason for making the measurement in an electrolytic tank is that the boundary conditions between the electrolyte and the long sides of the tank force the electric field inside the tank to run parallel to the long axis of the tank. (The capacitor plates which drive the electric field are on either end of the long axis, as described in the following section.) This can be shown by the application of Maxwell's equations at the interface between the water and a long side of the tank (either air or acrylic).

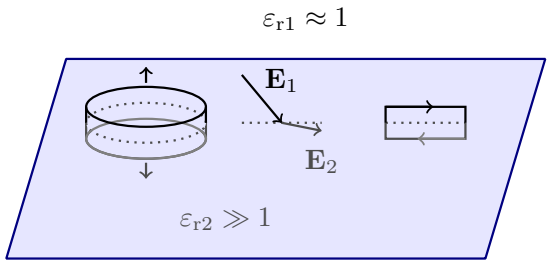

Figure A.2: Interface between air and dielectric

Let the internal electric field in the tank be $\mathbf{E}$, and the external field be $\mathbf{E}^{\text{ext}}$. The field oscillates with frequency ω. However, this frequency is sufficiently low to allow us to treat the configuration as quasi-static, and therefore ignore the time-dependent terms in Maxwell's equations. Let $\mathbf{n}$ be the unit normal vector at a given point on the interface. Using Gauss' Law on the pillbox with surface S and volume V in Figure A.2 yields:

$$\oint_S \mathbf{D} \cdot \mathbf{n}\, da = \int_V \rho\, d^3x \tag{A.1}$$

If the Gaussian pillbox is infinitesimally thin, then edge effects are unimportant. Since the response of the electrolytic medium is linear and because there is effectively zero free charge at the interface, $\mathbf{D} = \varepsilon\mathbf{E}$ and Equation A.2 reduces to the boundary condition:

$$\varepsilon_{\text{water}}\ \mathbf{n} \cdot \mathbf{E} = \varepsilon_{\text{ext}}\ \mathbf{n} \cdot \mathbf{E}^{\text{ext}} \tag{A.2}$$

Using Faraday's Law on the loop in Figure A.2, with contour C and surface S, yields:

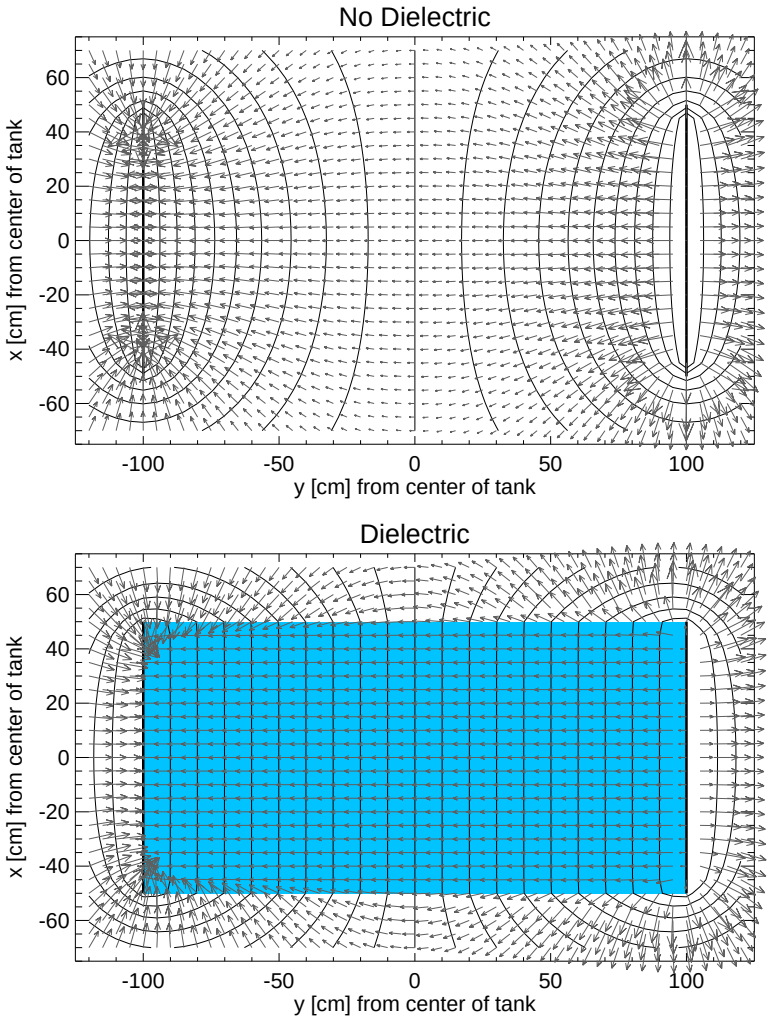

Figure A.3: Effect of dielectric on electric field between rheometry tank capacitor plates. The plot shows a cut through a numerical solution of Laplace's equation in a 3D grid. In both plots, two one meter square conducting capacitor plates are placed two meters apart, as in the actual configuration of the rheometry tank. Potentials of V and $-V$ are placed on the capacitor plates (thick black lines), and a relaxation method is employed to solve for the potential. The solid curves are voltage contours at intervals of $0.1V$. The gray arrows show the direction and magnitude of the electric field.

$$\oint_C \mathbf{E} \cdot d\mathbf{l} = -\int_S \frac{\partial \mathbf{B}}{\partial t} \cdot \mathbf{n}\, da \tag{A.3}$$

Reducing the width of the loop to an infinitesimal length and making use of the quasistatic assumption above yields:

$$\mathbf{n} \times \mathbf{E} = \mathbf{n} \times \mathbf{E}^{\text{ext}} \tag{A.4}$$

Medium	ε_r	Source
Vacuum	1.	(Definition)
Air	∼1.0006	(Hector & Schultz 1936)
Acrylite GP	3.3	(CYRO Industries 2002)
Tap Water (20°C)	∼80.	(Ellison et al. 1996)

Table A.2: Values of $\varepsilon_r = \varepsilon/\varepsilon_0$ for selected dielectric materials at 1 kHz. Ellison et al. (1996) present values of ε_r for pure water, but ε_r does not vary greatly due to the addition of relatively low concentrations of impurities (Drake et al. 1930).

Equations A.2 and A.4 are the boundary conditions for the electric field at the interface between the water and the long sides of the tank. Data from Table A.2 shows that, for both air-water and acrylic-water interfaces, $\varepsilon_{\text{water}} \gg \varepsilon_{\text{ext}}$, and therefore the boundary conditions require that the electric field be almost tangential to the interface surface, and therefore $\mathbf{E}$ is close to uniform throughout the tank. Solutions of Laplace's equation for two square capacitor plates of dimension and separation equivalent to that found in the tank are shown in Figure A.3.

Calibration of the tank with a simple model consisting solely of a test dipole antenna has confirmed that, within the volume in which the spacecraft models are placed, the electric field is uniform to within 0.5% in magnitude, and uniform up to the angular measurement uncertainty (about 1°) in direction.

A.3 Construction

A.3.1 Tank Construction

The rheometry tank is a rectangular prism, 2 m long by 1 m wide by 1 m high. Figure A.4 shows a diagram of the tank setup as well as a picture of the filled tank during a measurement.

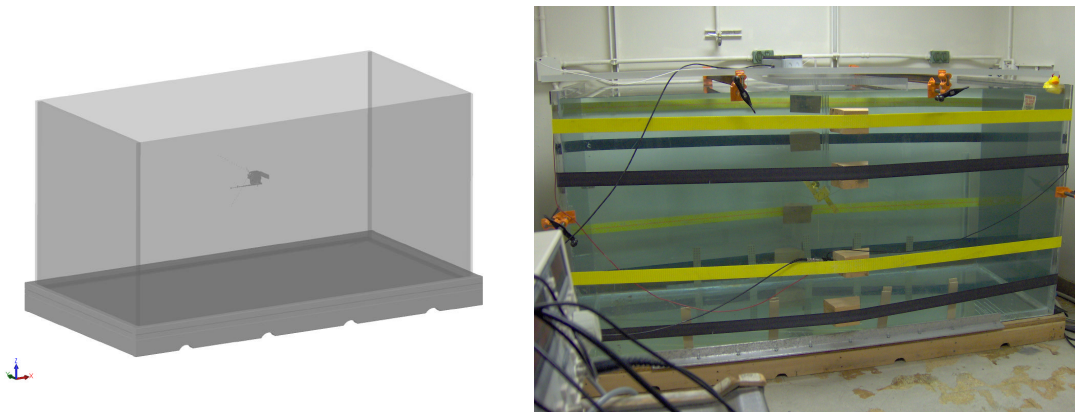

Figure A.4: Two views of the rheometry apparatus with the STEREO model suspended in the tank. Above, a diagram showing the relative size of the tank. Below, a picture of the actual tank, filled with water and including the STEREO model.

The panel side material is Acrylite GP, manufactured by Cyro Industries. The acrylic panels are joined with two-part solvent cement. Leftover solvent cement is stored in 114AA and can be used to fix the tank should the panels separate under stress. The seams of the tank are filled with silicone-based caulk to prevent leaks. After being dry for a long period, the caulk may need replacement. ***Caution****: the cement produces hazardous fumes—make sure the ventilation fan in the ceiling is installed and vented to the outdoors, make sure the other fans in the room are covered, and glue on a weekend when the building is vacant.*

The capacitor plates are two 1 meter by 1 meter sheets of stainless steel, the ends of which have been bent to hook over the short edges of the tank. Banana jacks are installed on each plate to connect to a function generator and drive the electric field. More information on the electrical setup of the capacitor plates can be found in Section A.4.

A.3.2 Manipulator

The spacecraft model orientation is controlled by the manipulator apparatus. The manipulator, which rests in a circular hole in the bridge which lies across the top of the apparatus, provides two degrees of rotational freedom. The first degree of freedom, α, controls the rotating arm. The arm protruding from the top of the manipulator is turned, and the gears on the manipulator transmit that motion into a rotation of the spacecraft model in the horizontal plane.

The second degree of freedom, β, is controlled by manually rotating the entire manipulator apparatus in the circular hole. If it is difficult to move the manipulator, the

rim of the hole can be lubricated with lithium grease. Further discussion of α, β, and how the orientation affects the antenna measurements can be found in Section A.5.

The bridge and circular part of the manipulator is made of the same acrylic material as the tank walls. The arms are also made of acrylic, and the gears are made of nonconducting Delrin plastic. The manipulator is made entirely of nonconducting material so as not to interfere with the rheometry measurements. The manipulator arm is hollow, so the signal-carrying wires from the model antennas and chassis can be passed through and out of the tank. The wires themselves are as thin as is practical in order to avoid interfering with the electrical measurement.

At the end of the manipulator arm is a circular plate with a hole for the signal wires and two mounting holes for the model. The model should be constructed with mounting threaded sockets that match the separation of the manipulator mounting holes. It is normally easiest to construct the model with the mounting sockets on the opposite side from the antennas, in order to allow the largest possible range of rotation.

A.3.3 Model Construction

The rheometry model must be an accurate representation of the spacecraft, including all of the important elements which can act as parasitic conductors. All of surfaces of the spacecraft model should be conducting surfaces. (In the case of STEREO, the conducting properties of the spacecraft were ensured by covering most of the spacecraft with a conductive blanket, including the back side of the solar panel arrays (Driesman et al. 2008).) The STEREO model was gold plated to ensure that the entire surface was a good conductor. For the remainder of this appendix, we will refer to the entire conductive spacecraft model as the chassis. The antennas can be modeled using simple metal rods cut to the appropriate length. Lead wires should be connected to each antenna and the chassis. Finally, the model should be constructed so that it can easily mount to the manipulator, as described in the previous section. Figure A.5 shows a diagram of the STEREO rheometry model and the actual constructed model. The position of the high gain communications antenna (HGA) on the model is adjustable, so the effect of the changing position of the HGA on the effective length vectors can be quantified.

A.4 Measurement

A.4.1 Mechanical Setup

In order to make the measurement, the water tank must be filled with tap water, using the hose available in Room 114AA. The volume of water in the filled tank is roughly 2000 L, with a mass of about 2000 kg. Consequently, the tank should be filled slowly, over a period of about one hour, while the experimenter carefully monitors the fill process.

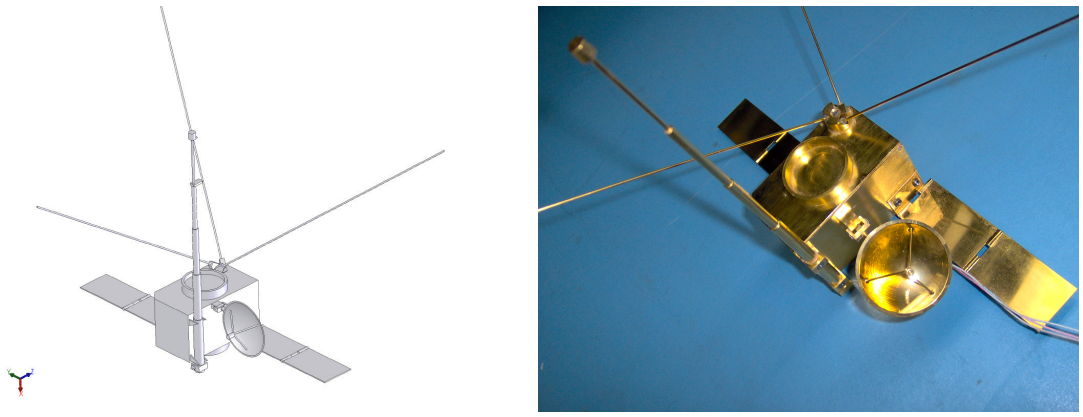

Figure A.5: Left, a diagram of the STEREO rheometry scale model, with the three S/WAVES antennas. Spacecraft features included in the model are those which will affect the electrical antenna length and direction, such as the IMPACT boom, the solar panels, and the HGA. Right, a picture of the gold-plated STEREO model.

Before starting the fill, measure the distance across the top of the tank between the midpoints of the two long acrylic panels. Check this distance periodically, both during the fill and for several hours after the tank is full, to make sure that the tank panels are not bowing out substantially. If the panels do bow out by more than about one inch, tighten the clamps and ratchet tie downs which support and encircle the tank to reduce the separation. During and after the fill, the ratchet tiedowns should be tightened to hold the joints tight, and the clamps should be tightened if they are loose.

If any leaks appear around the corners of the tank, the filling process should immediately be halted to assess the cause. Minor leaks, especially near the top of the tank, may be fixed with caulk. Major leaks, or any cracks in the glue or acrylic panels, require a full draining of the tank and a reapplication of two-part acrylic epoxy. Clamp the glue joint tightly while the glue is drying—if large air bubbles remain, the joint will be weak.

In the event of an emergency leak, the tank may be drained quickly using the blue submersible pump, which should be stored next to the tank at all times. Simply plug in the pump, feed the output hose down the drainpipe in the floor, and place the pump in the tank.

After making experimental measurements, the spacecraft model should always be removed from the rheometry tank to prevent corrosion of the metal elements of the model.

With particularly large or heavy rheometry models, it may be advisable to attach the model to the manipulator while it is submerged, to take advantage of the buoyancy of the model to reduce strain on the manipulator arm.

A.4.2 Electronics

In this section, the electronic setup of the rheometry apparatus is described in some detail. Figure A.6 graphically summarizes the information in this section using a block diagram which illustrates the connections between the various electric components.

Function Generator

The electric field in the rheometry tank is created by the Tektronix function generator. Set the frequency at 1 kHz and the amplitude at 5 V. The peak-to-peak amplitude of the electric field in the electrolyte is therefore approximately 2.5 V/m. The generated function should be set to a sine wave with zero offset.

The output from CH1 is set to ON and split into a BNC tee adapter. One end is connected to a 50 Ω feedthrough terminator, which passes the signal through to two banana jacks. Connect these to the capacitor plates using banana plugs. The other end of the tee is passed through to the oscilloscope.

Connect the SYNC OUT BNC jack from the back panel of the function generator to the REF IN jack on the lock-in amplifier.

Preamplifier and Controller

The front end component of the preamplifier for the rheometry apparatus is a Intersil DG409 analog multiplexer, which selects the specific antenna channel to make a voltage measurement. Usually, the model is configured so that each antenna wire is connected to a separate 'A' channel on the multiplexer, while the chassis is connected to the 'B' channels, which are all shorted together. The multiplexer is controlled via a Arduino controller connected to the control CPU via USB, which sends logic signals to select one 'A' channel and one 'B' channel. The selected channels are then passed to the Analog AD621 instrumentation amplifier to make a differential voltage measurement between the antenna and the chassis. The instrumentation amplifier then makes a differential measurement with a gain of 10. Refer to the spec sheets for the DG409 and AD621 for more information on connections and properties. Measurement probes are attached to the output of the instrumentation amplifier, then sent to the lock-in amplifier and the oscilloscope.

Power Supplies

A DC power supplies is required for the differential preamplifier. The units in 114AA are Agilent E3631A DC power supplies. For both the amplifier and the driver, set the output voltage mode to ±25 V, and set the voltage to ±15 V. The differential amplifier should be connected using the appropriate connectors to the ±15 V as well as to the

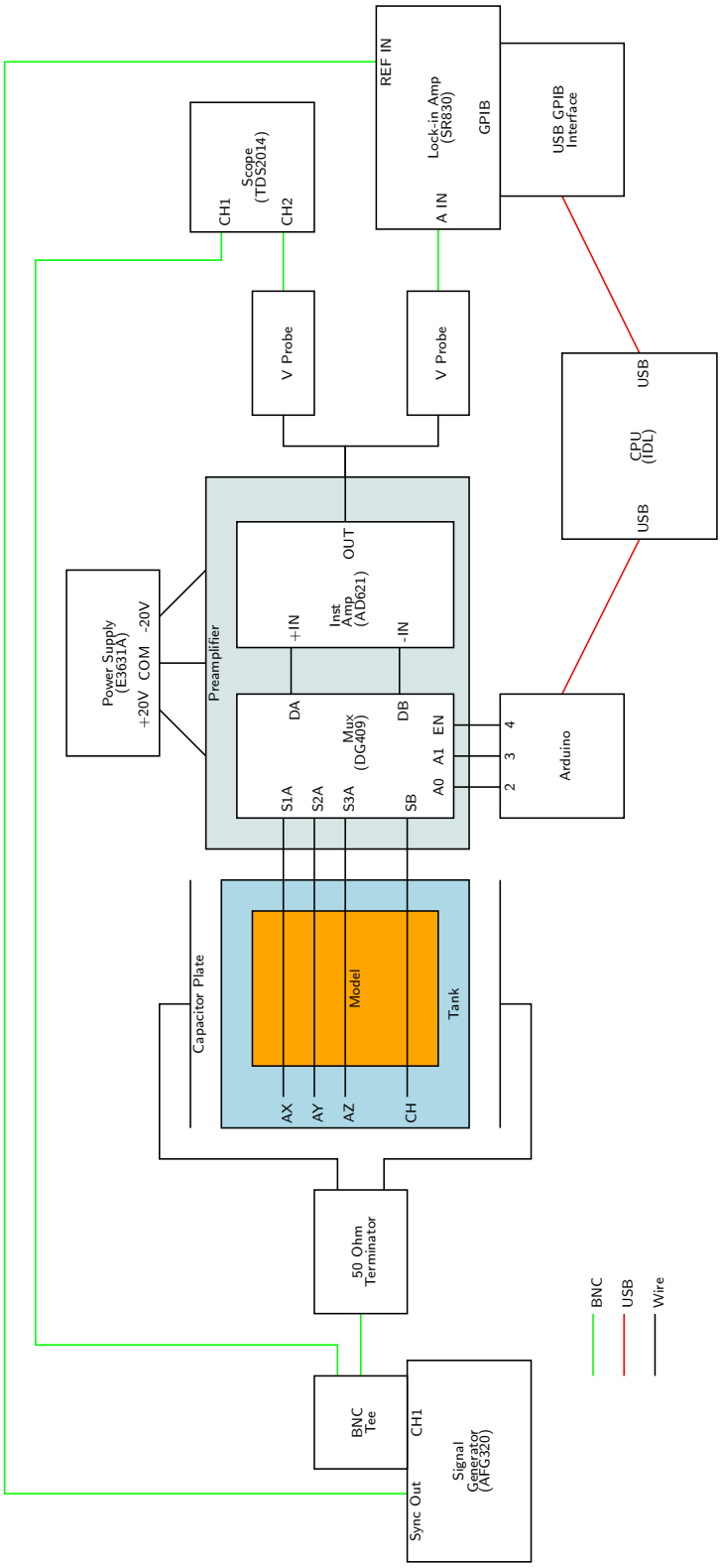

Figure A.6: Conceptual block diagram of a rheometry tank experiment.

COM ground connection. Do not connect the amplifier ground to the green terminal marked $\perp$, as this will result in an inaccurate measurement.

Interface with Lock-In Amplifier

The actual measurement of differential voltage is made by a Stanford Research Systems SR830 DSP lock-in amplifier. There should be three connections to the lock-in amplifier: the SYNC OUT from the function generator should be connected to the REF IN BNC port, a 10x probe from the differential amplifier should be connected to the A input, and the GPIB-USB interface should be attached to the GPIB port on the rear panel and connected to the control computer via a USB cable. Table A.3 shows suggested settings for the SR830. The lock-in amplifier measures the RMS voltage at the frequency supplied by the function generator. Typical values of measured RMS voltage for the STEREO model lie in the 0-20 mV range, depending on the orientation of the spacecraft model.

Lock-In Variable	Setting
Time Constant	30 ms
Sensitivity	200 mV
Input	A
Couple	AC
Ground	Float
Reserve	Low Noise
Filters	None
Ch1 Display	R
Ch1 Ratio	None
Ch1 Expand	x10
Ch2 Display	θ
Ch2 Ratio	None
Ch2 Expand	None
Reference Source	External
Trigger	Positive Edge
GPIB Address	5
GPIB Baud	9600
GPIB Parity	None

Table A.3: Settings for the SR830 lock-in amplifier.

A.5 Analysis

As described previously, the rheometry manipulator apparatus allows for two angular degrees of freedom (α and β) in the orientation of the model. α and β are illustrated in Figure A.7, and expressed in the format of a rotation matrix in Equation A.5. The notation used in this section assumes that the $\hat{\mathbf{z}}$ vector points in the vertical direction, and that the $\hat{\mathbf{y}}$ vector points in the direction of the long axis of the tank. Before voltage measurements are made, be sure to take careful note of the orientation of the spacecraft model as a function of α and β, so as to be able to translate the electric measurements into spacecraft model coordinates.

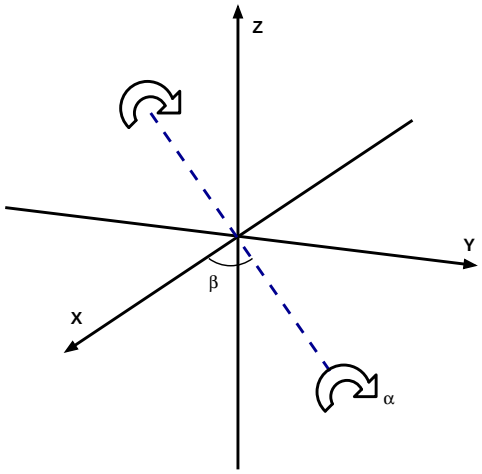

Figure A.7: Illustration of the two degrees of rotational freedom provided by the manipulator. The rotation matrix for this operation is described by Equation A.5.

$$\mathbf{R}(\alpha,\beta) = \begin{pmatrix} \cos^2\beta + \sin^2\beta\cos\alpha & \cos\beta\sin\beta(1-\cos\alpha) & -\sin\beta\sin\alpha \\ \cos\beta\sin\beta(1-\cos\alpha) & \sin^2\beta + \cos^2\beta\cos\alpha & \cos\beta\sin\alpha \\ \sin\beta\sin\alpha & -\cos\beta\sin\alpha & \cos\alpha \end{pmatrix} \tag{A.5}$$

Once we have made voltage measurements at various values of α and β, a three dimensional fit based on Equation A.5 can be performed. Given an electric field in the $\hat{\mathbf{y}}$ direction (parallel to the long axis of the tank), the voltage measured by an antenna is given by:

$$V(r,\alpha,\beta,\gamma) = r|\sin\gamma\cos\beta\sin\beta(\cos\alpha - 1) + \cos\gamma(\cos^2\beta\cos\alpha + \sin^2\beta)| \tag{A.6}$$

where $\alpha = \alpha_0$ is defined as the α for which the electrical antenna vector lies in the $\hat{\mathbf{x}} - \hat{\mathbf{y}}$ plane, and γ is the angle the effective electrical antenna makes with $\hat{\mathbf{y}}$ when $\alpha = \alpha_0$. The fit determines three parameters (r, γ, and α_0, the zero offset of α), which uniquely define the electrical antenna vector $\mathbf{h}$.

A.6 Results for S/WAVES

Results of this analysis for one of the S/WAVES antennas are shown in Figure A.8. The best fit triple of [r, α_0, γ] for all of the data (plotted as diamonds) is plugged in to Equation A.6 and the results are plotted as dotted lines. Heuristically, the r parameter determines the size of the lobes, the γ parameter determines the relative size of the lobes for a given value of β, and α_0 determines the tilt of the lobes. It should be noted that it is not useful to make measurements at β of zero or 90 degrees, since in that case Equation A.6 is degenerate with respect to r and γ and the two parameters cannot be fitted separately.

These results can be translated into the spacecraft frame, provided that the orientation of the model has been carefully recorded, and compared to the length and direction of the physical antennae. Figure A.9 shows the physical antenna vectors on the STEREO spacecraft in red and the effective vectors determined from rheometry measurements in black. The same data is presented in tabular form in Table A.4. The fact that the h values for the effective length vectors are roughly half of the length of the physical antennas is expected, since in the ideal case of no parasitic conductors the physical antennas will have an effective vector of length $L/2$. There is considerable variation from the ideal case in both the magnitude and direction of the effective length vectors.

S/WAVES rheometry measurements were also performed using using the Graz apparatus. The Graz team also included simulation data and compared configurations with open feed lines and with a defined base capacitance. The Graz open feed results agree well with the results presented here. Additionally, both rheometry experiments and simulations determined that the changing position of the HGA did not substantially affect the effective antenna vectors. All of the S/WAVES results are presented in Bale et al. (2008).

A.7 Rheometry as a Complementary Technique

A.7.1 Rheometry and Computer Simulations

The method of scale model rheometry was first developed (Hoang 1972; Hulin & Epstein 1973) during a time when computer simulation of the electromagnetic properties of antennas was difficult and expensive. Today, the exponential increase in computer capability means that high-quality antenna simulations can be inexpensively and quickly

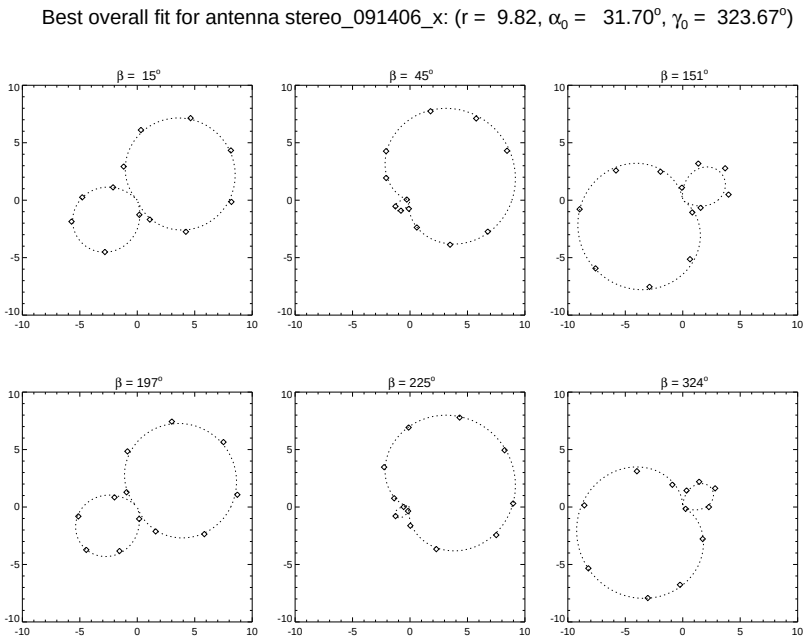

Figure A.8: Fits of Equation A.6 from rheometry measurements of the S/WAVES model $\mathbf{E_X}$ antenna. The maximum size of the fit lobes corresponds to r, the relative size of the lobes corresponds to γ, and the tilt of the lobes corresponds to α_0. Once these parameters are determined, they can be transformed into spacecraft coordinates to obtain the effective length vectors.

	Antenna	h [m]	θ [deg]	ϕ [deg]
Physical Antennas	X	6.00	125.3	-120.0
	Y	6.00	125.3	120.0
	Z	6.00	125.3	0.0
Effective Length Vectors	$\mathbf{h}_X$	3.04	127.0	-148.0
	$\mathbf{h}_Y$	3.95	120.8	123.6
	$\mathbf{h}_Z$	2.45	132.6	22.6

Table A.4: Table comparing the physical S/WAVES antennas and the measured effective antennas. Measurements do not include the effect of base capacitance. The coordinate system for the above measurement is defined in Bale et al. (2008).

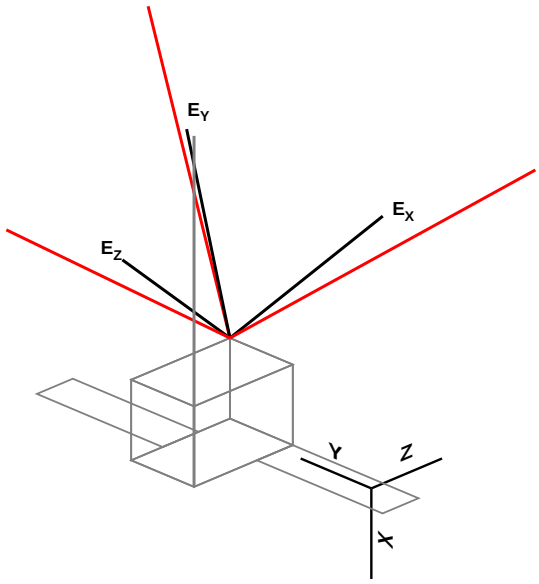

Figure A.9: Diagram of measured effective antenna vectors for the S/WAVES antennas. Physical antennas are shown in red, effective vectors shown in black.

performed on a desktop or laptop computer. However, rheometry still has a useful role to play in antenna calibration. Antenna codes, which are primarily developed for ground-based communication antennas, mainly focus on relatively high frequencies and cannot be extended to arbitrarily low frequencies while remaining numerically stable. In practice, at fairly low frequencies the antenna codes tend towards an asymptotic value for the effective length. The quasistatic value of the effective length as measured by the rheometry apparatus provides a ground-truth measurement which can be used to confirm the validity of the simulation at low frequencies. Rheometry may also be superior to numerical methods when modeling very fine structural components of the spacecraft (Rucker et al. 2005; Oswald et al. 2009).

It is true that the financial and time cost of constructing a physical apparatus and making a laboratory measurement will likely always be higher than the expense of a numerical simulation of spacecraft antenna with the comparable precision. However, given the presence of an already-constructed apparatus, the rheometry method remains quite inexpensive and quick. Once the model is constructed and wires connected to the antenna elements and chassis, the entire measurement process takes only a few hours. New methods for constructing spacecraft models, such as computed numerically controlled (CNC) fabrication of conductively-coated plastic models, allows rheometry to be sufficiently speedy and inexpensive to use as a prototyping tool.

A.7.2 Rheometry and In-flight calibration

In-flight calibration of electric antennas can also be performed, and provides the only direct measurement of effective antenna direction using the actual spacecraft antennas. In-flight calibration requires a source of known location, such as the terrestrial auroral emission generated by the cyclotron maser instability, which is known as auroral kilometric radiation (AKR) (Zarka 2000). If the spacecraft is sufficiently far from the region where the AKR is generated that it can treat the AKR as a point source, the direction finding equations (Cecconi & Zarka 2005) can be inverted to find the effective antenna lengths given the direction of the source. In the early post-launch stages of missions, spacecraft often perform roll maneuvers in order to calibrate the onboard magnetometers. These periods are also useful for performing in-flight calibration of the electric antennas, since the smooth motion of the spacecraft induces a signal on the antennas whose effect is clearly due solely to the rotation of the effective antenna vectors. Panchenko (2009) has measured the S/WAVES antenna effective vectors using magnetometer roll periods early in the STEREO mission where the spacecraft was close enough to Earth to see the AKR clearly, but far enough to treat the AKR as a point source. Panchenko (2009) solved the equations from Cecconi & Zarka (2005) using a singular value decomposition (SVD) technique, and compared the results to the rheometry and simulation derived results from (Bale et al. 2008). The published results include two sets of measurements (from Graz and Berkeley) made without taking into account the antenna base capacitance[2], and one measurement (from Graz) which does take the antenna base capacitance into account. The stray capacitance for the S/WAVES antennas has been measured and was found to be roughly 32 pF (Bale et al. 2008). With the stray capacitance taken into account, the Graz measurements agree very well with the in-flight calibration, showing that a realistic estimate of stray capacitance is important if one intends to use rheometry as a method of determining effective length vectors (Macher et al. 2007).

[2]At frequencies above the local plasma frequency, the antenna impedance is determined by the antenna capacitance, which for a monopole of effective length h and diameter d is given by $C_{\mathrm{a}} = \varepsilon\pi h/(\ln(2h/d) - 1)$, and by the stray capacitance C_{b}, which is a combination of capacitances between the antenna and the preamps, the preamp cables, and various components of the spacecraft (Manning 2000; Bale et al. 2008).

Appendix B

Formulae

This appendix lists common plasma parameters used in the text, their formulae, and approximations. The algebraic formulae are in SI units, while the units for the approximation results are shown in the brackets and are the most commonly used units in the solar wind at 1 AU for each given quantity. The input units for the approximations are cm^{-3} for the density n, eV for the temperature T, and nT for the magnetic field B.

The listed ion formulae are appropriate for protons. For other species, the formulae may be modified by replacing M with M_i, e with $Z_\mathrm{i}e$, and v with $v\sqrt{M/M_i}$, where M_i is the mass of the ion species and Z_i is its charge in units of e. Overall neutrality $n = n_\mathrm{i} = n_\mathrm{e}$ and a single temperature $T = T_\mathrm{i} = T_\mathrm{e}$ are assumed. γ is the adiabatic index of the plasma and is equivalent to $f + 2/f$, where f is the number of degrees of freedom in the plasma.

The formulae and approximations in Table B.1 can be found in Huba (2004) except for the Langmuir wave growth rate, from Robinson (1993). The collisional mean free path is calculated using $\ln\Lambda \approx 25.5$ (Salem et al. 2003) and using the electron collision time τ_e, temperature, and thermal speed. (The collision time $\propto m^{1/2}$, and the thermal speed $\propto m^{-1/2}$, so the corresponding collisional mean free path τv is of the same magnitude for the ions and electrons.)

	Quantity	Formula	Approximation
$\omega_{\rm pe}$	Plasma frequency	$\left(\frac{ne^2}{\varepsilon_0 m}\right)^{1/2}$	$\frac{\omega_{\rm pe}}{2\pi}[\text{Hz}] = 9. \times 10^3\sqrt{n}$
$\omega_{\rm c}$	Electron cyclotron frequency	$\frac{eB}{m}$	$\frac{\omega_{\rm c}}{2\pi}[\text{Hz}] = 28.B$
$\Omega_{\rm c}$	Proton cyclotron frequency	$\frac{eB}{M}$	$\frac{\Omega_{\rm c}}{2\pi}[\text{Hz}] = 1.5 \times 10^{-2}B$
$r_{\rm Le}$	Electron Larmor radius	$\frac{mv_\perp}{eB}$	$r_{\rm Le}[\text{km}] = 2.38\sqrt{T}/B$
$r_{\rm Li}$	Ion Larmor radius	$\frac{Mv_\perp}{eB}$	$r_{\rm Li}[\text{km}] = 102.\sqrt{T}/B$
$c/\omega_{\rm pe}$	Electron skin depth/inertial length	—	$c/\omega_{\rm pe}[\text{km}] = 5.31/\sqrt{n}$
$c/\omega_{\rm pi}$	Ion skin depth/inertial length	—	$c/\omega_{\rm pi}[\text{km}] = 228./\sqrt{n}$
$\lambda_{\rm D}$	Debye length	$\left(\frac{\epsilon_0 kT}{ne^2}\right)^{1/2}$	$\lambda_{\rm D}[\text{m}] = 7.43\sqrt{T/n}$
β	Plasma beta	$\frac{nkT}{B^2/2\mu_0}$	$\beta = 0.403nT/B^2$
$v_{\rm e}$	Electron thermal speed	$\sqrt{\frac{2kT}{m}}$	$v_{\rm e}[\text{km/s}] = 593.\sqrt{T}$
$v_{\rm i}$	Ion thermal speed	$\sqrt{\frac{2kT}{M}}$	$v_{\rm i}[\text{km/s}] = 13.8\sqrt{T}$
c_s	Ion acoustic speed	$\sqrt{\frac{\gamma kT}{M}}$	$c_s[\text{km/s}] = 9.79\sqrt{\gamma T}$
$v_{\rm A}$	Alfvén speed	$\frac{B}{\sqrt{\mu_0 Mn}}$	$v_{\rm A}[\text{km/s}] = 21.8B/\sqrt{n}$
$\lambda_{\rm c}$	Collisional mean free path	$\frac{3(2\pi)^{3/2}}{\ln\Lambda}\frac{T^2\epsilon_0^2}{ne^4}$	$\lambda_{\rm c}[\text{km}] = 5.66 \times 10^6 T^2/n$
$\Gamma_{\rm L}$	Langmuir wave growth rate	$\omega_{\rm p}\frac{\pi v_{\rm beam}^2}{n_{\rm e}}\frac{\partial f}{\partial v}$	—